



Theoretical and Experimental Investigation of the Plasmonic Probe

Dissertation

zur Erlangung des akademischen Grades
doctor rerum naturalium
(Dr. rer. nat.)

vorgelegt dem Rat der Chemisch-Geowissenschaftlichen Fakultät der
Friedrich-Schiller-Universität Jena

von

M.Sc Kourosh Rezaei

geboren am 22.09.1990 in Ahvaz, Iran

Gutachter:

1. Prof. Dr. Volker Deckert
2. PD Dr. Jer-Shing Huang

Tag der Verteidigung: 25 August, 2023

Acknowledgements

I am profoundly grateful for the limitless support and love that my family has bestowed upon me throughout my journey.

To my beloved Pegah, your constant encouragement, understanding, and patience have been the key of my strength. Your dedication and your belief in me have fueled my determination to strive for excellence.

To my father, your guidance, wisdom, and unyielding belief in my potential have shaped me into the person I am today. Your sacrifices and hard work have set a remarkable example for me to follow, and I am forever indebted for the values you've implanted in me.

My achievements would not have been possible without the sacrifices, encouragement, and understanding of my entire family. Your support has been my driving force, and I am truly humbled to have such an incredible foundation to lean on.

With heartfelt gratitude,
Kourosh

Abstract

The diffraction limit does not permit us to reveal information from dimensions smaller than roughly one-half of the wavelength. Hence, it was traditionally impossible to optically interact selectively with nanoscale features. However, with the increasing trend towards nanoscience and nanotechnology, nano-optics science emerged. A central goal of nano-optics is to extend optical techniques to length scales beyond the diffraction limit. In recent years, several new approaches have been developed to overcome this limitation. Tip-enhanced near-field microscopy techniques, such as TERS and PiFM, are among the innovations built around an AFM system. In this work, first, an algorithm for batch processing of the measured AFM data is introduced and utilized to analyze the height distribution of the inactivated SARS-CoV-2 samples. In the next chapter, plasmonic probes, as the crucial components of any near-field optical microscopy techniques, are modeled and investigated. Here, complex and realistic particle shapes are used to analyze particle-based probes' near- and far-field behavior. It has been shown that only the front-most particle is decisive for the near-field signal. On the other hand, the rest of nanoparticles enhance the scattering intensity. Apart from the optical responses, the mechanical properties of tips are also modeled because higher harmonics of the tip's oscillations are the foundation of new patents such as torsional force microscopy and photo-induced force microscopy (PiFM). In the last chapter, the PiFM is introduced and employed in various applications, i.e., plasmonic probe's quality, field mapping, and optical response of the plasmonic NPs.

Contents

List of Figures	IV
List of Tables	VI
List of Acronyms	VII
1 Introduction	1
2 AFM Data Analysis: Batch Processing	4
2.1 Principles of the AFM	4
2.1.1 AFM and plasmonic probes	5
2.2 Atomic force microscopy: A suitable method for virus detection	8
2.3 Batch Processing	9
2.3.1 Pre-processing algorithm	9
2.3.2 Post-processing algorithm	12
3 Modeling the Probes	18
3.1 Background and the theory	18
3.1.1 Maxwell's equations	18
3.1.2 Wave optics	19
3.1.3 Correction of the field by numerical aperture	24
3.1.4 Laguerre-Gaussian beam	25
3.1.5 Principles of light matter interaction at nanoscale	27
3.1.6 Plasmonics	28
3.1.7 Calculation of electromagnetic phenomena in near-field optics	32
3.1.8 Optical setup configuration	34
3.1.9 Linear polarization	36
3.1.10 Radial polarization	37
3.1.11 Azimuthal polarization	37
3.2 Results	41
3.2.1 Absorption spectrum of plasmonic nanoparticles	42
3.2.2 Near-field response of plasmonic nanoparticles	46
3.2.3 Directionality of the scattering field in Plasmonic nanoparticles	50
3.2.4 Model Development and Optical Responses of a Realistic 3D tip	53

3.2.5	Modeling the Mechanical Properties of the Tips	60
4	Photo-induced Force Microscopy (PiFM)	63
4.1	Principles of PiFM	63
4.1.1	Theory of Sideband Coupling	66
4.1.2	Theoretical Investigation of the Optical Force Interaction at Nano Scale	71
4.2	Results	81
4.2.1	Mapping Electromagnetic Field Distributions at Nanoscale	83
4.2.2	Characterization of the plasmonic tips	87
4.2.3	High Resolution PiFM Imaging of Plasmonic Nanostructures	90
4.2.4	Focusing effect on PiFM	99
5	Summary and Outlook	105
	Zusammenfassung	106
6	Bibliography	108
	Selbständigkeitserklärung	126
	Copyright Permissions	127

List of Figures

2.1	AFM principle	5
2.2	AFM and plasmonic probes	6
2.3	Bending and the twist of a cantilever	7
2.4	Potential curve	7
2.5	Pre-processing algorithms applied on an AFM image	10
2.6	Computer vision in AFM data analysis	13
2.7	In-situ AFM data analysis	14
2.8	Height information of entities within an AFM image	14
2.9	SARS-CoV-2 Height distribution	15
2.10	SARS-CoV-2 Height normalized distribution	17
3.1	Wave optics	21
3.2	Gaussian beam	23
3.3	Jablonski diagram	27
3.4	Surface plasmon polariton (SPP)	29
3.5	Localized surface plasmon (LSP)	31
3.6	High-resolution optical microscopy configurations	34
3.7	Bottom illumination/collection under different polarizations	35
3.8	Modeling a LPB	36
3.9	Modeling a RPB	38
3.10	Modeling a APB	39
3.11	Far and near-field regions	42
3.12	NP size distribution histogram	43
3.13	Different modes in far-field spectrum of dimer of Ag NPs	44
3.14	Colormap of different modes in far-field spectrum of dimer of Ag NPs	44
3.15	Different zones in spectroscopy	46
3.16	Field-enhancement distribution of a single NP	49
3.17	Radiation pattern of a chain of Ag NPs	51
3.18	Modeling of a 3D tip	53
3.19	Absorption spectrum of a 3D tip	54
3.20	Near-field spectrum of a 3D tip	56
3.21	Radiation pattern of a 3D tip	58
3.22	Radiation pattern of a single and many particle 3D tip	59
3.23	Deflection of a AFM probes	61
4.1	Schematic of a PiFM setup	65

4.2	Dynamic motion of a cantilever.	66
4.3	Induced dipole moments of an AFM tip and particle	72
4.4	Lorentz force on a continuous charge distribution in motion	76
4.5	Comarison of Maxwell stress tensor and dipole-dipole approxi- mation methods	79
4.6	Application of PiFM in beam profile mapping	85
4.7	Application of PiFM in assistance of other tip-enhanced methods	89
4.8	Schematic comparison of a bare Si and an Au coated Si tip	90
4.9	Electric field distribution in dimer of Au NPs	92
4.10	Simultaneous AFM and PiFM imaging (512 x 512 pixels) of Au NPs	93
4.11	PiFM of Au dimer	95
4.12	Resolution in PiFM	97
4.13	Schematic of changes of focusing position	99
4.14	PiFM focus position	100
4.15	Synergy of PiFM and TERS	103

List of Tables

3.1	Comparison of the electric field enhancement within the 1 nm gap between the apex of gold/silver tip and glass or thin gold/silver substrate.	49
3.2	First five resonance frequencies and their corresponding oscillation of <i>Tap300Al-G</i> and <i>Tap190Al-G</i> tips.	60

List of Acronyms

AFM (Atomic Force Microscopy): A very-high-resolution type of scanning probe microscopy (SPM), with demonstrated resolution on the order of fractions of a nanometer.

APB (Azimuthally Polarized Beam): A beam of light has azimuthal polarization if at every position in the beam, the polarization (electric field) vector has tangential direction with respect to the centre of the beam.

LPB (Linearly Polarized Beam): A confinement of the electric or magnetic field vector of an electromagnetic radiation to a given plane along the direction of propagation.

NP (Nanoparticle): A nanoparticle is usually defined as a particle of matter that is between 1 and 100 nanometres (nm) in diameter.

PiFM (Photo-induced Force Microscopy): A scattering type of scanning near-field optical microscopy (scattering SNOM or s-SNOM), where mechanical technique (as opposed to optical detection) is used.

RPB (Radially Polarized Beam): A beam of light has radial polarization if at every position in the beam, the polarization (electric field) vector points towards the centre of the beam.

SEM (Surface Electron Microscope): A type of electron microscope that produces images of a sample by scanning the surface with a focused beam of electrons.

SERS (Surface-enhanced Raman Scattering): A surface-sensitive technique that enhances Raman scattering by molecules adsorbed on rough plasmonic surfaces or nanostructures such as gold or silver.

SNOM (Scanning Near-field Optical Microscopy): A microscopy technique for nanostructure investigation that breaks the far-field resolution limit by exploiting the properties of evanescent waves.

SPM (Scanning Probe Microscopy): A variety of microscopy that forms images of surfaces using a physical probe that scans the specimen.

TERS (Tip-enhanced Raman Scattering): A special approach to surface-enhanced Raman spectroscopy (SERS), where enhancement of Raman

scattering occurs only at the point of a near atomically sharp tip, typically coated with gold or silver.

1. Introduction

The analysis of optically induced processes in nanostructures and single molecules can disclose extensive information about the physical and chemical phenomena, including chemical component identification, molecule conformational changes, and the kinetics of vibrational and electronic transitions. However, the diffraction limit (Rayleigh criterion [1] or Abbe limit [2]) restricts the analysis of these processes using conventional optical detection. In this case, the highest achievable spatial resolution can be defined as $\approx \frac{\lambda}{NA}$, where NA is the numerical aperture of the collecting optics, and λ is the illumination wavelength. Hence, the feasible resolution is limited if one examines a nanoscale entity with a conventional light microscope (far-field). Yet, the information about the individual nanoscopic object is only available in the optical near-field region, the region size smaller than the wavelength of the light used for observation. It has been clarified that in the presence of inhomogeneity in space this resolution limit is no longer strictly valid but, in principle, infinite confinement of light becomes, is possible [3–6].

Near-field optical microscopy is a method to boost spatial resolution without relying on prior information from the sample. Similar to atomic force microscopy (AFM), it delivers complementary details about the surface topology while imaging features near a specimen’s surface. The correlation between the source (or detector) and the sample to be imaged is a challenging task in near-field optical microscopy. This issue does not exist in standard light microscopy because the light source (e.g., the laser) is unaffected by the sample properties. Synge proposed near-field optical microscopy for the first time in 1928 [5]. He presented an instrument that is remarkably close to the current scanning near-field optical microscopy implementations: a tiny aperture in a transparent slab irradiated from one side is positioned near a sample surface, resulting in an illuminating spot that is not determined by the diffraction limit. A microscope collects the transmitted light, and its intensity is measured with a photoelectric cell. The aperture is moved in small steps across the surface to establish an image of the sample. Here the aperture size determines the resolution of such an image and not the wavelength of the incident light, as Synge correctly stated. Later, without knowing about Synge’s brilliant notion, O’Keefe presented a similar setup in 1956 [7]. In 1972 also unaware of Synge’s paper, Ash and Nichols accomplished the first experimental realization in the microwave region [8]. Ash and Nichols produced sub-wavelength imaging with a resolution of $\frac{\lambda}{60}$ using a 1.5 mm aperture lit illuminated with 10-cm waves. The emergence of scanning probe microscopy in the early 1980s [9] enabled

highly precise distance adjustment between probe and sample, paving the way for Synge’s notion to be achieved at optical frequencies. In 1984, Massey proposed [10] using piezoelectric position control to accurately position tiny lit radiated at optical frequencies. Shortly after, the challenge of subwavelength-sized aperture production was solved by Pohl, Denk, and Lanz at the IBM Rüschlikon Research Laboratory. They managed to ”pound” a metal-coated pointed quartz tip against the sample surface until some light leakage through the frontmost part could be detected, and in 1984, the IBM group presented the first subwavelength images at optical frequencies [11]. An almost simultaneous yet independent development was done by Lewis *et al.* [12]. Subsequently Betzig *et al.*, [3, 4, 13] systematically advanced and extended the technique to various applications. They showed subwavelength magnetic data storage and detection of single fluorescent molecules. Later on, the photon scanning tunneling microscope [14]; the near-field reflection microscope [15]; microscopes using luminescent centers as light-emitting sources [16]; microscopes based on local plasmon interaction; microscopes based on local light scattering [17, 18]; and microscopes relying on the field enhancement effect near sharply pointed metal tips were proposed over the years [19, 20]. These methods create a restricted photon flux between the probe and the sample. However, the confined light flux is not the only restriction limiting the feasible resolution. The photon flux must have a minimum intensity to be observable. These two requirements are rather incompatible. Thus, a balance between light confinement and light throughput must be met.

Similar to AFM, in a near-field optical microscope, a nanoscale optical probe is raster scanned across a surface, which is now termed scanning near-field optical microscopy (SNOM) [21, 22]. In SNOM, there are various possible experimental realizations to create optical near-field at the sample or the tip apex. Different configurations can be denoted depending on how the near-field is measured. In this work, we merely focus on optical microscopy with a near-field excitation source, commonly referred to as the ”tip” or ”probe”, i.e., a source with evanescent field components. This near-field is localized to the surface of the material, and depending on the material properties, the near-field intensity can be enhanced over the intensity of the irradiating light. The excitation field induces a dipole in the tip, which induces an image dipole in the sample [6]. The signal observed in the far-field is the light scattered by the effective dipole emerging from the combination of tip and sample dipoles [23]. Scattering-type scanning near-field optical microscopy (s-SNOM) [24] and tip-enhanced Raman scattering (TERS) [19, 20, 25, 26] are new techniques operating on the same principles. The highly localized information from the target sample is blended into the background signal. In these techniques, as long as the tip, the near-field excitation source, is approached to the target, the localized information will be pronounced and well-separated from the background in

the far-field. There are other techniques to assist in distinguishing near- from far-field information. To discriminate the near-field signal generated at the tip apex against the background signal associated with the diffraction-limited external irradiation, modulation techniques are furthermore practical. In some methods, the external radiation is modulated, and the optical-induced signal is detected at the same modulation frequency or higher harmonics using lock-in amplifiers. Photo-induced force microscopy (PiFM) is a novel technique based on the modulation principle [27–34]. By modulating the irradiated laser, the PiFM characterizes the optical field distribution by measuring the near-field photo-induced phenomena. i.e., the photo-induced dipole-dipole interaction force, which is highly localized and decays fast as the tip and sample distance increases. As a result, nonlocal background noise is effectively removed. Hence in PiFM, both the illumination and detection of the optical responses are in the near-field. In this mode, spectroscopic information can be gained by tuning the frequency of the excitation laser.

AFM is a powerful characterization tool and the fundamental of the near-field optics experiments used in this work. In the next chapter, after a brief overview of the working principles of the AFM, the processing of batches of the measured AFM data in a fast way is introduced. Then the presented algorithm is applied to inactivated SARS-CoV-2 samples to study their height distribution. The acquired results are in excellent agreement with measured fluorescence experiments. The third chapter focuses on modeling the probes commonly used in near-field optics. After introducing the theory behind the modeling and the FEM method, silver-coated probes are modeled in Comsol multiphysics in their "realistic" geometry. Optical properties such as near- and far-field responses followed by mechanical properties of the tip are investigated. PiFM as a new advanced SNOM technique is the subject of the study in the last chapter. It starts with an introduction of PiFM, the theory of side-band coupling, the theoretical investigation of optical forces, and then the application of PiFM. More specifically optical response of gold nanoparticles is mapped using regular AFM tips (silicon tips), which fits with the results from chapter 3.

2. AFM Data Analysis: Batch Processing

Shortly after the invention of the AFM [35], it was realized that these instruments are capable of measuring far more than surface topography. The Atomic Force Microscope (AFM) is a part of the family of scanning probe microscopes, including the scanning tunneling microscope (STM) [10, 36] and the scanning near field optical microscope (SNOM) [21]. Employing these microscopes, surface topography can be measured by raster scanning of a sharp probe across a surface and monitoring its motion. An STM operates by scanning the current flow between a probe and the surface. In the AFM, the force between a probe and the surface is mapped. Lastly, in the SNOM, the optical properties of a sample's surface are monitored. The only requirement is that a system should be modified and developed according to the desired setup.

2.1. Principles of the AFM

The force between a nanoscopic tip and the surface is generally measured with a force sensor in the microscope. The force sensor in an AFM is usually constructed from a gentle lever shown in Figure 2.1. In the lever, the output from an near-infrared (NIR) laser is focused on the backside of a cantilever and then reflected into a photo-detector with two or four blocks. The output of each photo-detector section is compared in a differential amplifier. When the tip at the end of the cantilever interacts with the surface, the cantilever bends, and the path of the NIR laser changes causing the amount of light in the two (or four) photo-detector sections to change. Thus the electronic output of the lever force sensor is proportional to the force between the probe and sample. The output of the force sensor is then sent to a feedback controller that drives a z motion generator. The feedback controller uses the force sensor output to maintain a fixed force (corresponds to the set point voltage) between the probe and the sample. Set-point voltage goes into the differential amplifier and is compared with the force sensor output voltage generating an error signal. The set point voltage controls the “relative” force. The x - y motion generator is responsible for moving the probe over the surface in the x and y axes (or the x - y piezo stage moves the sample while the tip is fixed). Finally, the motion of the probe is monitored and used to create an image of the surface.

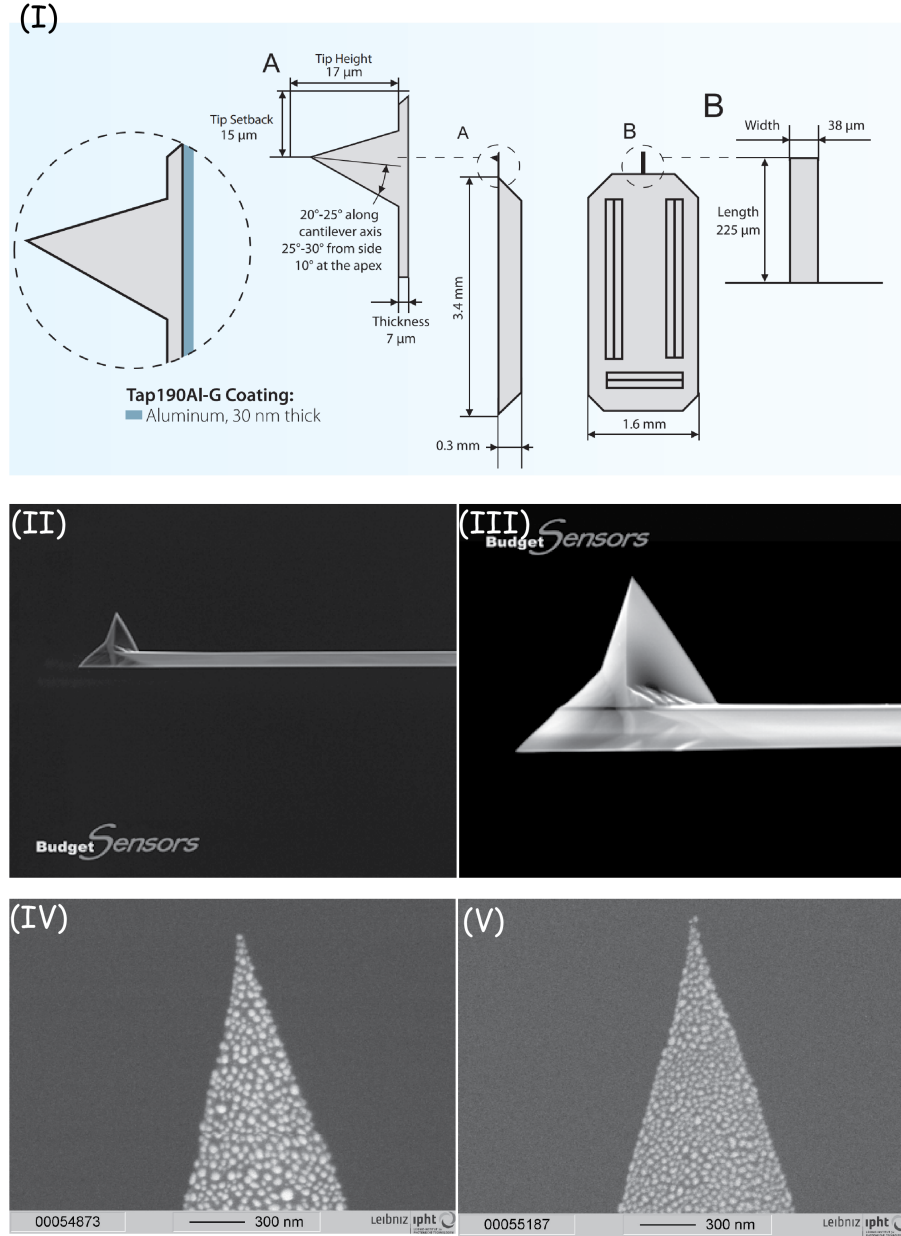


Figure 2.2: (I) Detailed geometry of a *Tap190Al-G* probe from Budget Sensors. (II) and (III) SEM images from the probe with different magnifications. (IV) and (V) SEM images from silver-evaporated plasmonic probes [37].

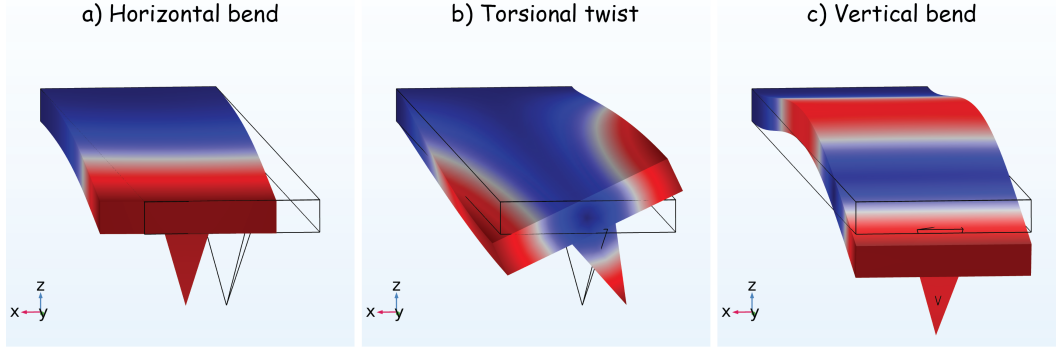


Figure 2.3: The schematic of a cantilever with horizontal bending, torsion twist, and vertical bending shown in (a), (b), and (c), respectively.

individually (more details in [3.2.5](#)).

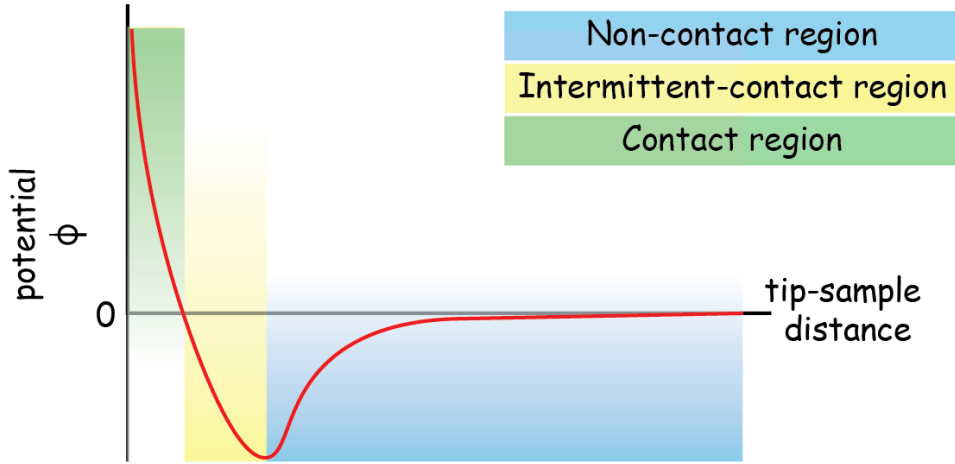


Figure 2.4: A force-distance curve representing possible measuring modes of atomic force microscopy for vertical bending of the cantilever. Contact mode in the repulsive regime ($\Phi > 0$), non-contact mode in the attractive regime ($\Phi < 0$), and the intermittent contact mode.

All the AFM measurements in this work were done while the cantilever was in a vertical-bending mode. In this case, depending on the tip-sample distance, the system can operate in contact, non-contact, and intermittent contact mode. Figure 2.4 shows a force-distance curve of a tip as a function of the tip-sample distance. Due to the Pauli principle (i.e., Coulomb interaction), the force has a repulsive behavior for small distances. In this range ($\Phi > 0$ and the green region in Figure 2.4), the AFM tip scans the sample in a contact mode. The tip has attractive behavior for larger distances due to van der Waals forces or permanent dipole-dipole interactions. In this region, one speaks of the non-contact mode ($\Phi < 0$ and the blue region in Figure 2.4). In order to

make the signal-to-noise ratio higher and thus be able to measure weaker forces with the AFM, the probe is vibrated as it is scanned across a surface. This mode is called the intermittent-contact mode (the yellow region in Figure 2.4). The intermittent-contact mode is a unique form of the contact mode in which the tip is excited to oscillate. In this mode, it is possible to bring the tip close enough to the surface and simultaneously reduce the contact with the surface. This allows the examination of sensitive samples, as well as the determination of strength or adhesion based on the phase change in the signal. All the AFM measurements in this work were done in intermittent-contact mode.

In this chapter, AFM is used as a reliable characterization tool to unravel the morphology of SARS-CoV-2 (Severe acute respiratory syndrome coronavirus 2) viruses and determine the height distribution of the samples. A series of pre- and post-processing methods to analyze the AFM data are introduced to achieve this end.

2.2. Atomic force microscopy: A suitable method for virus detection

Culture-based virus isolation has been the 'gold standard' in clinical virology, replaced by various antibody and antigen tests and molecular technologies based on real-time PCR (polymerase chain reaction). The amplification of viruses from cell culture is a time-consuming procedure that requires a suitable cell model [49]. For routine virus detection and checking the spread of disease, the most accessible analytic strategies depend solely on polymerase chain reaction (PCR) or enzyme-linked immunosorbent assay (ELISA). Estimation and identification of viral DNA or RNA are provided by PCR, whereas ELISA allows viral proteins and antiviral antibodies identification [50]. In addition to pure biologically oriented analytical techniques, imaging techniques can also contribute to the pre-classification of viruses [51].

Besides the described biological methods, physical methods are used to determine viruses' structure, such as X-ray diffraction and electron microscopy (EM). X-ray diffraction from single crystals is extraordinary in the resolution of structural detail moving toward the atomic level. In many cases, closure details of the capsid architecture become apparent with X-ray crystallography [52]. But it requires that the virus be crystallized. The main advantages of EM over X-beam diffraction is that the virus does not have to be crystallized. But it generally requires heavy metal staining or shadowing to increase contrast and requires complete dehydration, and it often involves fixatives [53]. It is ineffective when the viruses are pleiomorphic and lack architectural uniformity [54]. Another technique for virus analysis is atomic force microscopy (AFM).

Since its commercialization, AFM has been a powerful research tool pro-

viding images of biomolecules with high spatial resolution down to the atomic scale. One of the main advantages of AFM is that it works non-invasively and can be used for dynamic and high-resolution imaging of biological specimens in the dry state and the native environment ranging from single viruses, bacteria, whole cells, and tissues [50, 55, 56]. It is equally applicable to small icosahedral viruses such as Tomato bushy stunt virus, helical viruses such as tobacco mosaic virus, and completely irregular, complex viruses like the retroviruses. Thus it does not require that the virus have a uniform architecture. There is no size restriction; it has been used to analyze small plant viruses such as tobacco mosaic virus, icosahedral viruses such as Paramecium bursaria Chlorella virus, and mimivirus, the largest virus known [57–59].

SARS-CoV-2 virus is currently classified as an S3 pathogen [60], hence, a proper inactivation was crucial before transferring the material to our standard laboratory. Virus inactivation can be achieved by applying heat, alcohol, peroxide, radiation, fixatives, or detergents [61–64]. It must be taken into account that some procedures may alter the structure of viruses, which had to be avoided when investigating the morphology with an AFM. One of the most commonly used procedures to inactivate viral samples is a treatment with paraformaldehyde (PFA, polymeric form of formaldehyde). Formaldehyde reacts with amino, thiol, and hydroxyl groups and peptide linkages within proteins and forms stable methylene bridge cross-links. One of the principal advantages of cross-linking is preserving the three-dimensional architecture of the proteins. A very recent study demonstrated that it is also possible to inactivate SARS-CoV-2 using UV-C irradiation by modifying nucleic acid structure [65]. A poly-L-lysine coating was used to increase the adsorption of the virus particles to the substrate. It is known that poly-L-lysine is a positively charged polymer that absorbs very well with negatively charged glass.

Here PFA inactivated SARS-CoV-2 samples are investigated. All the AFM measurements are done using the JPK instruments. Hence, AFM data acquired with JPK systems are in JPK file formats, which are challenging to process. The task gets more challenging when batches of data need to be processed. Developing an efficient and fast way to process and analyze sets of JPK data is the main goal of this chapter.

2.3. Batch Processing

2.3.1. Pre-processing algorithm

Generally, JPK files can only be opened and then processed with commercially available softwares such as Gwyddion [66, 67] and JPKSPM Data Processing [68]. In the processing steps, some techniques are commonly used

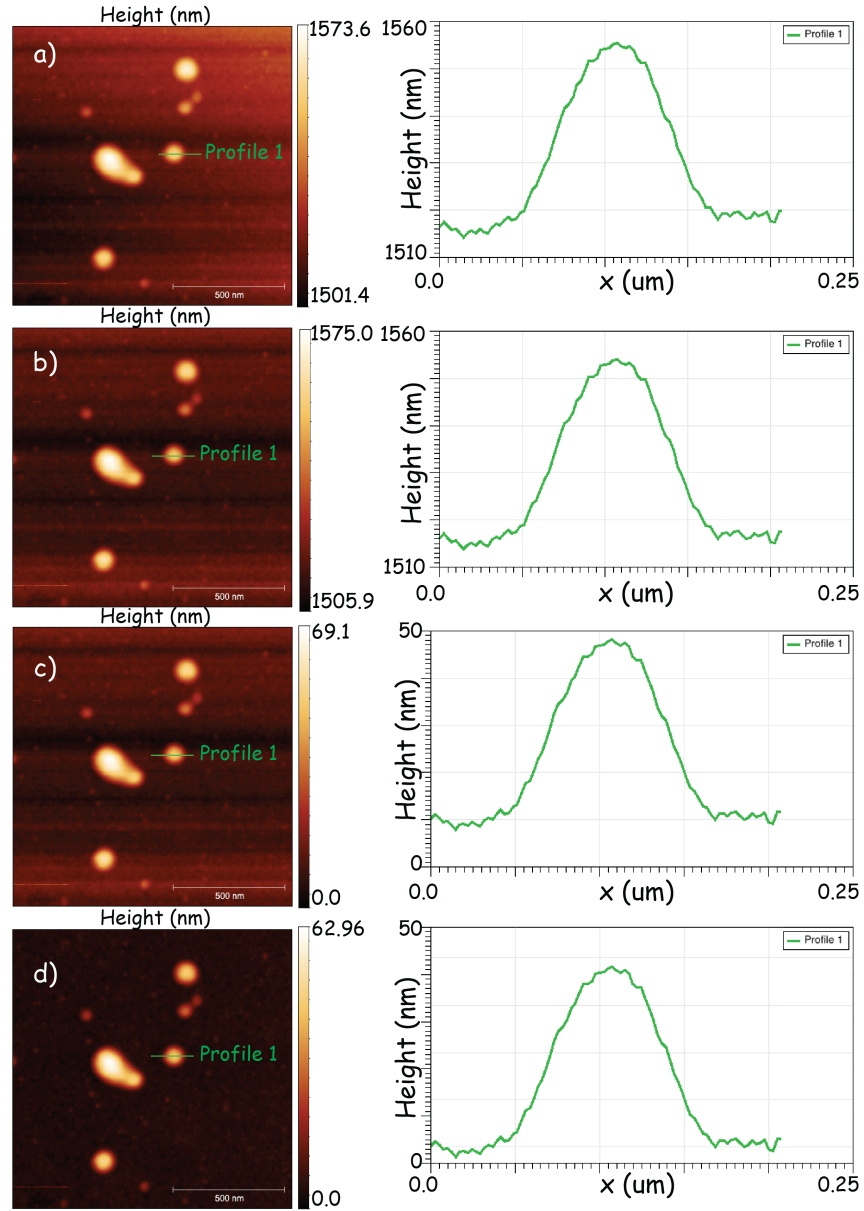


Figure 2.5: Height channel of the raw AFM images (a), after plane leveling (b), after normalization to minimum (c) and after background subtraction (d) and their corresponding line profiles.

to convert the JPK data to a PNG file so that the data can be presented anywhere. The data obtained from SPM microscopes are often not leveled at all (see Figure 2.5 (a)). The microscope directly outputs raw data values computed from piezoscanner voltage. This way of exporting data enables the user to choose their method of leveling data. Plane leveling is usually one of the first functions applied to raw data. During the AFM, line scans might face a height drift, so an actual plane surface might not be recorded correctly. For this artifact, the plane is computed from all the image points and is subtracted from the data (see Figure ?? (b)). Since the data range during the measurements can be different and not necessarily starts from zero, fixing to zero is the next step in pre-processing procedure. In this step, a constant is added to all the data to move the minimum to zero (see Figure 2.5 (c)). These steps should be sufficient to save the data, with the scalebar, in an i.e., PNG file. It takes more than 30 seconds to open a single JPK file, apply the aforementioned pre-processing, and save it to a PNG file. It takes more time when more pre-processing, such as background subtraction, is needed. Sometimes the target sample is placed on the top of an adsorbing layer, and the task is to obtain the height values of the target sample only. In this case, the height of the adsorbing layer should be removed from the data (see Figure 2.5 (d)). Since it takes considerable amount of time for a single file, it would be challenging to repeat the same procedure for batches of the JPK data. Hence, it is crucial to have a algorithm that processes the data systematically.

To process batches of the AFM data measured in the JPK file format, *Python* programming language is used to develop an algorithm to process batches of data. All the analysis has been done on MacBook Pro (2016) with 3.3 GHz Dual-Core Intel Core i7 processor, and 16 GB 2133 MHz LPDDR3 memory. Gwyddion software is already installed in the system because Python-compatible libraries of Gwyddion are used to read the JPK files. These libraries, i.e., *pygwy*, are only consistent with *Python2*. Hence, all the other libraries, i.e., *Matplotlib*, *Numpy*, *OpenCV*, etc., used in the scripts should be compatible with *Python2*. In the Python script, first the directory of the *Python2* site package should be provided. In the case of our system it is:

```
/opt/local/Library/Frameworks/Python.framework/Versions/2.7/lib
/python2.7/site-packages
```

The next crucial directory that should be pointed to is the *pygwy*, which in our case is:

```
/opt/local/share/gwyddion/pygwy
```

These directories should be changed and adjusted depending on the operating system.

After properly adjusting those packages, existing JPK files in the directory, can be loaded iteratively. Each JPK file consists of data and corresponding metadata (name of the measurement, date, measured channels, etc). So in each iteration in the script, respective data from the channel, i.e. "Height"

can be selected. Now with the developed script, which is available online [69] the commonly used procedures (shown in Figure 2.5) to read, process, and save the 340 JPK files took less than 45 seconds.

2.3.2. Post-processing algorithm

Now that JPK files can be processed quickly, further analysis of the files is also achievable. In the following, two major post-processing applications are introduced.

In-situ pre-characterization tool

By reading a JPK file, the user can access all the metadata from the file. So the algorithm can be used for the pre-characterization tool to select specific targets within the sample. There might be cases where specimens of different sizes are in the sample, but not all are required for further analysis. Imagine a case where a sample includes a variety of specimen sizes, here height distribution, can be seen in the AFM image. However, the user needs further measurements, i.e., Raman or TERS, on selected targets. Here an algorithm can be used to help the user. In this case, an AFM image from the sample can be taken and fed to the algorithm for some pre-processing techniques and be prepared for further analysis.

Such a pre-processed image is shown in Figure 2.6 (a). The first step is to set a threshold regarding the maximum height in the image. By doing this, that specific height plane divides, or masks, the whole sample into two binary areas: areas with height values higher than the selected threshold are replaced by 1 and the rest are replaced by zero. In Figure 2.6 (b) and (c), all the green areas are the selected areas that are substituted by the value of 1. This technique is called masking. The created maps, including masks, are in a separate data range (0 and 1). Depending on the selected height threshold, different masked areas can be selected. As it can be seen from Figure 2.6 (b), by choosing $0.8 \times \text{Height}_{max}$ as the input threshold, two big specimens are distinguishable and well separated. Still, the smaller, and maybe interesting, targets are not selected. On the other hand, by lowering the threshold (see Figure 2.6 (c)), these smaller regions are chosen, but those two bigger targets are now picked as one entity. As the last step, the user can provide a range of height values of the interesting targets for further measurements. In this case, extreme values, too small or too big, are neglected (Figure 2.6 (d)). Now that the targets are properly selected, the computer vision algorithm, *OpenCV* library, can be used to find the center of mass coordinates of the selected areas with respect to the original measured file. Figure 2.7 displays coordinates of

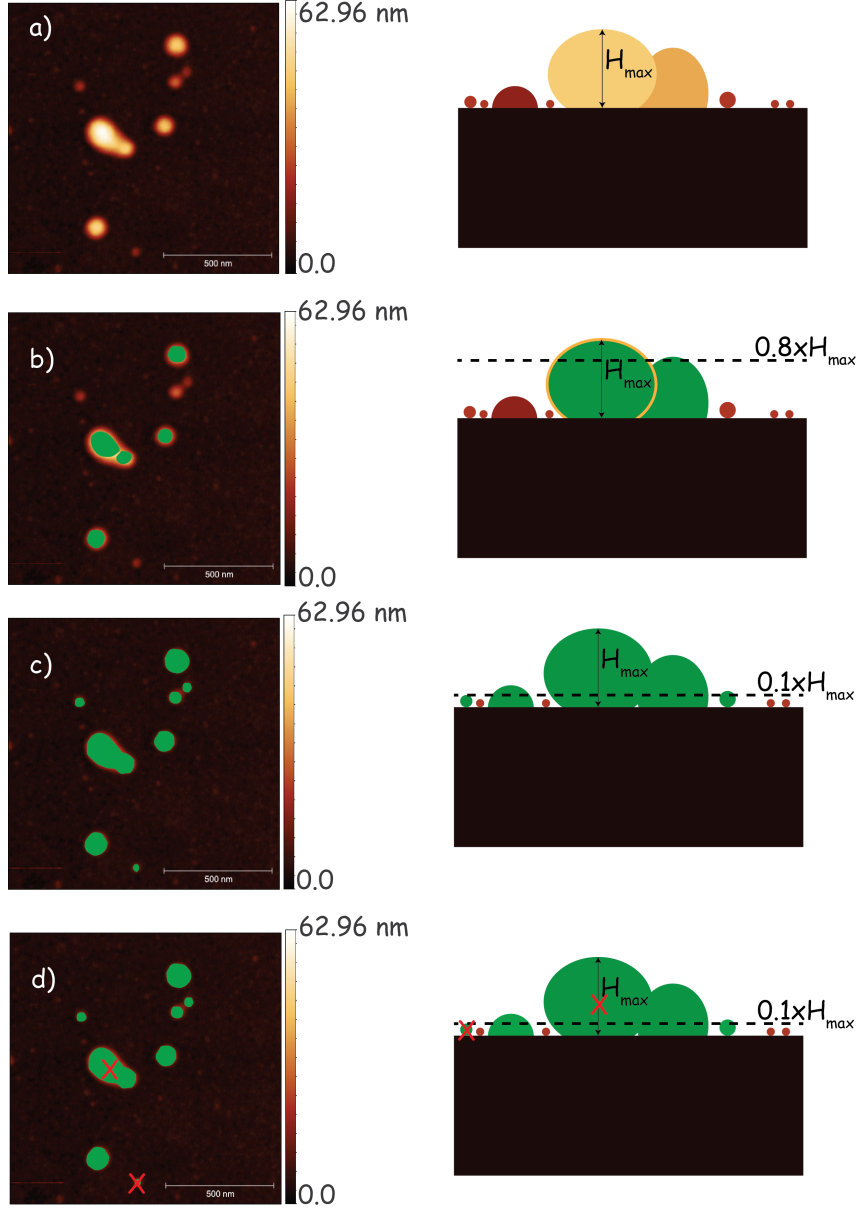


Figure 2.6: Height channel of pre-processed AFM image (a) and selected targets based on 0.8 threshold (b) and 0.1 threshold (c) and their corresponding scheme. Final selected targets based on the extreme height values of the target. For instance if the height of the selected targets are bigger than "X" or smaller than "Y" (nm)(d).


```

File name: save-2020.05.25-13.41.59.418.jpk
Coordinate (x,y) (in um): -16.243128250112356,27.582709908840936

Coordinate (x,y) (in um): -16.586849901057466,27.33699992064545

Coordinate (x,y) (in um): -17.315212447107818,27.173193261848457

Coordinate (x,y) (in um): -17.298844749443763,27.148622263028912

```

Figure 2.7: Representation of using computer vision to process the AFM data in the *in-situ* mode. Here the coordinates of the selected targets are shown.

the selected targets within a sample. Now instead of the whole image or a random selection of the regions, the next experiments can be done around the specific coordinate.

In a nutshell, the user can take an AFM measurement, run the script and feed the measured file to the script, provide input thresholds, and then algorithms used in the script will provide information similar to that shown in Figure 2.7, which can be used for further measurements.

Batch analysis tool

```

File name: save-2020.05.25-13.41.59.418.jpk
Coordinate (x,y) (in um): -16.243128250112356,27.582709908840936 Height (in nm): 38.52639637162653
Coordinate (x,y) (in um): -16.586849901057466,27.33699992064545 Height (in nm): 71.34617746621097
Coordinate (x,y) (in um): -17.315212447107818,27.173193261848457 Height (in nm): 21.936399809399607
Coordinate (x,y) (in um): -17.298844749443763,27.148622263028912 Height (in nm): 22.070374809454098

```

Figure 2.8: Representation of using computer vision to process the AFM data in the *in-situ* mode. Here the coordinates of the selected targets together with the corresponding heights are shown.

In the previous section, computer vision was used to reveal each masked region's center of mass coordinate. By pointing to the coordinates inside the original pre-processed image (Figure 2.6 (a)), the actual height of the target can be accessed (see Figure 2.8). This algorithm can be used to display height distribution statistics from batches of the measured AFM data. In this case, all the JPK files in the current directory will be read, pre-processed (Figure 2.5), processed (Figure 2.6), and then the height of the selected maps are stored. Figure 2.9 shows statistics from the SARS-CoV-2 height distribution of 350 measurements, which are selected in the algorithm explained in the previous section. 80% and 10% of maximum height, H_{max} , values are chosen as the thresholds for Figure 2.9 (a) and (b), respectively. Entities with the height of around 30, 60, and 80 nm have more counts in both cases, which agrees with the other works [70]. On the other hand, entities with height values up to

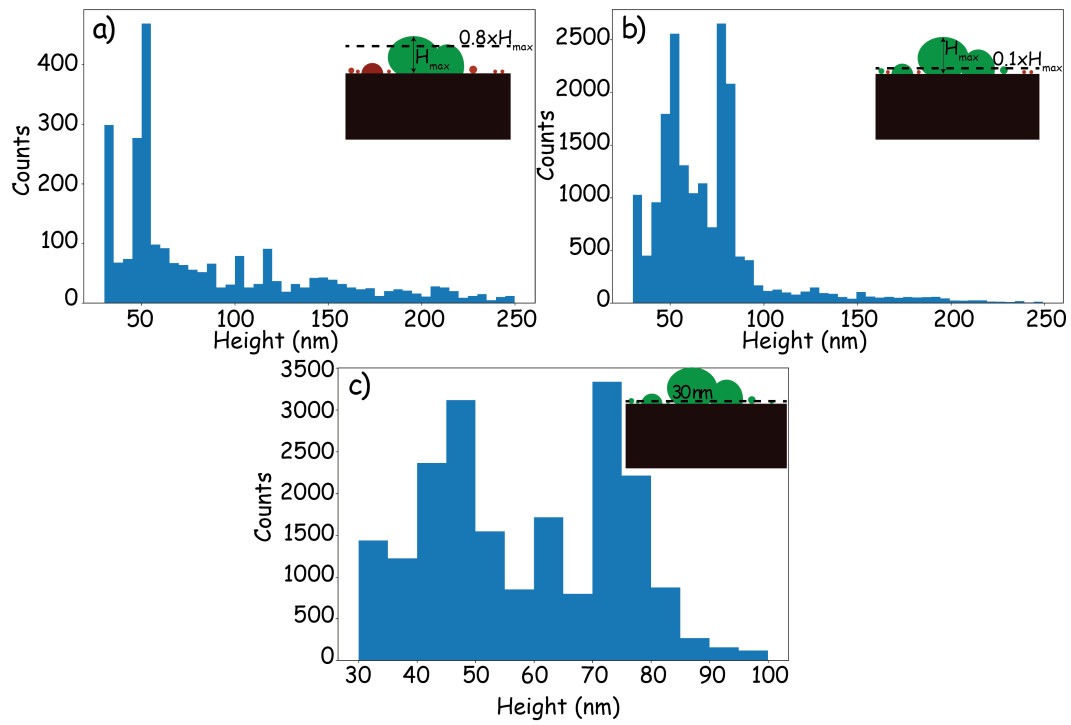


Figure 2.9: Height distribution of SARS-CoV-2 virus acquired from 350 measurements (JPK files) for 0.8 of maximum height as threshold (a) and 0.1 of maximum height as threshold (b) and absolute value of 30 nm as threshold (c).

250 nm are also selected. The main reason for the appearance of such objects could be the aggregation of small particles and the assembly of clusters on top of each other, so extreme height values appear in the statistics. Consequently, by choosing a higher value as the threshold, entities with a height lower than the threshold are not selected. It can be seen clearly by comparing the number of counts for both plots in Figure 2.9. In order to examine this, same analysis but with absolute value (here 30 nm) as threshold was performed. 2.9 (c) shows that by choosing an absolute value as threshold instead of relative values (percentage of maximum in each image) small size targets hidden in an image where bigger targets exist, can be accessed. This clearly shows the difference between two threshold aspects in the image analysis approaches. It should be mentioned for the later case we intentionally neglected the targets bigger than 100 nm. The results are shown in Figure 2.10 as a boxplot. Boxplots are one of the standardized ways of displaying the distribution of data based on a five-number summary (*minimum*, first quartile ($Q1$), median, third quartile ($Q3$), and *maximum*). The range between $Q1$ (25th percentile) and $Q3$ (75th percentile) is interquartile range (IQR). So the *minimum* and *maximum* can be defined as $Q1 - 1.5 \times IQR$ and $Q3 + 1.5 \times IQR$, respectively. Figure 2.10 shows a boxplot with the aforementioned values (middle) and its corresponding nearly normal distribution and the probability density function (pdf) for a normal distribution (top). In Figure 2.10 top and middle, it can be seen that 50% of the data are inside the box and the line inside it represents the median value of the whole data. 99.3% of the whole data are inside the range from *minimum* and *maximum*. The data outside this range, whose counts are less than 0.35% of the entire data, are called outliers (the green spheres in Figure 2.10 middle). By presenting the results from Figure 2.9 in a boxplot format (Figure 2.10 bottom), it can be seen that, for instance, in case of 10% of H_{max} as the threshold, 50% of the viruses have the height between 50 to 80 nm; and 99.3% of them have the height between 30 to 125 nm. In addition, the median height value of the viruses are 60-70 nm.

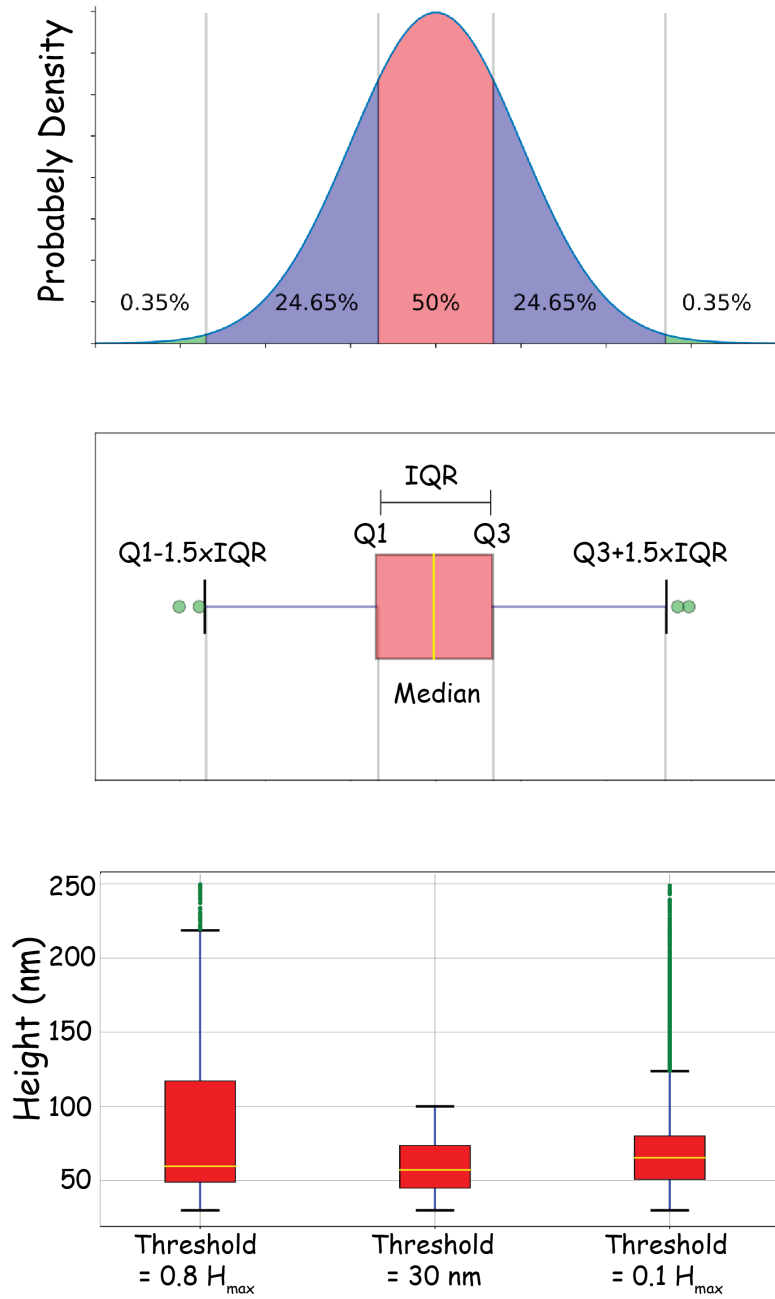


Figure 2.10: Representation of a hypothetical normal distribution (top) in its corresponding boxplot format (middle) and the height distribution of SARS-CoV-2 samples from Figure 2.9 in a box plot format (bottom).

3. Modeling the Probes

3.1. Background and the theory

Designing and developing an efficient setup for SNOM-type experiments requires extensive modeling. This thesis deals with the theoretical consideration of modeling the near-field optics, specifically tip-enhanced Raman spectroscopy (TERS) and photo-induced force microscopy (PiFM). Therefore, a comprehensive introduction is necessary. At first, Maxwell equations, wave optics, and Laguerre-Gaussian beams are introduced. After that, plasmonic interactions will be considerably described. The finite element method (FEM) as the primary approach for the models will be presented. Then FEM is used to model tightly focused linearly polarized beam (LPB), radially polarized beam (RPB), azimuthally polarized beam (APB) and their behavior in nano-optic interactions.

3.1.1. Maxwell's equations

Maxwell's equations are a set of coupled equations that describe the world of electromagnetics. These equations describe how electric and magnetic fields propagate, interact, and how entities influence them.

James Clerk Maxwell took a set of known experimental laws (Faraday's Law, Ampere's Law) and unified them into a symmetric coherent set of equations known as Maxwell's equations. He presented them for the first time in 1864 in the paper *A Dynamical Theory of the Electromagnetic Field* in London [71]. This work originally contained eight equations, each of which had two expressions for the electromagnetic force and the electromagnetic moment. Later, with the help of O. Heaviside and J. W. Gibbs, among others, the equations were simplified to the four microscopic known today. By assumptions for linear and isotropic media, $\mathbf{B} = \mu\mathbf{H}$ and $\mathbf{D} = \epsilon\mathbf{E}$ give rise to the familiar equations. Here \mathbf{H} is magnetic field, \mathbf{B} is magnetic flux density, \mathbf{D} is electric flux density, \mathbf{E} is electric field, μ is permeability, and ϵ is permittivity. The first equation, in differential representation, is Gauss's law:

$$\nabla \cdot \mathbf{E} = \frac{\rho}{\epsilon_0} \quad (3.1)$$

This describes the divergence ($\nabla \cdot$) of electric field lines in the presence of an electric charge. Where ρ describes the electric charge density and ϵ_0 the

permittivity in free space.

The second equation is Gauss's law for magnetic fields:

$$\nabla \cdot \mathbf{B} = 0 \quad (3.2)$$

This is analogous to the first equation, except that this one describes the magnetic field. But since there are no proven magnetic monopoles, besides in quasi-particles [72], this term is set to zero. The third equation is the law of induction:

$$\nabla \times \mathbf{E} = -\frac{\partial \mathbf{B}}{\partial t} \quad (3.3)$$

This describes that the time change (∂t) of a magnetic field (\mathbf{B}) leads to a vortex electric field ($\nabla \times \mathbf{E}$). The vortex is expressed by $\nabla \times$. The fourth equation is the extended Ampère's circuital law (with Maxwell's addition).

$$\nabla \times \mathbf{B} = \mu_0 \mathbf{j} + \mu_0 \epsilon_0 \frac{\partial \mathbf{E}}{\partial t} \quad (3.4)$$

This describes that time-varying electric fields ($\frac{\partial \mathbf{E}}{\partial t}$) and the displacement current ($\mu_0 \mathbf{j}$), lead to vortex magnetic fields ($\nabla \times \mathbf{B}$), where \mathbf{j} is the electric current density and μ_0 is the vacuum permeability.

With the help of these differential equations, various electrodynamic or electrostatic, which are mainly used in this work, can be solved.

3.1.2. Wave optics

To describe the electromagnetic fields of a laser beam, it is necessary to introduce the theory of wave optics. Based on that, Gaussian and Laguerre-Gaussian beam profiles are derived. In this thesis, we will mainly deal with Gaussian and Laguerre-Gaussian beam fields with transverse electromagnetic mode (TEM) because this mode is sufficient for the description of the experiments. For the calculation of the Laguerre-Gaussian (LG) beam profiles, it is also helpful to introduce higher-order modes (e.g., LG_{01}) in cylindrical coordinates. With this, radially and azimuthally polarized fields can be generated on the substrate surface [73–77]. The wave equation (Helmholtz equation) serves as the starting point for the calculation.

$$\nabla^2 E(r, t) - \mu_0 \epsilon_0 \frac{\partial^2 E(r, t)}{\partial t^2} = 0 \quad (3.5)$$

In order to solve this equation, the following time-dependent wave should be considered:

$$E(r, t) = u(x, y, z) \cdot e^{-i(kz - \omega t)} \quad (3.6)$$

Here, $u(x, y, z)$ is a complex scalar function which describes the non-planar part of the wave. By inserting equation 3.6 into the wave equation and using the paraxial approximation, the paraxial Helmholtz equation for the stationary case is obtained.

$$\nabla_{\perp}^2 u(x, y, z) + 2ik \frac{\partial u(x, y, z)}{\partial z} = 0 \quad (3.7)$$

In the paraxial approximation, changes in amplitude in the z -direction are very small. ∇^2 thus becomes modified to $\nabla_{\perp}^2 \equiv \frac{\partial^2}{\partial x^2} + \frac{\partial^2}{\partial y^2}$ [78] and equation 3.7 will be reformed as:

$$\frac{\partial^2 u}{\partial x^2} + \frac{\partial^2 u}{\partial y^2} + 2ik \frac{\partial u}{\partial z} = 0 \quad (3.8)$$

By introducing cylindrical coordinates, the equation can be expressed as follows:

$$\frac{\partial^2 u}{\partial r^2} + \frac{1}{r} \frac{\partial u}{\partial r} + 2ik \frac{\partial u}{\partial z} = 0 \quad (3.9)$$

Then, the solution of this paraxial Helmholtz equation is:

$$u(r, z) = A(z) \cdot e^{-\frac{ikr^2}{2q(z)}} \quad (3.10)$$

where A and q are two complex functions (of z only), which remain to be determined. This expression for u looks something like a Gaussian distribution. To obtain the unknown terms in equation 3.10, we substitute this expression for u into the axially symmetric paraxial wave equation, 3.9 and obtain

$$-2ik \left(\frac{A}{q} + \frac{\partial A}{\partial z} \right) + \frac{k^2 r^2 A}{q^2} \left(\frac{\partial q}{\partial z} - 1 \right) = 0 \quad (3.11)$$

Since this equation must be satisfied for all r as well as all z , and given that the first part depends only on z while the second part depends on r and z , the two parts must individually be equal to zero. This gives us two relationships that must be simultaneously satisfied:

$$\frac{\partial q}{\partial z} = 1 \quad (3.12)$$

$$\frac{\partial A}{\partial z} = -\frac{A}{q} \quad (3.13)$$

Equation 3.12 has the solution

$$q(z) = q(z_0) + (z - z_0) \quad (3.14)$$

Without loss of generality, we define the reference position along the z axis to be $z_0 = 0$, which yields

$$q(z) = q(0) + z \quad (3.15)$$

The function q is called the complex beam parameter (since it is complex), but it is often simply referred to the beam parameter or Gaussian beam parameter. Since it appears in equation 3.10 as $\frac{1}{q}$, it is reasonable to write

$$\frac{1}{q} = \left(\frac{1}{q}\right)_r - i \left(\frac{1}{q}\right)_i \quad (3.16)$$

where the subscripted terms are the real and imaginary parts of the quantity $\frac{1}{q}$, respectively. Substituting into equation 3.10, the exponential term becomes

$$\exp\left(\frac{-ikr^2}{2q}\right) = \exp\left[\left(\frac{-ikr^2}{2}\right) \left(\frac{1}{q}\right)_r - \left(\frac{kr^2}{2}\right) \left(\frac{1}{q}\right)_i\right] \quad (3.17)$$

The imaginary term has the form of the phase variation produced by a spherical wave front in the paraxial limit. We can see this starting with an equi-phase surface having radius of curvature R and defining $\phi(r)$ to be the phase variation relative to a plane for a fixed value of z as a function of r as shown in Figure 3.1. In the limit $r \ll R$, the phase delay incurred is approximately equal to

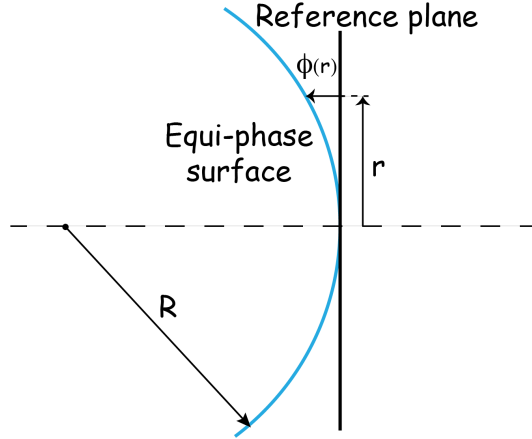


Figure 3.1: Phase shift, $\phi(r)$, of spherical wave with radius of curvature of R relative to plane wave at distance r from axis defined by propagation direction.

$$\phi(r) \cong \frac{\pi r^2}{\lambda R} = \frac{kr^2}{2R} \quad (3.18)$$

We thus make the important identification of the real part of $\frac{1}{q}$ with the radius of curvature of the beam

$$\left(\frac{1}{q}\right)_r = \frac{1}{R} \quad (3.19)$$

Since q is a function of z , it is evident that the radius of curvature of the beam will depend on the position along the axis of propagation.

The second part of the exponential in equation 3.17 is real and has a Gaussian variation as a function of the distance from the axis of propagation. Taking the standard form for a Gaussian distribution to be

$$f(r) = f(0) \exp \left[- \left(\frac{r}{r_0} \right)^2 \right] \quad (3.20)$$

to make the second part of equation 3.17 be of the following format, we take

$$\left(\frac{1}{q} \right)_i = \frac{2}{kw^2(z)} = \frac{\lambda}{\pi w^2} \quad (3.21)$$

and thus define the beam radius w , which is the value of the radius at which the field falls to $\frac{1}{e}$ of its on-axis value. Since q is a function of z , the position along the axis of propagation, the beam radius as well as the radius of curvature will depend on z too. With these definitions, we see that the function q is given by

$$\frac{1}{q} = \frac{1}{R} - \frac{i\lambda}{\pi w^2} \quad (3.22)$$

where both R and w are functions of z and the real part describes the radius of curvature and the imaginary part describes the phase difference of the wave front at position z . In these equations

$$z_R = \frac{\pi \omega_0^2}{\lambda} \quad (3.23)$$

is the Rayleigh range. At a distance from the waist equal to the Rayleigh range z_R , the width w of the beam is $\sqrt{2}$ larger than it is at the focus where $w = w_0$, the beam waist. That also implies that the on-axis ($r = 0$) intensity there is one half of the peak intensity (at $z = 0$) [78]. From equation

3.10, at $z = 0$, $u(r, 0) = A(0) \exp[-ikr^2/2q(0)]$, and if w_0 is chosen such that $w_0 = [\lambda q(0)/i\pi]^{1/2}$, the relative field distribution at $z = 0$ can be written as:

$$u(r, 0) = u(0, 0) \exp \left(\frac{-r^2}{w_0^2} \right) \quad (3.24)$$

where w_0 denotes the beam radius at $z = 0$, which is called the beam waist radius. With this definition and equation 3.15 a second important expression for q can be shown as:

$$q = \frac{i\pi w_0^2}{\lambda} + z \quad (3.25)$$

Equations 3.22 and 3.25 together allow us to obtain the radius of curvature and the beam radius as a function of position along the axis of propagation:

$$R(z) = z + \frac{1}{z} \left(\frac{\pi w_0^2}{\lambda} \right) \quad (3.26)$$

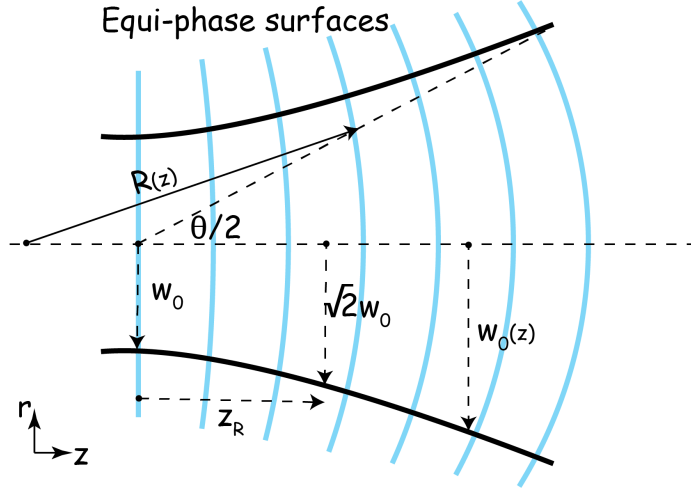


Figure 3.2: Cut through beam showing equi-phase surfaces (dashed blue lines), beam radius: $w_0(z)$; $R(z)$: radius of curvature ; w_0 : beam waist; z_R : Rayleigh range; θ : total angular spread.

$$w(z) = w_0 \left[1 + \left(\frac{\lambda z}{\pi w_0^2} \right)^2 \right]^{\frac{1}{2}} \quad (3.27)$$

It is clear now that the beam waist radius is the minimum value of the beam radius and it occurs at the beam waist, where the radius of curvature is infinite (characteristic of a plane wave front). The behavior of the radius of curvature is shown schematically in Figure 3.2.

To complete our analysis of the basic Gaussian beam equation, the second part of the equations 3.11, which is obtained from substituting our trial solution in the paraxial wave equation, should be used. Using equations 3.12, 3.13, 3.26 and 3.27 following relation can be derived:

$$\frac{A(z)}{A(0)} = \frac{1 + \frac{i\lambda z}{\pi w_0^2}}{1 + \left(\frac{i\lambda z}{\pi w_0^2} \right)^2} \quad (3.28)$$

It is convenient to express this in terms of a the Gouy phase (Gaussian beam phase shift). At position z the Gouy phase of a fundamental Gaussian beam is given by:

$$\phi_0 = \arctan\left(\frac{z}{z_R}\right) \quad (3.29)$$

$$\tan \phi_0 = \frac{\lambda z}{\pi w_0^2} \quad (3.30)$$

so

$$\frac{A(z)}{A(0)} = \frac{w(z)}{w_0} \tan \phi_0 \quad (3.31)$$

By taking E_0 as the amplitude of the beam at the beam waist, the complete expression for the fundamental Gaussian beam mode can be written as:

$$u(r, z) = E_0 \frac{w_0}{w(z)} \exp \left(\frac{-r^2}{w(z)^2} - \frac{i\pi r^2}{\lambda R(z)} + i\phi_0 \right) \quad (3.32)$$

The expression for the electric field can be obtained immediately using equation 3.6 as follows:

$$E(r, z) = E_0 \frac{w_0}{w(z)} \exp \left(\frac{-r^2}{w(z)^2} - ikz - \frac{i\pi r^2}{\lambda R(z)} + i\phi_0 \right) \quad (3.33)$$

For the case of Cartesian coordinates, simply substituting $r^2 = x^2 + y^2$ and by adding the time, the complete form of the electric field has the following form:

$$E(x, y, z, t) = E_0 \frac{w_0}{w(z)} \exp \left(\frac{-(x^2 + y^2)}{w(z)^2} - i(kz - \omega t) - \frac{i\pi(x^2 + y^2)}{\lambda R(z)} + i\phi_0 \right) \quad (3.34)$$

3.1.3. Correction of the field by numerical aperture

Since the laser beam in experimental setups is guided through complex optics (e.g., objectives, beam expanders) onto the sample, it is necessary to correct the field. Here it is assumed that the laser beam is collimated at the beginning and focused with a particular numerical aperture (NA) on the sample. By introducing the beam's divergence (θ in Figure 3.2) and NA as below:

$$\theta = \arctan \left(\frac{\lambda}{\pi n_s w_0} \right) \quad (3.35)$$

$$NA = n_s \cdot \sin(\alpha) \quad (3.36)$$

where again λ is the wavelength, w_0 is the beam waist, and n_s is the refractive index of the medium. By assuming θ and α as identical values for the incident beam, equations 3.35 and 3.36 can be combined as follows.

$$\sin^{-1} \left(\frac{NA}{n_s} \right) = \tan^{-1} \left(\frac{\lambda}{\pi w_0} \right) \quad (3.37)$$

After simple rearrangement of the equation and insertion of the Rayleigh range, it will form as below:

$$z_R = \frac{w_0}{\tan \left[\sin^{-1} \left(\frac{NA}{n_s} \right) \right]} \quad (3.38)$$

However, this equation gives real results only when $n_s \geq NA$. Assuming the small angle approximation, equation 3.38 can be simplified to the following:

$$z_R = \frac{w_0}{NA} \quad (3.39)$$

This equation shows that, using the given NA of the objective lens Rayleigh length or in other words the Gaussian beam can be modulated.

3.1.4. Laguerre-Gaussian beam

The effect of the different polarizations is also part of this thesis. More specifically, RPB and APB are intriguing to consider. These beam profiles, which are circularly symmetric (or lasers with cavities that are cylindrically symmetric), are often best solved using the Laguerre-Gaussian modal decomposition [79]. Here the derivation of the equations for a Laguerre-Gaussian beam is presented. For this purpose, the solution of the paraxial wave equation in cylindrical coordinates (equation 3.33) is used. In addition, it is convenient to describe radial symmetric modes with Laguerre polynomials ($L_{p,m}$) where p represents the radial order and m the azimuthal order of the modes. Thus the equation changes as follows [80].

$$\begin{aligned} E_{p,m}(r, \theta, z, t) = & \frac{E_0}{w(z)} \sqrt{\frac{2p!}{\pi(p+m)!}} \left(\frac{r\sqrt{2}}{w(z)} \right)^m L_{p,m} \left(\frac{2r^2}{w(z)^2} \right) \\ & \times \exp \left(\frac{-r^2}{w(z)^2} - ikz - \frac{i\pi r^2}{\lambda R(z)} + i(2p+m+1)\phi_0 + im\theta \right) \end{aligned} \quad (3.40)$$

The Laguerre polynomials are usually represented by the Rodrigues formula.

$$L_{p,m}(r) = \frac{e^r r^{-m}}{p!} \frac{d^p}{dr^p} (e^r r^{p+m}) \quad (3.41)$$

In this work we are mostly interested in radial mode of $p = 0$ and azimuthal mode of $m = 1$. Therefore, in this specific case:

$$L_{0,1}(r) = 1 \quad (3.42)$$

By applying this assumption to equation 3.40 and inserting the polynomial, the following equation can be obtained:

$$\begin{aligned} E_{0,1}(r, \theta, z, t) = & \frac{E_0}{w(z)} \sqrt{\frac{2}{\pi}} \left(\frac{r\sqrt{2}}{w(z)} \right) \\ & \times \exp \left(\frac{-r^2}{w(z)^2} - ikz - \frac{i\pi r^2}{\lambda R(z)} + i2\phi_0 + i\theta \right) \end{aligned} \quad (3.43)$$

From this equation it can be seen that the last term ($e^{i\theta}$) is crucial for the description between radially and azimuthally polarized light [76]. This term can be represented by Euler's formula ($e^{i\theta} = \cos(\theta) + i \sin(\theta)$) in the form of unit vectors for radially (\hat{e}_{radial}) and azimuthally ($\hat{e}_{azimuthal}$) polarized light as follows:

$$\hat{e}_{radial} = \begin{pmatrix} \cos(\theta) \\ \sin(\theta) \end{pmatrix} \quad (3.44)$$

$$\hat{e}_{azimuthal} = \begin{pmatrix} -\sin(\theta) \\ \cos(\theta) \end{pmatrix} \quad (3.45)$$

Since the unit vectors in Cartesian coordinates are also required for later numerical calculations, it is necessary to present them.

$$\hat{e}_{radial} = \begin{pmatrix} \frac{x}{\sqrt{x^2+y^2}} \\ \frac{y}{\sqrt{x^2+y^2}} \end{pmatrix} \quad (3.46)$$

$$\hat{e}_{azimuthal} = \begin{pmatrix} \frac{-y}{\sqrt{x^2+y^2}} \\ \frac{x}{\sqrt{x^2+y^2}} \end{pmatrix} \quad (3.47)$$

By substituting each of these terms into equation 3.43, the complete form of electric field with radial polarization will be:

$$\begin{aligned} E_{0,1}(x, y, z, t) &= \frac{E_0}{w(z)} \sqrt{\frac{2}{\pi}} \left(\frac{\sqrt{2(x^2+y^2)}}{w(z)} \right) \\ &\times \exp \left(\frac{-(x^2+y^2)^2}{w(z)^2} - ikz - \frac{i\pi(x^2+y^2)^2}{\lambda R(z)} + i2\phi_0 + i\theta \right) \frac{x}{\sqrt{x^2+y^2}} \end{aligned} \quad (3.48)$$

$$\begin{aligned} E_{0,1}(x, y, z, t) &= \frac{E_0}{w(z)} \sqrt{\frac{2}{\pi}} \left(\frac{\sqrt{2(x^2+y^2)}}{w(z)} \right) \\ &\times \exp \left(\frac{-(x^2+y^2)^2}{w(z)^2} - ikz - \frac{i\pi(x^2+y^2)^2}{\lambda R(z)} + i2\phi_0 + i\theta \right) \frac{y}{\sqrt{x^2+y^2}} \end{aligned} \quad (3.49)$$

Same procedure for the azimuthally polarized beam will result:

$$\begin{aligned} E_{0,1}(x, y, z, t) &= \frac{E_0}{w(z)} \sqrt{\frac{2}{\pi}} \left(\frac{\sqrt{2(x^2+y^2)}}{w(z)} \right) \\ &\times \exp \left(\frac{-(x^2+y^2)^2}{w(z)^2} - ikz - \frac{i\pi(x^2+y^2)^2}{\lambda R(z)} + i2\phi_0 + i\theta \right) \frac{-y}{\sqrt{x^2+y^2}} \end{aligned} \quad (3.50)$$

$$E_{0,1}(x, y, z, t) = \frac{E_0}{w(z)} \sqrt{\frac{2}{\pi}} \left(\frac{\sqrt{2(x^2 + y^2)}}{w(z)} \right) \times \exp \left(\frac{-(x^2 + y^2)^2}{w(z)^2} - ikz - \frac{i\pi(x^2 + y^2)^2}{\lambda R(z)} + i2\phi_0 + i\theta \right) \frac{x}{\sqrt{x^2 + y^2}} \quad (3.51)$$

3.1.5. Principles of light matter interaction at nanoscale

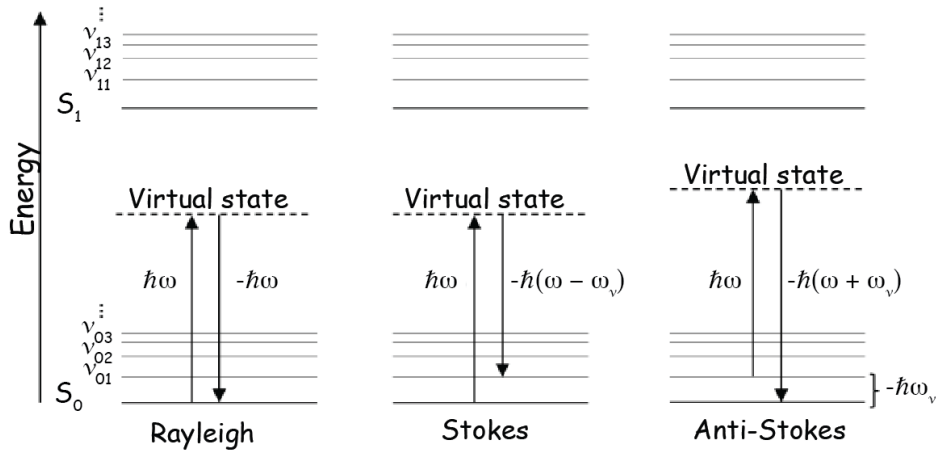


Figure 3.3: Energy diagram of light scattering processes on bound electrons. S_0 describes the ground state and S_1 the first excited state. Each of these has different vibrational states, which are denoted by v_{xx} . Rayleigh scattering is an elastic scattering process, whereas Stokes and anti-Stokes scattering are inelastic processes.

Raman spectroscopy

According to the Jablonski diagram in Figure 3.3, the relationship between the light wavelength and the energy needed for vibrational or electronic transitions in the molecule determines the type of light-matter interaction [81]. When infrared light (IR) of mid-infrared wavelengths ($4\text{--}20\ \mu\text{m}$) is absorbed, molecule vibrations in the ground electronic state are excited. Electrons are elevated to greater energy levels by UV-visible light ($280\text{--}700\ \text{nm}$), which then encourages their decay by various pathways like fluorescence and phosphorescence emission or non-radiative relaxation [81]. The lit molecules scatter light

when the wavelength of the incoming light does not match the energy of an electronic transition. The vast majority of the scattered photons are elastically scattered and have energies equivalent to the input light's energy. Rayleigh scattering is the name of this scattering technique. One out of every 10^6 to 10^8 photons are scattered inelastically [36, 82] with optical frequencies that are different from the incident light. Molecular Raman scattering describes the inelastic light scattering brought on by molecular vibrations [36].

In Raman scattering, the incident light interacts in two separate ways with the quantized energy levels of the scattering molecules. Raman scattering can cause the incident photons to either lose or gain energy. Stokes Raman scattering occurs when the scattered light has less energy than the incident light, whereas anti-Stokes Raman scattering occurs when the scattered light has more energy [83]. However, compared to Stokes Raman peaks, anti-Stokes Raman peaks are less strong [36]. The photons change from a lower energy level to a higher one during Stokes Raman scattering. In contrast, energy moves from the system to the incident light in anti-Stokes Raman as the system transitions from a higher energy level to a lower one.

According to the Boltzmann distribution, excited vibrational energy levels are less populated than the ground state. As a result, anti-Stokes are less intense since the scattering comes from a condition with a lower population density. In Figure 3.3, the three types of Raman scattering are shown. The absorption and scattering processes for Stokes and anti-Stokes scattering take place to and from an intermediate state that is a time-dependent superposition of molecular electronic states and is commonly referred to as a virtual state. The energies of the virtual states do not coincide with the energies of the current electronic levels in the scattering system.

Enhancing Raman scattering in near-field techniques such as surface and tip-enhanced Raman spectroscopy and optical forces in PiFM constitutes a research field that belongs to a more general theme of plasmonics. To better understand enhanced near-field discussions in this thesis, plasmon resonances in metal surfaces are introduced in the following sections.

3.1.6. Plasmonics

The interaction of electromagnetic radiation with metallic nanostructures excites the oscillation of the free conduction electrons of the metal out of phase relative to the driving electric field [6]. The oscillation causes a displacement of the free electrons concerning the positively charged lattice in metal, and therefore, at specific optical frequencies, the free electrons can sustain surface and volume charge density oscillations known as plasmons. The physical process involved in plasmon resonance includes the free movement of the metal conduction electrons within the bulk of the metal.

Volume plasmons

The volume plasmon describes the oscillation of free charge carriers in the solid for extended volumes and can be explained with the help of the following equation.

$$E_{vp} = \sqrt{\frac{\hbar^2 e^2 n}{m_e \epsilon_0}} = \hbar \omega_p V \quad (3.52)$$

In this equation, the energy of a volume plasmon is calculated, which depends on natural constants like the reduced Planck's constant (\hbar), the elementary charge (e), the dielectric constant in vacuum (ϵ_0) and the mass of the electron (m_e). The other physical quantities like the density of the valence electrons (n), the plasma frequency (ω_p) and the volume (V) represent material properties. From the equation it can be shown that the energy of the volume plasmon polariton is only influenced by the plasma frequency and the volume of the metallic object.

Surface plasmons

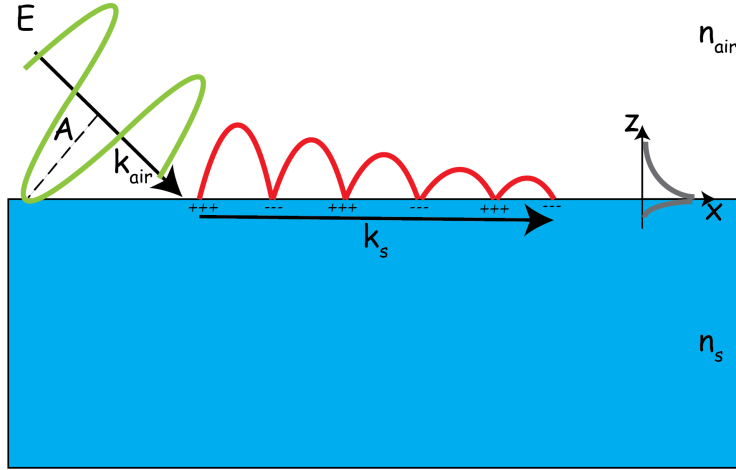


Figure 3.4: Schematic representation of a surface plasmon polariton (red wave), which is formed by constructive coupling of an external field (green wave). This surface plasmon polariton has an evanescent field along the propagation, which is shown by the grey lines.

The surface plasmon polariton, on the other hand, requires a boundary surface (e.g., metal-air) and a certain angle of incidence of the electromagnetic field, TM polarized to the surface, to be generated. To calculate the field

components above the surface ($z > 0$), the following equations should be considered [84]:

$$E_x(z) = -iA \frac{k_s}{\omega \epsilon_0 \epsilon_s} \exp(i\beta x + k_s z) \quad (3.53)$$

$$E_z(z) = -A \frac{\beta}{\omega \epsilon_0 \epsilon_s} \exp(i\beta x + k_s z) \quad (3.54)$$

Equation 3.53 show that x component of the electric field depends largely on the wave vector of the substrate (k_s). Thus, for the excitation of surface plasmons, a large fraction of wave vectors parallel to the boundary surface is needed. This can be achieved by a prism in the Otto [85] or Kretschmann [86] configuration. Considering equation 3.54, the z component of the field is largely influenced by the dispersion relation between two mediums:

$$\beta = k_0 \sqrt{\frac{\epsilon_s \epsilon_{air}}{\epsilon_s + \epsilon_{air}}} \quad (3.55)$$

where β describes the propagation constant. For the field components in the substrate ($z < 0$) the field behaves analogously.

$$E_x(z) = iA \frac{k_{air}}{\omega \epsilon_0 \epsilon_{air}} \exp(i\beta x - k_{air} z) \quad (3.56)$$

$$E_z(z) = -A \frac{\beta}{\omega \epsilon_0 \epsilon_{air}} \exp(i\beta x - k_{air} z) \quad (3.57)$$

In addition, for both cases ($z < 0$ and $z > 0$), the x component of the electric field is an imaginary value. As a result, there will be an evanescent surface plasmon field component perpendicular to the surface which gets enhanced near the interface and decays rapidly with distance away from it into the two mediums [87]. For surface plasmons to be detectable at the interface between a metal and a dielectric, the complex dielectric constant of the metal has to have a negative real and a positive imaginary part, which is the case for noble metals [88, 89].

Localized surface plasmons

When a surface plasmon is confined to a nanostructure with sizes comparable to the wavelength of the light, they cannot propagate anymore and remain localized. Accordingly, they are called localized surface plasmon resonance (LSPR) [90]. Incident light will stimulate the free electrons of the metal nanostructure to oscillate collectively with respect to the incident electric field upon which they experience a change in their momentum. The collective oscillations create charge accumulation at the surface. In addition, when these

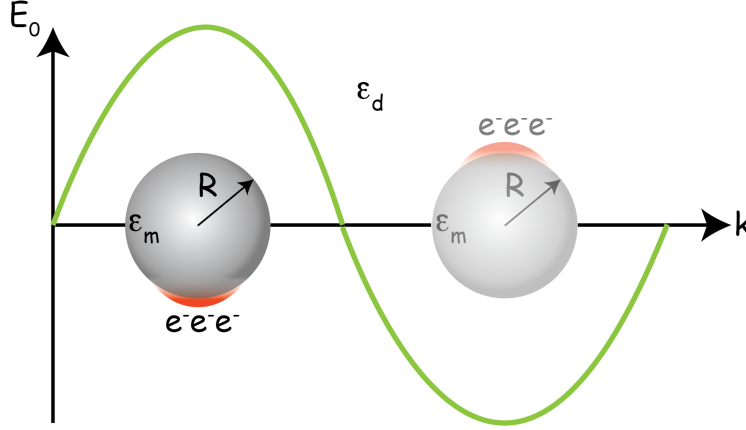


Figure 3.5: Schematic representation of a localized surface plasmon. This leads to an evanescent field upon oscillation of an external field due to the localization of electrons at the particle-medium interface (red area).

oscillations couple between neighboring nanostructures, the electric field gets locally more intensified inside the interparticle gaps. Near sharp features of a metallic nanostructure and LSPR condition, the electric field is enormously enhanced, yielding hot spots which decay rapidly with distance. Even if no plasmon resonance is triggered, the structure can still exhibit non-resonant field enhancement due to “field line crowding” at the apex of sharp metal tips. This phenomenon is also known as the lightning-rod effect in electrostatics [6, 91–94]. Similar to propagating surface plasmon, the LSPR depends on the chemical nature of the metal, the dielectric constant of the surrounding environment, along with the geometric parameters of the particles or ensemble of particles such as size and shape or interparticle distance [84, 89]. Mie’s analytical solution to Maxwell’s equations in the scattering and absorption of light by spherical particles is usually utilized for the characterization of LSPR [95]. According to the Mie theory, if the particles are very small ($R \ll \lambda$ with $2R$ being the diameter of the nanosphere) total extinction (σ_{ext}), absorption (σ_{abs}), and scattering (σ_{sca}), cross-section of a nanosphere can be defined as [84, 96]:

$$\sigma_{ext} = \frac{18\pi\epsilon_d^{\frac{3}{2}}V}{\lambda^4} \frac{Im(\epsilon_m)}{[Re(\epsilon_m)\chi\epsilon_d]^2 + [Im(\epsilon_m)]^2} \quad (3.58)$$

$$\sigma_{abs} = \frac{32\pi^4\epsilon_d^2V^2}{\lambda^4} \frac{[Re(\epsilon_m) - \epsilon_d]^2 + [Im(\epsilon_m)]^2}{[Re(\epsilon_m)\chi\epsilon_d]^2 + [Im(\epsilon_m)]^2} \quad (3.59)$$

$$\sigma_{ext} = \sigma_{abs} + \sigma_{sca} \quad (3.60)$$

The equations above confirm that the optical properties of metal nanoparticles are a function of the dielectric constants of the metal and the dielectric environment, as well as the geometrical parameters such as the shape factor (χ)

and volume (V) of the nanoparticles. These equations are typically used to estimate systems' optical response and the LSPR. In addition, LSPR can be accumulatively boosted when the interparticle distance between the nanoparticles is small enough to allow the coupling of the neighboring hot spots [84]. In summary, to increase field enhancement and improve the resolution and sensitivity of near-field optical measurements, the understanding of localized surface plasmon is essential for the fabrication of active plasmonic probes. This principle can be employed for efficient near-field probes.

Next, a method for modeling and investigating the tips' properties is introduced.

3.1.7. Calculation of electromagnetic phenomena in near-field optics

Numerical computational methods have grown crucially in applied electromagnetics over the last five decades. Winslow proposed the Finite Element Method (FEM) in 1963 [97], and Yee presented the Finite Difference Time Domain (FDTD) in 1966 [98]. The Approach of Moments (MoM) is a standardized integral equation approach that has its conceptual origins in Harrington's work from 1968 [99]. C. W. Trowbridge *et al.*, [100] included a full historical background as well as numerous different techniques, such as the Finite Integration Method (FIM) and the Fast Multipole Method (FMM). With user-friendly graphical interfaces and comprehensive postprocessing templates, the aforementioned techniques have been numerically implemented to form commercial software packages capable of fully characterizing three-dimensional (3-D) electromagnetics problems. These commercial softwares such as COMSOL [101], CST MICROWAVE STUDIO [102], Lumerical [103] are widely utilized in research organizations and industries throughout the world. M. Kupresak *et al.*, [104] demonstrated a comparative study of the most commonly used electromagnetics field solvers in nano-plasmonics: COMSOL, CST, and Lumerical.

For all the modeling in this work, COMSOL software which utilizes FEM to solve the electromagnetics problems is used. The finite element method (FEM) is a widely used technique for solving differential equations in engineering and mathematics numerically. Structural analysis, heat transfer, fluid flow, mass transport, and electromagnetic problems are typical areas to benefit from FEM. To solve partial differential equations with two or three variables in two or three dimensions, FEM is a powerful method. The FEM breaks down an extensive and complicated system into smaller, more straightforward units called finite elements to solve a problem. A particular space discretization achieves this in the space dimensions, implemented by constructing a mesh

within the object. With a finite number of points, this object is then defined as a numerical domain for the solution. All the details about using COMSOL for modeling near-field optics are vastly presented in [\[105\]](#).

3.1.8. Optical setup configuration

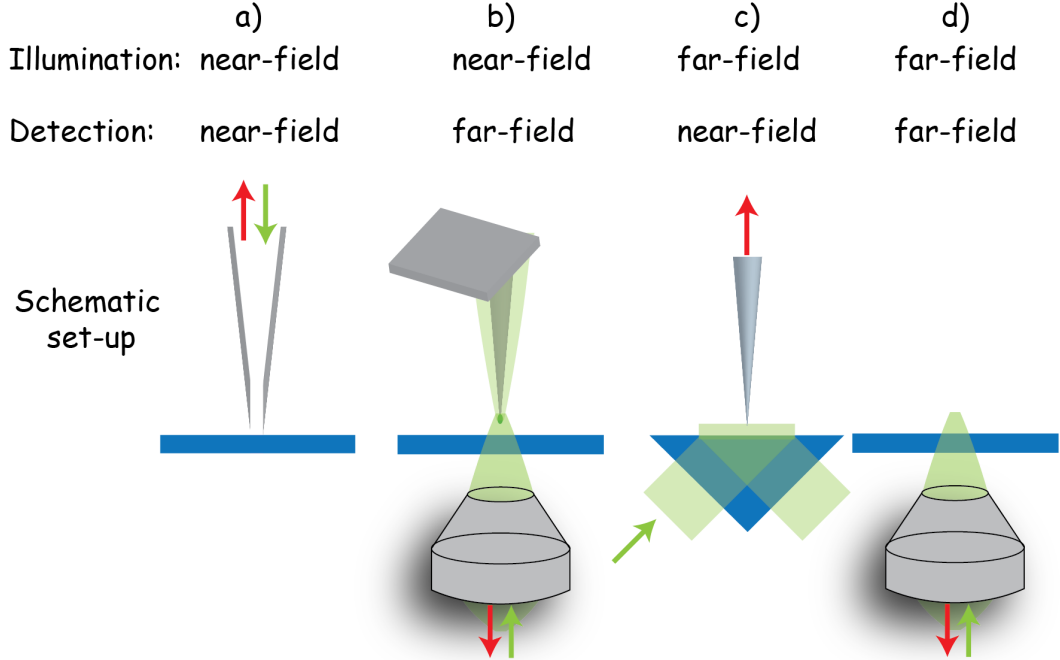


Figure 3.6: Summary of possible configurations in high-resolution optical microscopy categorized by the illumination and detection principle. Figure is adapted from [6].

The theory and fundamental of modeling the near-field optical measurements have been presented and discussed in previous sections. Here a brief overview of the illumination configurations is explained. The external excitation field is an important factor in near-field optics. For example, it can be decisive whether the optical coupling into a plasmonic system is constructive and thus generates an amplification. Due to this fact, a variety of possible setups in high-resolution optical microscopy have been developed in recent years (see Figure 3.6) [6]. In this work, only the bottom illumination/collection scheme (see Figure 3.6 b) will be considered. In this case, even with a low numerical aperture, optical excitation is done through the substrate [106]. However, this approach is rather uncommon since the collection efficiency is low. For instance for TERS it has been reported below 60% [107]. For this reason, setups with high numerical aperture [108] are often used. Hereby, it is possible to generate polarizations perpendicular to the surface on the substrate with a high collectivity, which has a constructive effect on the near-field signal to be detected. Since these setups are partly easier to design and have a great collection efficiency, they are also mainly used in our working group. Thus,

primarily this configuration is investigated in this work.

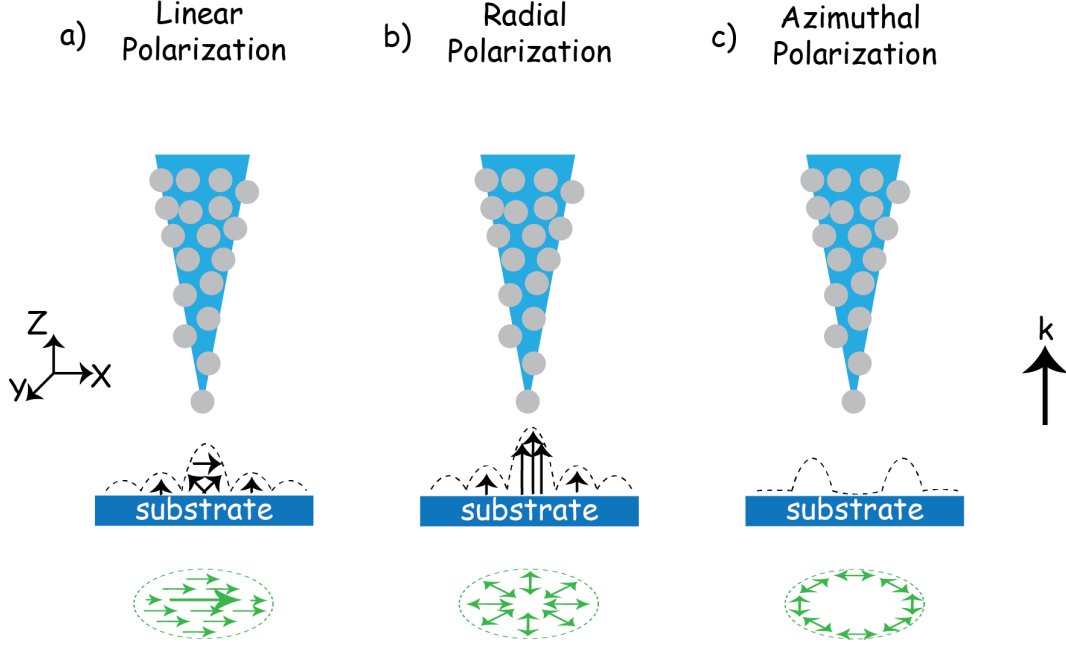


Figure 3.7: Schematic representation of a probe on the substrate surface under illumination of a) linearly polarized beam (LPB), b) radially polarized beam (RPB), and c) azimuthally polarized beam (APB) with high NA .

The enhancement of the electric field in near-field optics depends critically on various parameters such as the polarization of the excitation beam, the metallic nature and the geometry of the metallic tip, as well as the sample substrate [109–112]. In near-field optics, a polarization component of the incident light along the tip axis induces a strong surface charge density at the sharp apex of the metallic tip, which is a prerequisite for local enhancement of the electric field [109]. As it can be seen from Figure 3.7 laser with different polarizations (green arrows in Figure 3.7) can create different electric field components on the substrate surface. Figure 3.7 a) shows that in case of the LPB center of the beam is not the best choice for doing near-field optics experiments in transmission configuration because the axial (z) component of the electric field on the substrate is not very strong there (more details in 3.1.9). However, by using RPB, one can overcome this flaw since there is a solid axial component at the center of the beam (Figure 3.7 b). Laser beams with radial polarization provide unique focusing properties, including a strong electric field component along the tip axis generated at the focal point [113,114] (more details in 3.1.10). On the other hand, the APB is not the appropriate choice for this configuration because there is no axial component on the substrate surface (there is no black arrow on the substrate in Figure 3.7 c) (more details

in 3.1.11). Next, the outcomes from section 3.1.4 are designed and integrated into COMSOL to conduct the FEM calculation and model LPB, RPB, and APB.

3.1.9. Linear polarization

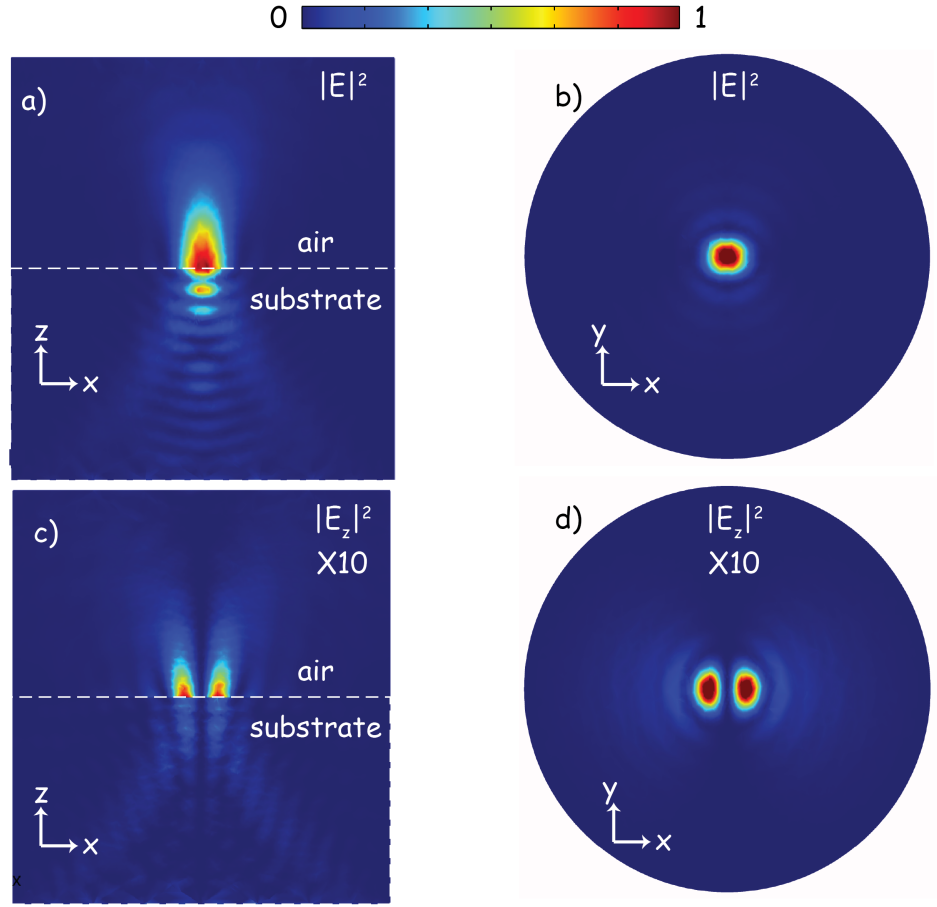


Figure 3.8: Intensity profile of a tightly focused x polarized light modeled using FEM in COMSOL from (a) side and (b) top view. (c) Corresponding out-of-plane components of the field from side and (d) top view.

In a linearly polarized electromagnetic wave, the electric field vectors are oriented along a single direction inside a plane perpendicular to the propagation direction of the wave. The top and side view of the total intensity profile $|E|^2$ of a tightly focused LPB along with their corresponding out-of-plane components $|E_z|^2$ are shown in Figure 3.8a, Figure 3.8b and Figure 3.8c, Figure 3.8d respectively. Here the Gaussian beam has been focused by passing an objective lens with 1.3 numerical aperture. Refractive index of the substrate

is $n_{sub} = 1.5$.

The top view of a focused Gaussian beam consists of several concentric rings in xy plane with a maximum intensity in the middle (Figure 3.8 b). From the side view, the beam would be relatively elongated in the direction of propagation along z (Figure 3.8 a). The z component of the electric field in a focused Gaussian beam has two lobes in the direction of polarization with zero intensity in the middle (Figure 3.8 c and Figure 3.8 d). This minimum intensity results in the absence of significant excitation of plasmon resonances at the tip apex if the tip is located in the center of the focal region. Hence, tip-enhanced Raman or photo-induced force should be observed more significantly in case the tip is located inside one of the two lobes of the LPB excitation.

3.1.10. Radial polarization

By using equations 3.48 and 3.49 propagation of the radially polarized beam can be simulated. A radially polarized beam (RPB) has polarization vectors oriented radially in the transverse plane with respect to the propagation direction as it is shown in Figure 3.7 a). The transverse and longitudinal intensity components of the described beam are shown in Figure 3.9 c) and Figure 3.9 d). The transverse component of a RPB consists of several concentric rings with variable intensities and a minimum intensity at the middle. The longitudinal component of this beam is another set of concentric rings with overall intensities higher than the transverse component and with a maximum intensity at the center. As can be seen from Figure 3.9, RPB is of great interest for near-field optics experiments using bottom illumination/collection optical setups since maximum intensity with a strong longitudinal field component emerges at the center of the beam. In this case, a robust field enhancement at the apex of the sharp metallic tip can be expected in the center of the beam.

3.1.11. Azimuthal polarization

In azimuthally polarized beam (APB) electric field components are in tangential format. Utilizing the equations 3.50 and 3.51 can help us simulate propagation of laser beam with azimuthal polarization. One can see that the transverse component of an azimuthally polarized beam plays a crucial role. So the total electric field of the beam (Figure 3.10 b) is proportional to the transverse component (Figure 3.10 c) of this beam. On the other hand, there is no longitudinal component (Figure 3.10 d), and that is why we can see no electric field component perpendicular to the substrate surface (Figure 3.10 a). Even though this beam seem to have no actual application for near-field enhancement in this configuration, it has its benefits for magnetic field mea-

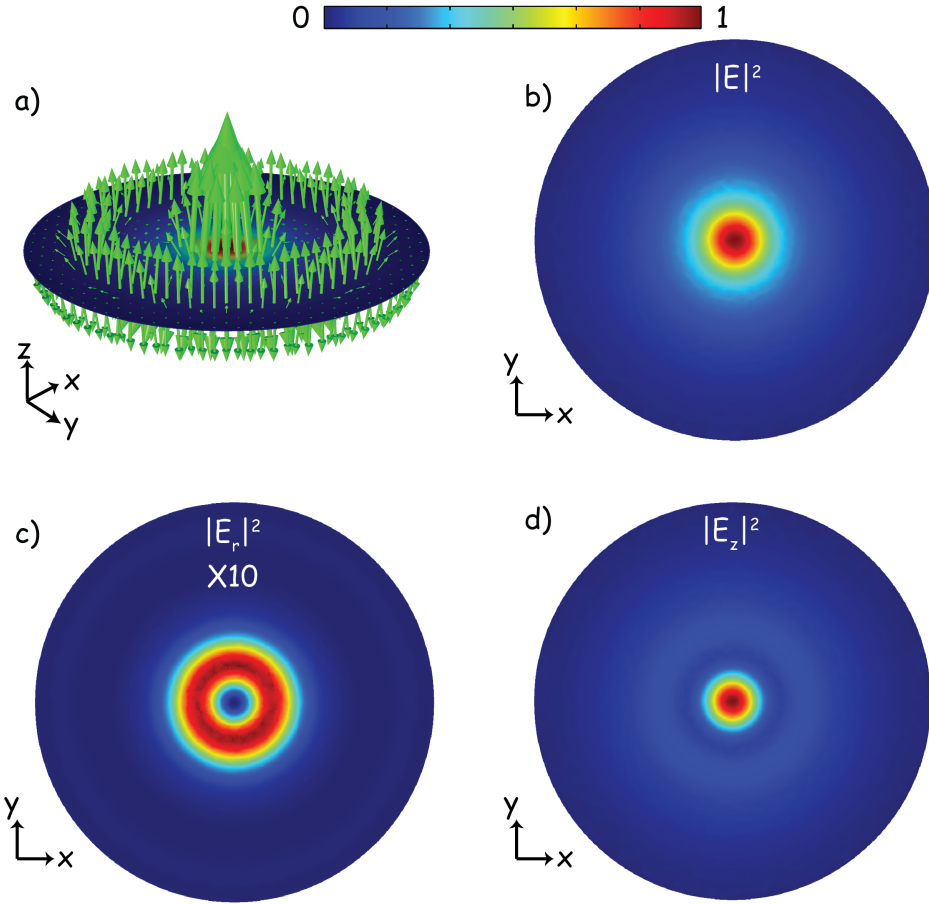


Figure 3.9: Intensity profile of a tightly focused radially polarized beam modeled using FEM in COMSOL with 3D presentation of electric field components on the substrate (green arrows) in (a). (b) total intensity distribution (c) intensity of transverse component (E_r) and (d) intensity of longitudinal component (E_z) all shown from top view.

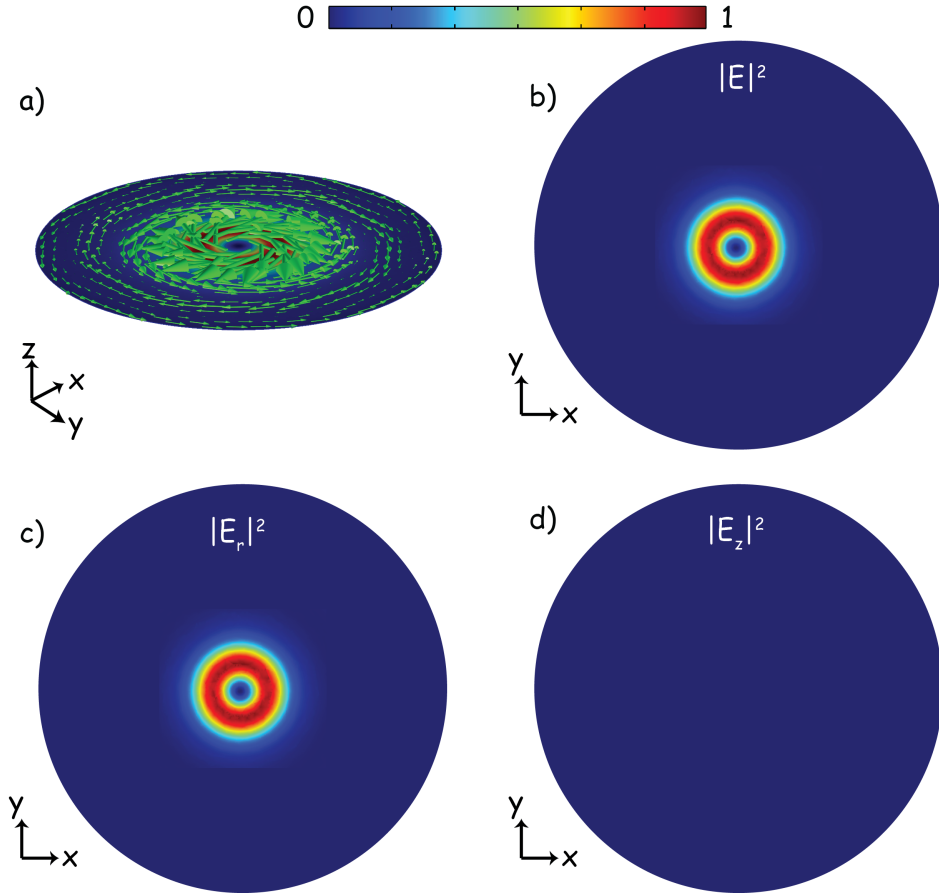


Figure 3.10: Intensity profile of a tightly focused azimuthally polarized beam modeled using FEM in COMSOL with 3D presentation of electric field components on the substrate (green arrows) in (a). (b) total intensity distribution (c) intensity of transverse component (E_r) and (d) intensity of longitudinal component (E_z) all shown from top view.

surements as it carries a strong magnetic field at its center [[115](#)].

3.2. Results

As mentioned in the introduction and previous sections, the metallic tip determines the performance of the probe-based near-field optics experiments. Although the importance of these tips has been highlighted continuously, few articles have investigated tip performance in their realistic shape. In our case, for a blue-green spectral region, tips are used for AFM-based TERS and PiFM, in which tips are usually fabricated by thermal evaporation of silver on a commercially available silicon AFM cantilever tip. In this method, rough silver grains form in random shape, size, and interparticle distances on the AFM cantilever. Several groups have used these tips, but few investigated the performance of rough tips over the smooth ones [116, 117]. Tagushi *et al.* considered the effect of multiple metal grains on the enhancement of TERS signals. Although they showed that multiple metal grains near the tip apex provide good enhancement [118], and a single metallic NP attached to the tip apex are also reported [119, 120]. This controversy and the fact that most tip modelings consider smooth tips with symmetric and well-shaped plasmonic structures on it, or even just a simple sphere [121–123], imply that comprehensive modeling considering realistic and rough tips is needed. Rough tips produced by metal evaporation and subsequent annealing show reliable enhancement and are comparatively easy to produce. Such realistic tips require a more elaborate model to estimate the far-field and near-field optical response. Electromagnetic simulations of the plasmonic response of probes are generally applied to understand better the tip response regarding resonance and lateral resolution and, consequently, the optimization of experiments.

This subchapter presents a comprehensive investigation of plasmonic probes. The absorption spectrum, near-field response, and scattering pattern of the plasmonic nanoparticles (NPs) are discussed chronologically. In the subsequent step, a theoretical study of the interaction of light with a 3-dimensional plasmonic near-field probe is presented. The electromagnetic calculations employing a FEM are used to model far-field and near-field optical responses based on parametrized scanning electron microscopy (SEM) images of plasmonic tips. It is a previously used yet powerful method to simulate a vast range of complex irregular 3D structures. It can also be easily and generally applied to plasmonic probes of different geometry, and roughness [124]. At the end of this subchapter, the mechanical properties of the AFM probes are examined and discussed.

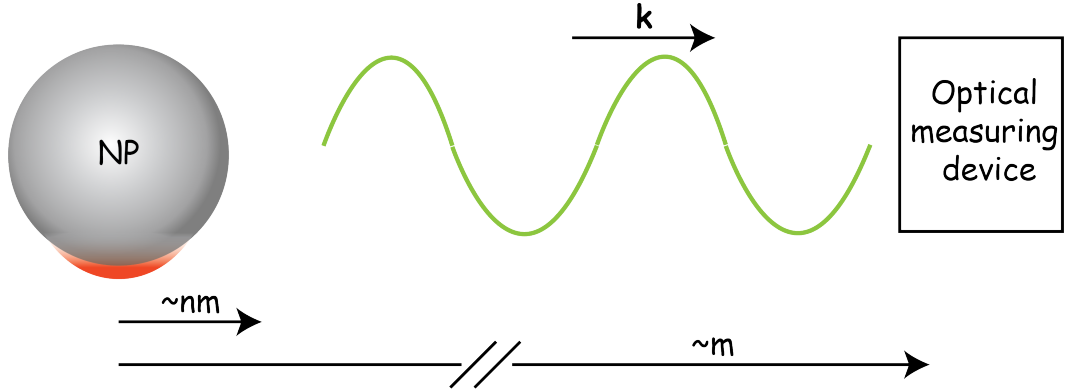


Figure 3.11: Illustration of the spectroscopic problem; surface-enhanced spectroscopy such as SERS, TERS and PiFM occurs within a few nanometers from the nanoparticle surface (the near-field), while common detection techniques are done many wavelengths away from the particle (far-field). In general, the resonant wavelength is not the same in the near- and far-field.

3.2.1. Absorption spectrum of plasmonic nanoparticles

As vastly discussed, a rapidly increasing number of applications utilize the unique optical effects of plasmonic NPs. However, when a new nanoplasmonic structure is proposed or when structures are to be compared, a simple question arises: how should the optical properties of the nanostructure(s) be characterized? The most common experimental techniques rely on far-field measures, where an optical signal is measured many wavelengths away from the nanostructure and hence takes on the form of a propagating wave. The most common far-field measurements are extinction (scattering plus absorption) spectrum. In contrast, near-field techniques measure the electromagnetic field within one wavelength (and often within nanometers) of the nanostructure surface. While the far-field measures are easier to obtain experimentally, the near-field is responsible for surface-enhanced near-field optics processes such as surface-enhanced Raman spectroscopy (SERS), TERS, and PiFM. This spectroscopic problem is framed in Figure 3.11. Hence, the sensing capabilities of a structure are most intimately tied with its local field responses.

Figure 3.12 (a) shows a typical active TERS active tip produced by silver evaporation on a commercial AFM tip (*Tap190Al-G*, BudgetSensors, Sofia, Bulgaria). The NPs vary slightly in size and shape. They can be described as hemisphere-like particles, and in addition, they show edges and atomic protrusions (as shown by TEM experiments) [125]. The effect of size distribution and shape on their plasmon response has been widely investigated [89]. To model more realistic plasmonic tips, it is pivotal to determine the actual size of the silver grains on the TERS tips for further analysis. To determine the

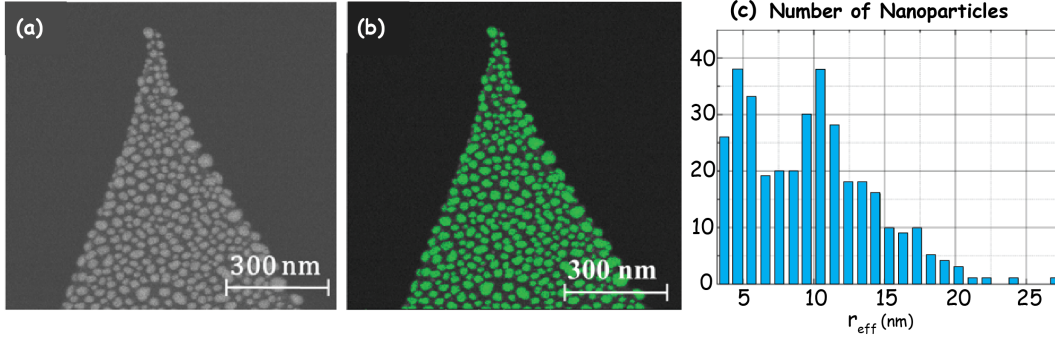


Figure 3.12: Determination of the relative size distribution of particles of a TERS tip using a threshold in the SEM image (a). The area of the particles with a threshold value of 30% (b). The size distribution of nanoparticles, based on their effective radius (r_{eff}) (c).

size distribution, Figure 3.12 (a) was loaded into the Gwyddion program [126], and the particles were marked above a threshold of 30% (green areas in Figure 3.12 (b)). With the help of this masking, it is possible to numerically determine the effective radius (r_{eff}) from the respective particle area. Figure 3.12 (c) shows that particles with a radius of 5 and 10 nm contribute mainly at the TERS tip. Since larger particles tend to form at the edges and the frontmost parts of the tip and are more effective in the TERS measurements, the particle radius of 10 nm is used for most of the calculations.

As revealed, the tips used here resemble hemispherical NPs with slightly varying shapes, sizes, and gaps between them. Investigating the tip's respective plasmonic modes is challenging as individual variations can play a significant role. As a first step, the whole complex nanoantenna, as sets of interacting dimers of silver NPs, will be considered as a model for the simplest and smallest plasmonic clusters. Although the optics of hemispherical plasmonic NPs have been investigated previously [127, 128], it is helpful to closely look at the plasmonic modes in NP systems.

In this part, individual modes relevant for the far-field response will be examined more closely. Three different cases for dimer of (hemispherical) silver NPs in the air were modeled and the respective absorption spectrum was calculated (Figure 3.13). In the first case, the distance is sufficiently large, and the particles interact weakly (see Figure 3.13 (a) top). Here NPs show two plasmonic modes (360 nm and 400 nm). The surface charge density plot reveals that, mode 360 nm peak is a quadrupole plasmon (QP) and mode 400 nm peak is a dipole plasmon (DP) (see Figure 3.13 (b)). The quadrupole mode arises from the anisotropy of the nanoparticles (hemisphere). In the second case, the interparticle distance is set to 2 nm (see Figure 3.13 (a) center). In this formation, three modes are present. Mode QP and DP are similar to the

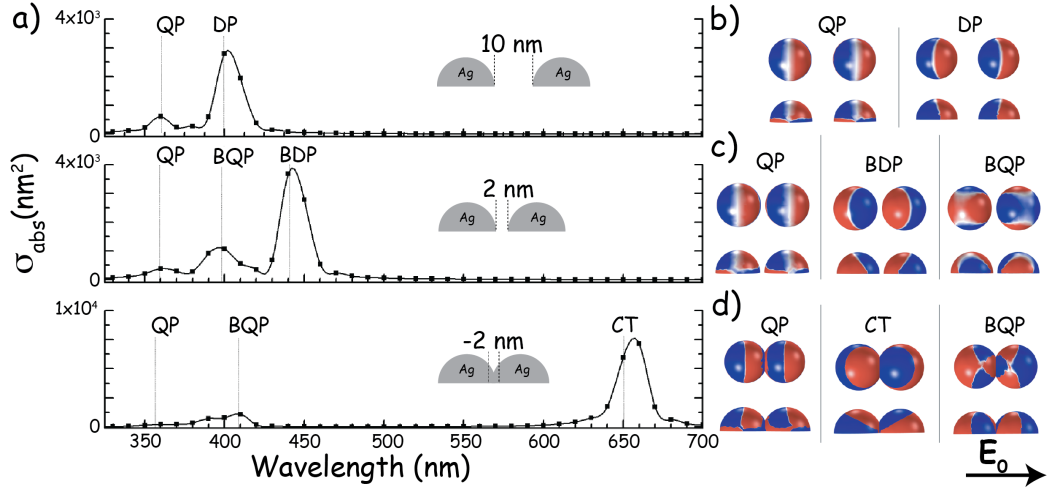


Figure 3.13: Calculated absorption spectra of hemispherical silver NP dimers ($R=10$ nm) in air for a gap distance of 10 nm (top), 2 nm (middle) and -2 nm (bottom). b), c) and d) show the surface charge density of the hemisphere NPs depending on the respective modes for top and side view. Note the charge density change of the “quadrupolar modes” close to the surface. Figure is adapted from [105].

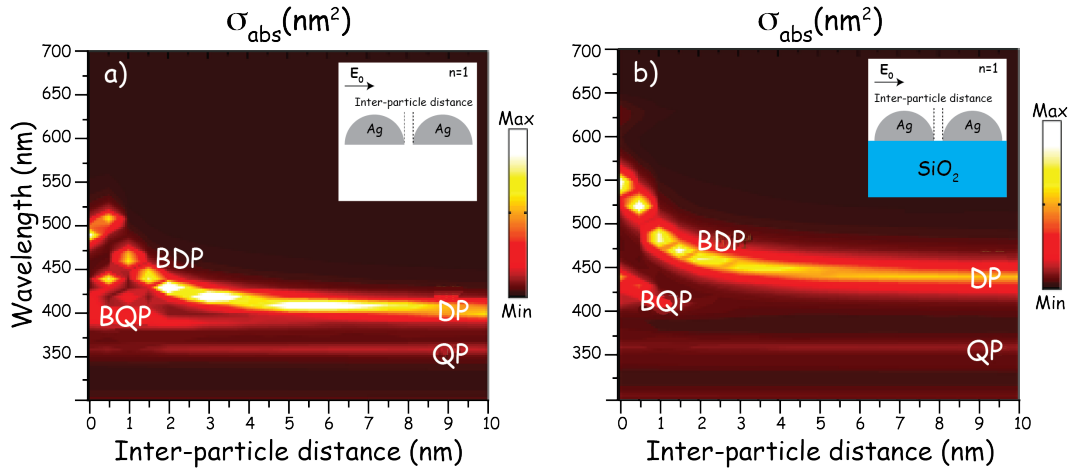


Figure 3.14: Far-field spectrum (σ_{abs}) as a function of inter-particle distance for a hemisphere dimer in air (a) and on a SiO_2 substrate (b) shows the dependency of the dipole plasmon (DP), binding dipole plasmon (BDP), quadrupole plasmon (QP), and binding quadrupole plasmon (BQP) modes with respect to the inter-particle distance. Figure is adapted from [105].

previous case. Still, since DP is influenced (red-shifted) by the adjacent NP, it can be considered as the binding dipole plasmon (BDP). The surface charge density shows that the newly appearing resonance 440 nm , which is a binding quadrupole plasmon (BQP) mode. In the third case, the NPs are touching each other and due to quantum effects such as tunneling effects, the classical simulation here is only valid conditionally [129, 130]. A new mode at 660 nm is formed (see Figure 3.13 (d)) in which a charge-transfer (CT) plasmon occurs [131].

Next, we did more general calculations and considered the effect of substrate on the system. Figure 3.14 shows the particle distance dependence of the far-field (σ_{abs}) spectrum for the two systems. The model is based on two hemispherical silver NPs with a 10 nm radius, either entirely in the air, Figure 3.14, (a) or on a quartz substrate in air, Figure 3.14, (b). The polarization direction was parallel to the main dimer axis. The calculations (see Figure 3.14, a) show that the DP (400 nm) for distances smaller than 5 nm shifts toward larger wavelengths, which is in agreement with previous work where this shift and appearance of new modes were attributed to the hybridization of two single particle DP modes, and a BDP mode starts to form [132]. It should be noted that due to anisotropy in the NPs, a QP mode and a BQP mode also appeared [133–135]. At this time, these arguments are qualitative considerations providing physically meaningful results for a distance $> 2\text{ nm}$ (local regime) [136]. For distances below 2 nm , the system enters a non-local or quantum regime ($0.3\text{--}0.4\text{ nm} < \text{inter-particle distances} < 2\text{ nm}$: a classical non-local regime, and inter-particle distances $< 0.3\text{--}0.4\text{ nm}$: the quantum regime), where purely classical calculations have to be corrected. Since, the plasmon resonance of NPs depends on the refractive index of the surrounding medium, the response of a hemispherical NP dimer on quartz is calculated (see Figure 3.14, (b)). As expected, the initial “free” dipole plasmon (DP) mode shifts from 400 to 450 nm . The coupling distance does not significantly change so it can be generally assumed that, for this particle shape, coupling occurs at distances of half the particle radius. It should be mentioned that the QP mode hardly generate measurable signals in TERS. However, it can be measured in transmission and reflection measurements for other plasmonic applications of silver films, which several groups confirmed [136, 137]. The discussed simple cases for NP dimer provides general information on the plasmonic modes involved in a TERS probe. Still, a real tip certainly looks different and more interactions should be considered to better understand their performance better.

3.2.2. Near-field response of plasmonic nanoparticles

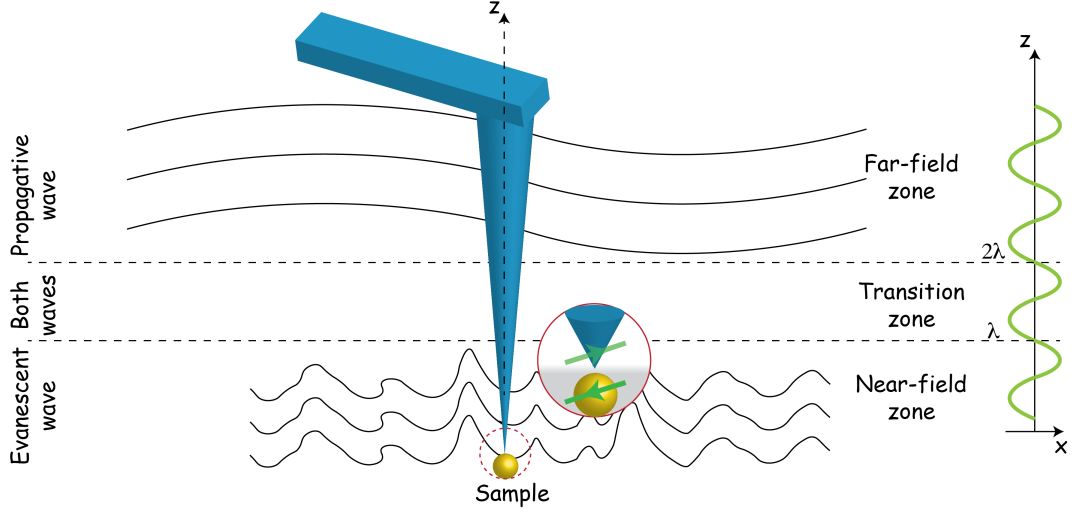


Figure 3.15: Schematic illustration of different waves contributing in spectroscopy. Figure is adapted from [138].

In the previous section, the optical response of a plasmonic system in the far-field, where the diffraction limit (explained in 1) is a substantial limiting factor in accessing sub-wavelength information from the examined sample, is studied. As vastly explained in the introduction 1, SNOM is one way to conquer the diffraction limit in optical microscopy, which operates in the optical near field zone, where the evanescent waves are predominant. Evanescent fields are of significant importance for the interpretation of optical fields that are confined to subwavelength dimensions. They possess an imaginary wave vector component so that the wave does not propagate but rather decays exponentially. Evanescent waves never appear in a homogeneous medium but are inevitably connected to the interaction of light with inhomogeneities [139]. The simplest case of inhomogeneity is a plane interface. Access to the evanescent waves allows achieving high optical resolution [6]. In the very general scheme of conventional microscopy and spectroscopy, the sample is illuminated by incident light (E_{in}), and a detector then collects the scattered or emitted light. Upon illumination, the incident field induces a polarization current in the sample, giving rise to a radiated field (E_{out}) [140]. In near-field optics, however, two entities are considered. One is referred to as the probe and the other part as the sample, as illustrated in Figure 3.15. For a SNOM measurement, the probe is designed to have unique properties of metal nanostructures at optical frequencies to exhibit a localized surface plasmon resonance. When the light is incident on the probe, the incoming electric field periodically displaces the probe's electron clouds. Near resonance frequency,

electron clouds oscillation gives rise to a greatly amplified electric field a few nanometers outside the probe, called the near-field region. The probe acts as a nanoantenna which converts non-propagating field components confined on the sample surface (evanescent waves) into propagating radiation [141]. This nanoscale antenna acts as a receiver for the input light and an emitter for the output light to be detected. E_{out} emitted by the combined system contains information about the sample properties. As a result, near-field measurements enable retrieving the small details of a sample through the localized light-sample interaction within a few nanometers above the surface.

Calculation of the local electromagnetic field near a Plasmonic Structure: Field Enhancement

Here, the calculation of the field enhancement of plasmonic structures considering the different input polarization is given. But before running the simulations, it is helpful to consider the local field intensity analytically and discuss the spatial resolution. In a case where the tip is considered as a sphere with radius R , $\alpha_t = 4\pi\epsilon_0 R^3 \frac{\epsilon_t - \epsilon_m}{\epsilon_t + 2\epsilon_m}$ represents the polarizability of the tip, where ϵ_0 is the vacuum's permittivity, ϵ_m is the polarizability of the medium and ϵ_t is the permittivity of the sphere. For an incident electric field, \mathbf{E}_0 the local electric field (\mathbf{E}_{loc} or \mathbf{E}_{ind}) at a distance \mathbf{r} near the sphere can be obtained from the polarized dipole moment ($\mathbf{d}_t = \alpha_t \mathbf{E}_0$) as follows [6]:

$$\mathbf{E}_{ind} = \mathbf{E}_0 + \frac{1}{4\pi\epsilon_0} \frac{3(\mathbf{d} \cdot \hat{\mathbf{r}})\hat{\mathbf{r}} - \mathbf{d}}{r^3} \quad (3.61)$$

For a test point right beneath the tip apex at z , the local field intensity or the field enhancement can be simplified as:

$$\frac{|\mathbf{E}_{ind}|}{|\mathbf{E}_0|} = 1 + 2\left(\frac{\epsilon_t - \epsilon_m}{\epsilon_t + \epsilon_m}\right)\left(\frac{R}{R + z}\right)^3 \quad (3.62)$$

Equation 3.62 from very simplified analytical theory shows that the field enhancement of a plasmonic structure depends on its shape (R), material (ϵ_t), and respective position in which the localized field is measured (z). The theoretical definition of the second advantage of near-field optics, spatial resolution, also depends on the field enhancement. In general, when the local field decreases to half of its maximum value or the full width at half maximum (FWHM), it theoretically defines the system's spatial resolution. For the simplified analysis above, this factor can be written as $W \approx 1.364(R + z)$ [142]. So it is clear the decrease in W leads to achieving better spatial resolution, which, for this simple case, can be accomplished when the plasmonic structure is sharper (smaller R) or very close to the sample (smaller z). In other words,

a very sharp tip (that could eventually imply even an atomic scale sharpness) is required to achieve high spatial resolution experimentally [125, 142]. Introducing a nano-cavity (or nano-gap) in the tip-substrate system leads to the gap-mode plasmons, which improves the local field enhancement and the corresponding field confinement in the metallic nanostructures. This hybrid system can be viewed as a dimer system composed of a metal sphere and its image on the metallic substrate [143].

Here, field enhancement of the gold and silver NPs is investigated. Gold and silver are the most potential candidates for SNOM in the visible range of frequency. In each FEM model, the NP is placed 1 nm above the substrate (glass to model conventional-mode and gold/silver for Gap-mode). After illumination of incident light (\mathbf{E}_0), the induced electric field (\mathbf{E}_{ind}) is then calculated at the specific position within the 1 nm gap between the nanostructure and the substrate. This calculated local field is then normalized to the incident field, so the field enhancement for all of our models is defined as $E_{enh} = \frac{|\mathbf{E}_{ind}|}{|\mathbf{E}_0|}$. A $1\text{ }\mu\text{m}$ extend metal film of 20 nm thickness was used as the substrate in the gap-mode model. Illumination with two different polarizations, linearly polarized and radially polarized beams (LPB and RPB, respectively), was set to propagate along the tip axis (transmission configuration). For LPB excitation, the tip is intentionally positioned off-center to optimize the z -coupling efficiency. The illumination wavelength was chosen depending on the tip material (532 nm for silver and 632 nm for gold NP).

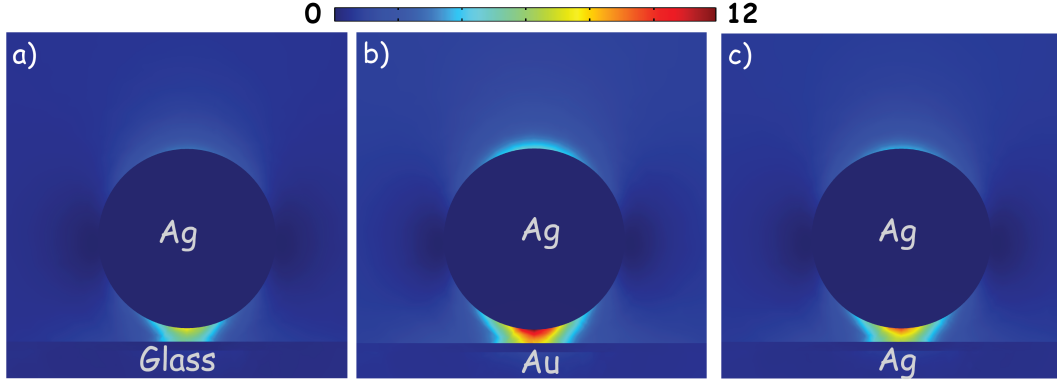


Figure 3.16: Electric field enhancement distribution around a 10 nm silver NP with (a) glass (b) gold and (c) silver substrate under linear polarized beam illumination at 532 nm .

Tip	Substrate	Polarization	$\lambda(\text{nm})$	$E_{enh} = \frac{ \mathbf{E}_{ind} }{ \mathbf{E}_0 }$
Ag	Glass	Linear	532	4
Ag	Ag	Linear	532	7
Ag	Au	Linear	532	10
Au	Glass	Linear	632	5
Au	Ag	Linear	632	8
Au	Au	Linear	632	10
Ag	Glass	Radial	532	27
Ag	Ag	Radial	532	80
Ag	Au	Radial	532	108
Au	Glass	Radial	632	41
Au	Ag	Radial	632	73
Au	Au	Radial	632	82

Table 3.1: Comparison of the electric field enhancement within the 1 nm gap between the apex of gold/silver tip and glass or thin gold/silver substrate.

The results of these simulations are presented in Figure 3.16. The tip, here single silver NP, illuminated with an LPB, is placed 1 nm above the glass (a), gold (b), and silver (c) substrate. Here the green laser (532 nm wavelength) is modeled. The results for a different combination of gold and silver tips and substrate in various incident illuminations are summarized in Table 3.1.

A closer look at these results reveals that the simulations predict a more prominent enhancement factor inside the gap generated between a silver tip and a gold substrate rather than between the silver tip and the silver substrate. This phenomenon might be related to the fact that silver, which has an

extinction coefficient of 3.5 at 532 nm wavelength, absorbs a more significant part of the incident light rather than gold having an extinction coefficient of 2.1 at the same wavelength. This absorption weakens the excitation beam that reaches the tip apex. The absorption of the light by the silver substrate can be relatively high, which breaks the observed trend for the confinement factor of the electric field. Silver has a larger absorption of 632 nm light with an extinction coefficient of 4.02 at this wavelength, and gold has an extinction coefficient of 3.02 at 632 nm wavelength, which decreases the amount of light that reaches the gold tip in gap-mode [96, 144].

It is also important to mention that, in all of our gap-mode configurations, the NP was placed in the middle of the metallic substrate. However, It has been shown, both in theory and the experiment, when the tip is placed on the top of the edges of the metallic substrate, even higher field enhancement and spatial resolution can be achieved [145].

3.2.3. Directionality of the scattering field in Plasmonic nanoparticles

Now that the near-field response of the plasmonic structure is discussed, it is helpful to know the radiation pattern of the near- toward far-field. The Straton-Chu formula implemented in the Comsol multiphysics is employed in this case. [101, 146–149]. This approach makes the modeling very convenient because it is a near- to far-field transformation that causes simulation volume to be scaled down pretty much into the near-field zone. The benefit of this method is to reduce computational resources and time. In this work, the effect of the glass substrate is not included in any of the radiation pattern simulations.

Figure 3.17 shows the far-field radiation pattern (E_{far}) of a system of free-standing silver NPs above a glass substrate under LPB in y-direction at 395 nm . Figure 3.17 a) displays the scheme of the models. All the NPs have a 10 nm radius with a 1 nm surface to surface distance. First, to examine our model, a single silver NP is considered. As it can be seen from Figure 3.17 b) (3D) and 2) (2D), single silver NP exhibits the well-known donut shape far-field radiation. It shows almost no radiation in the direction of incident polarization and/or induced dipole moment, which is in agreement with results in [6, 96]. Figure 3.17 c) and d) show that when silver NPs form a "chain-like" structure [150, 151] the radiation pattern from NPs is slightly shifted toward the "chain" axis (here z direction). This shift is strongly pronounced when the number of interacting NPs is increased to 10 (see Figure 3.17 f) and g)). Here it has been shown that FEM can be utilized to uncover the radiation pattern of the nanostructures. Moreover, FEM calculations show

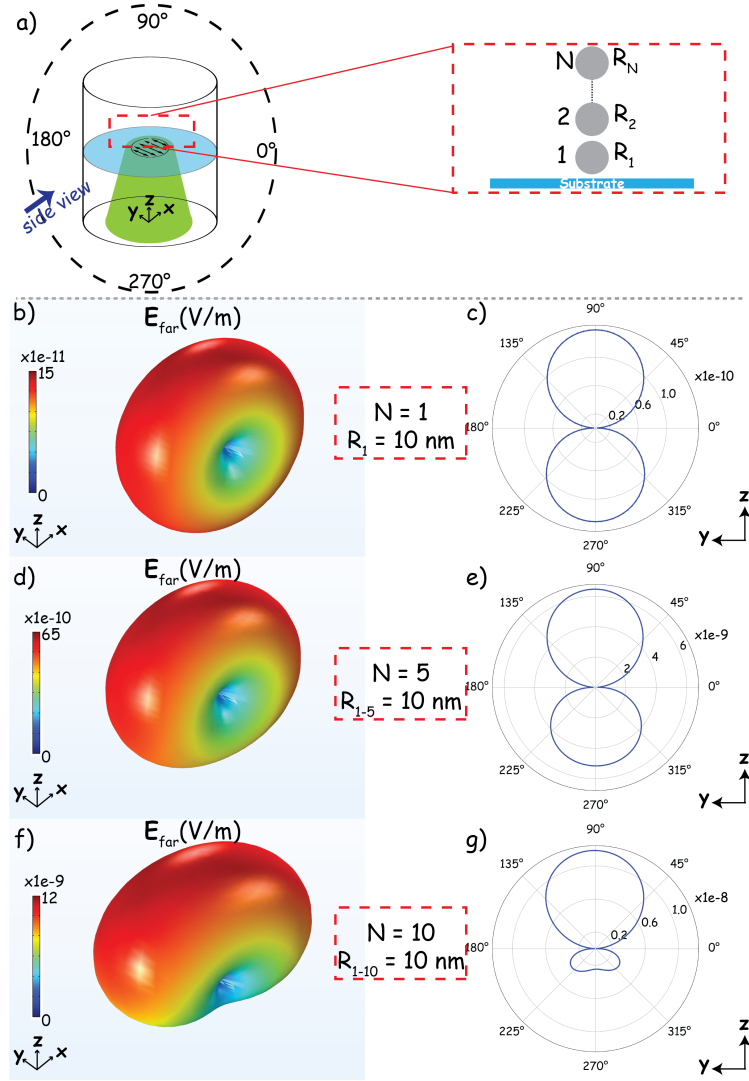


Figure 3.17: Far-field radiation pattern E_{far} of a chain of 10 nm radius free standing silver NPs above the glass substrate under linearly polarized light illumination at 395 nm . a) shows the scheme of the modeling. Three dimensional radiation pattern of single NP, 5 NPs, and 10 NPs are shown in b), d), and f), respectively. c), e), and g) displaying the two dimensional pattern of the respective chains.

that in bottom illumination/collection configurations, the formation of NPs can strongly affect the far-field radiation pattern of the nanostructure.

Next, all the introduced concepts will be used to model a plasmonic tip with its "realistic" shape and to investigate its optical responses.

3.2.4. Model Development and Optical Responses of a Realistic 3D tip

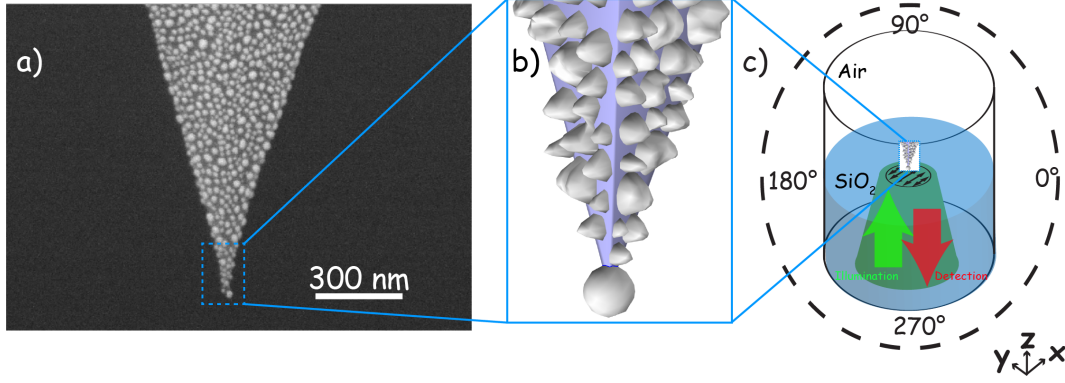


Figure 3.18: a) SEM image of a “TERS silver-evaporated-on- Si ” tip. b) parametrized 3D shape tip modeled in COMSOL Multiphysics for FEM calculations. c) Details of the model used in this work: 700 nm long tip in bottom illumination-collection configuration with LPB and RPB ($NA=1.25$) in the z -direction. The tip is positioned 1 nm above the SiO_2 substrate. The tip is specifically positioned off-center for the LPB excitation to optimize the z -coupling efficiency.

After introducing all the principles and investigating the optical properties of relatively small nanostructures, it is time to expand the models and simulate a realistic plasmonic tip. Figure 3.18 (a) shows an SEM image of one side of a TERS tip and the challenges of a detailed understanding of the plasmonic behavior of the plasmonic far- and near-fields. As the next step towards accurate optical response modeling of a realistic plasmonic probe, a FEM-based methodology was used. Based on previous work, where this method was used to investigate plasmonic responses of SERS substrates [124], we developed it for plasmonic modeling of TERS and extended it to three dimensions. Similar to the plane SERS substrates, the silver NP surface of the tip, obtained from SEM images, was parametrized and then 3D meshed using COMSOL Multiphysics. This 3D meshed film of silver NPs was then placed virtually on the pyramidal edge of a commercial Si -based AFM tip with a half pyramidal angle of (for *Tap190Al-G*, BudgetSensors, Sofia, Bulgaria), Figure 3.18 (b). Due to memory and meshing restrictions, the model considered the first 700 nm of the tip shaft. Still, the effect of atomic-scale roughness of single silver NP as an essential feature to interpret the exceptional high resolution and enhancement factor in TERS experiment [125] cannot be considered in the model at this time. The present study focuses on investigating the influence of arbitrary-shaped neighboring NPs. Consequently, the front-most NP is regarded as a

smooth spherical NP. Figure 3.18 (c) presents the model based on a tip-sample configuration for bottom illumination with LPB and RPB ($NA=1.25$) in the z -direction. The 700 nm long realistic tip is positioned 1 nm above the SiO_2 substrate.

Absorption spectrum of a plasmonic probe

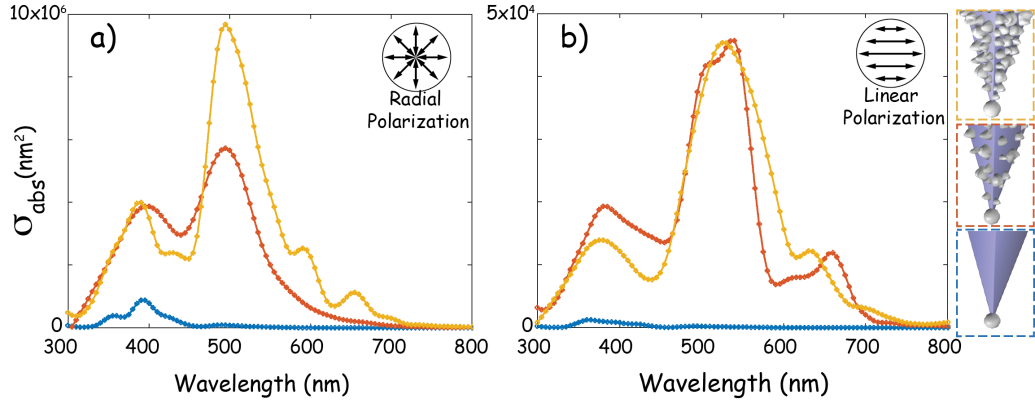


Figure 3.19: absorption spectrum of single NP tip (blue line), tip with coarse distance between the particles (red line) and “realistic” tip (yellowish line) for a radially polarized beam. b) same calculations for a linearly polarized beam. Images at the right side display the sketch of the respective system. Note that the specific positioning of the tip in the linear polarization case results effectively in z -polarization parallel to the tip’s main axis.

As the first comparison between the model and the actual TERS tip, the absorption spectrum of a plasmonic probe was calculated. In addition to the parametrized 3D tip, Figure 3.18 (b), two other cases were considered: a tip with bigger interparticle distances and a bare tip with only single front-most NP. In Figure 3.19, for both linearly and radially polarized illumination, an increase in particle density generally results in stronger far-field signals in the mode, which is in line with the findings of Taguchi et al [118]. The modeled far-field absorption spectra for both polarizations show multiple peaks, which agrees with previous research on planar SERS substrates [124]. Due to variations of the NP structure over the modeled area, i.e., size and inter-particle distances, in the SEM-based model, a direct assignment of the respective peaks in Figure 3.19 is not as straightforward as for the dimer case. However, the local occurrence of super-radiant, sub-radiant, and Fano-modes of randomly distributed silver NPs of arbitrary size and shape have been reported for isolated NP clusters [124, 152, 153]. Additionally, the resulting observed absorption is a superposition of all these modes. The spectrum (yellow line) from

Figure 3.19, (a) indicates that the evaporation-based TERS tips provide a strong resonance at $\sim 500\text{ nm}$, particularly for the RPB illumination, which matches experimental evidence as well as the theoretical investigations [154]. Even for the tip with larger interparticle distances (red spectrum in Figure 3.19), this signal is still strong and spectrally similar; hence, indicating at least for the far-field, no significant differences should be expected. In Figure 3.19, (b) the tip are irradiated with a linearly polarized beam. Note that the specific positioning of the tip in the linear polarization case results effectively in z -polarization parallel to the tip's main axis.

For the directly parametrized tip (yellow line) and the tip with larger gaps between NPs (red line), the intensity of absorption spectra in the $500\text{-}550\text{ nm}$ range is almost equal but essentially providing sufficient enhancement for a TERS experiment albeit, as expected, weaker than for the radially polarized light. The reference model of the single NP tip is shown in Figure 3.19, (a) and (b) (blue curve) for both polarizations. The comparatively weak peaks between $350\text{-}400\text{ nm}$ correspond to localized plasmons of silver NPs. Qualitatively, the results are good in agreement with previous publications, as the involvement and specifically further enhancement by neighboring nanoparticles are confirmed [118, 124]. However, the absorption spectrum alone should not be considered as the only characterization of the performance of the tip. The near-field response of the probe is also a crucial criterion, which has to be considered carefully.

Near-field response of rough silver based plasmonic probes

This section will address the near-field enhancement “felt” by a specimen positioned 1 nm underneath the frontmost NP. Similar to the previous far-field investigations, three tip shapes will be considered: the directly parametrized model from the TERS tip SEM images, the same tip with enlarged interparticle distances, and a single NP tip. The frontmost particle had the same size and shape in all cases. A plain single NP in the air was also included for further comparison. Figure 3.20 shows the wavelength dependence of the enhancement for radial (Figure 3.20, a) and linear polarization, respectively (Figure 3.20, b). Clearly, the free-standing NP case can be easily distinguished by spectral position, intensity, and the number of resonances. However, as long as silver nanoparticles are placed on a *Si* tip, additional peaks in the field enhancement appear. In this regard for the field enhancement, two phenomena are influential. The first one is the plasmon resonance whose peak is distinguishable in all the modeled cases, including a free-standing NP. Depending on the geometry of the tips and the illuminations, this peak is detectable in the range of $350\text{ to }410\text{ nm}$ in Figure 3.20. However, it has been shown that in plasmonic (even dielectric) nanoantenna, if no plasmon resonance is trig-

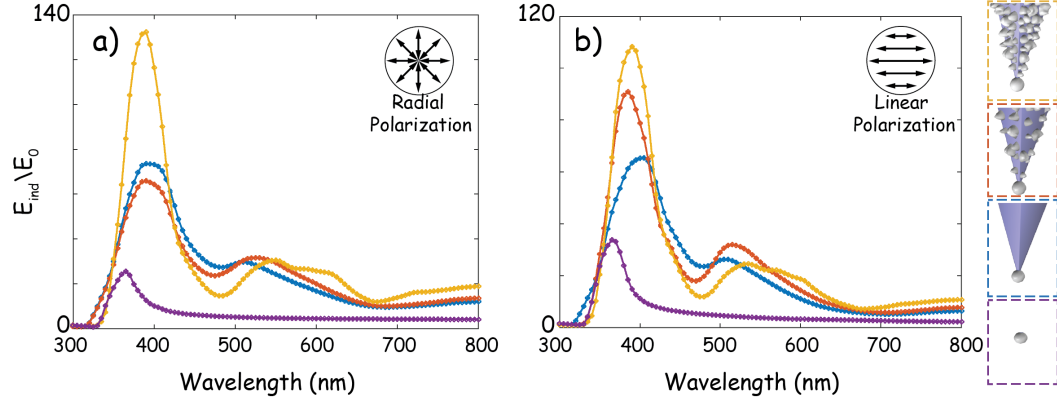


Figure 3.20: a) near-field enhancement spectrum of a free-standing NP (purple line), single NP tip (blue line), tip with large inter-particle distance (red line) and directly parametrized tip (yellowish line) under illumination of radially polarized beam on the molecule placed 1 nm beneath the front-most NP. b) same calculations for a linearly polarized beam. Images at the right sketch the respective systems. Here again for the linear polarization case the tip is specifically positioned off-center to optimize the z -coupling efficiency.

gered, the structure can still exhibit non-resonant field enhancement due to field line crowding at the apex of sharp metal tips. The lightning-rod effect is a well-known non-resonant (broadband) phenomenon that involves the robust enhancement of the local near field of incident radiation in the vicinity of a sharp corner or tip as a consequence of the high local charge densities present near such structural components [91–94]. Therefore, the lightning-rod effect is responsible for additional peaks in Figure 3.20. It is visible that plasmon modes, 350 to 410 nm , are sharper, stronger, and more influenced by geometry and the illumination, which in principle shows that it is a resonant phenomenon. On the other hand, in the case of nanoantenna (all the cases in Figure 3.20 except free-standing NP), broader peaks are emerging, which are weaker and less affected by geometry and illumination. As expected, this already strongly indicates that the “roughness,” i.e., many-particle systems, are advantageous for TERS tips. Interestingly the linear polarized case seems to provide a stronger enhancement attributed to the specific geometry used here for illumination. Rather than positioning the tip in the focus center, we position the tip at the maximum site for z -coupling efficiency. Experimentally, this is also very important when using LPB from below, since the z -contributions cancel out in the center of the focus, and the coupling between plasmon and sample would be very weak. For the other geometries, the radial polarization is more advantageous, most likely due to the efficient coupling

also at more distant parts of the tip shaft. Comparing the far- and near-field behavior shown in Figure 3.19 and Figure 3.20, respectively, the spectral positions of the resonances are shifted, and also the intensity ratios are different. Evidently, the particle interacting with the specimen dominates the plasmon resonance position in the optical near-field, while the neighboring NPs mostly influence the field enhancement itself. Particularly a comparison between the free single NP case and the three tip models shows that the largest shift for the plasmon resonance occurs when the tip slightly distorts the plain silver sphere. Introducing a spherical particle at the end of the tip, simplifying our model, allows us to compare and single out specific contributions. A full assessment of the shape of the particular tips would require a much denser grid and presently would limit our ability to include larger portions of the tip shaft. The very localized effect of even single atomic protrusions on the localized surface plasmon resonance has been pointed out in previous experiments [125, 155]. It indicates that the necessary precision required for a full FEM investigation is yet out of range. Of great interest for experimental applications is the spectral position of the plasmon resonance. The values in Figure 3.20 for all near-field cases apparently are in the violet spectral regions, whereas the far-field data in Figure 3.19, indicate major resonances in the green to yellow spectral region. For TERS application, the local near-field contributions must be considered, rendering the results of Figure 3.20, out of the reach of standard Raman excitation wavelengths (e.g., 488, 515, 532 nm). It is important to note that already small deviations from a sphere (and sample substrate) will induce a redshift of the localized surface plasmon resonance [156–160]. In a recent experiment, the actual spectral near-field position of a plasmon resonance could be determined directly, clearly confirming that the tips resonance is in reach of the above-mentioned excitation wavelengths [161]. Furthermore, it is also important to mention that current investigations do not consider any chemical contribution to the overall enhancement [162–165].

Scattering directionality pattern of the tip

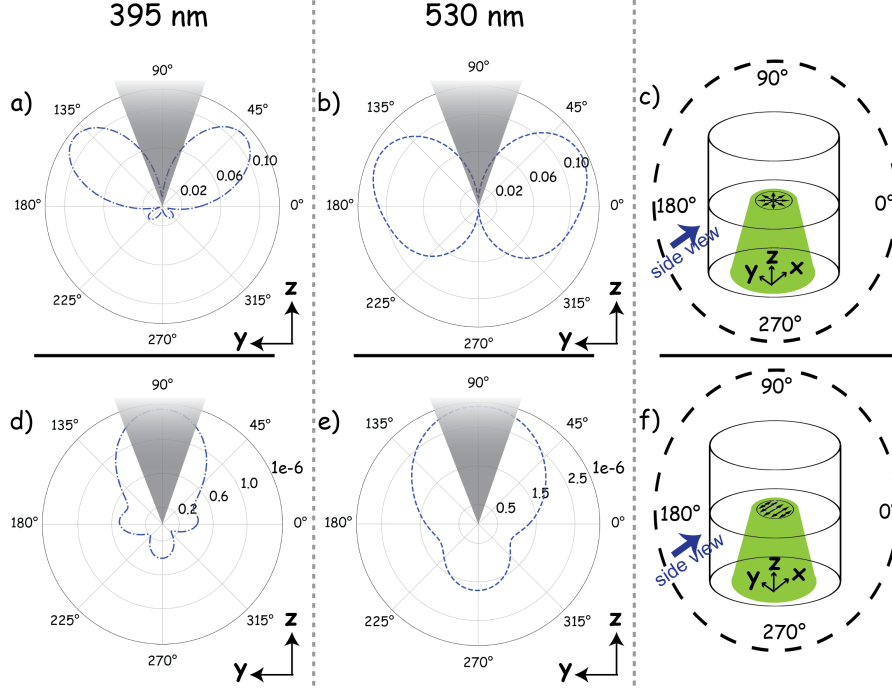


Figure 3.21: a) scattering pattern of the tip under radially polarized beam illumination from below in 395 nm . b) in 530 nm . d) under linearly polarized light illumination in 395 nm from below and e) in 530 nm . Small numbers show intensity of normalized far-field, E_{far} , c) and f) represent the schematic picture of the tip under respective illuminations.

An often-overlooked part of a SNOM experiment is the illumination and detection geometry. While mainly governed by sample and instrumental conditions, a closer look into the tip's influence to the best of our knowledge has not been discussed widely. The following part investigates the radiation pattern of a plasmonic tip. The calculations are done for the parametrized tip only and specifically for the prominent near-field modes at 395 nm and 530 nm , respectively. For the simulations of this part, the same method as presented in 3.2.3 is used. The whole tip was enclosed by a virtual sphere defined as the far-field domain for the model. A Gaussian beam was focused on the tip with an NA of 1.25 . Figure 3.21 shows the calculated normalized far-field E_{far} in this model. Small numbers inside each graph refer to the magnitude of E_{far} . Figure 3.21, c) and f) line out the geometry, polar coordinates, and polarization direction for radial and linear polarization illuminations. The schematic tip shape in the Figure 3.21 displays the polar coordinates blocked by the tip and cannot be detected/collected. Interestingly, the radiation pattern of the two resonances

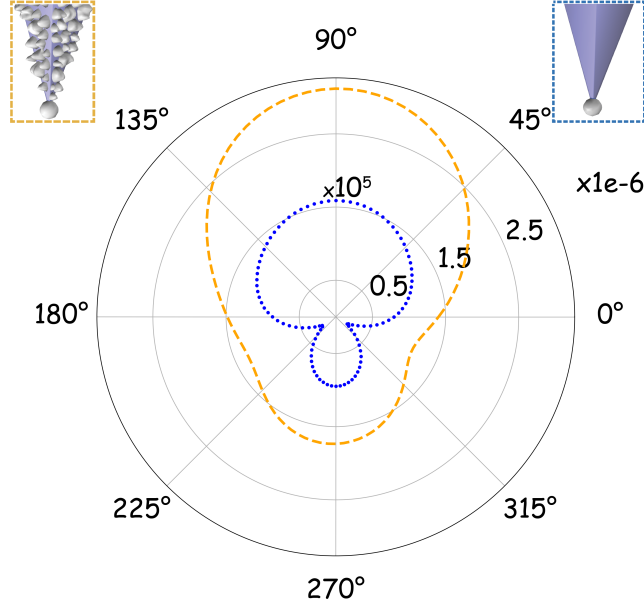


Figure 3.22: Far-field radiation E_{far} of a single NP and many NP tips under illumination of a linearly polarized green laser (532 nm). Note that in this case tip is placed at the center of the beam.

using radially polarized illumination (Figure 3.21, (a) and (b)) is really not identical. While two clear major lobes pointing away from the source can be observed for the 395 nm resonance, the directionality is much more uniform for the 530 nm mode (Figure 3.21, (b)). Figure 3.21, (d) and (e) reveal that for linearly polarized light both resonances show quite a different behavior; here, the main scattering efficiency points directly away from the collection part (red arrow in Figure 3.21 (c) and (f)). Such a directionality of the signal could strongly affect the signal collection efficiency of any SNOM setup and will therefore be investigated more closely. In addition to the mere collection efficiency, an angle-dependent investigation should provide information about the particular plasmon mode that is excited with a given laser line. In the last part of this section, far-field radiation of the single NP and many-particle tip are compared. Figure 3.22 shows the E_{far} of a single NP (blue dotted curve) and many-particle tip (dashed orange curve). For green laser illumination, many-particle tip's far-field scattering is more than 10^5 stronger than that of a single NP tip.

In conclusion, modeling a tip revealed that at 530 nm illumination wavelength, both many-particle and a single NP tip showed comparable near-field enhancement since, at this wavelength, tips show the lightning-rod effect (see Figure 3.20). Far-field radiation also displayed that a many-particle tip shows much stronger far-field scattering power compared to a single NP tip (see Fig-

ure 3.22). From these two calculations, one can suppose that a single NP tip can perform well enough when a SNOM measurement is illuminating and detecting in the near-field region (as in PiFM). On the other hand, for the SNOM-type experiments where the detection is performed in the far-field domain, tips with stronger far-field scattering intensity, many-particle tips, are better options. This finding is put into practice in 4.2.3.

3.2.5. Modeling the Mechanical Properties of the Tips

Up to now, we merely focused on the optical properties of the probes. This part investigates the mechanical properties of the tips that are mostly used in experiments. More specifically, we discuss oscillation of higher harmonics of the *Tap300Al-G* and *Tap190Al-G* from BudgetSensors. To model these AFM probes, we used the precise geometry provided by the company [37], shown in Figure 2.2. We used Comsol multiphysics only this time, instead of the Wave-Optics module, the Eigenfrequency module is used. Only the tip part (shown with dashed circles in Figure 2.2) is modeled in our simulation. One end of the tip, in reality attached to the cantilever’s larger part, is modeled as a ”fixed point”. The first four eigenfrequencies and the corresponding total deflection of a *Tap190Al-G* tip are shown in Figure 3.23. First, we can see that based on our model, the fundamental resonance frequency f_1 is equal to 190.69 kHz , which is in perfect agreement with the value specified by the manufacturer ($190 \pm 30\text{ kHz}$). So we can be sure that the tip is well modeled. From the Figure 3.23, it

Tip	Resonance Frequency (kHz)	Oscillation	Mode
<i>Tap300Al-G</i>	347.27	Out of plane	Vertical
<i>Tap300Al-G</i>	2195	Out of plane	Vertical
<i>Tap300Al-G</i>	2469.3	In-plane	Horizontal
<i>Tap300Al-G</i>	2835.2	Twisting	Torsional
<i>Tap300Al-G</i>	6141.4	Out of plane	Vertical
<i>Tap190Al-G</i>	190.69	Out of plane	Vertical
<i>Tap190Al-G</i>	1006.8	In-plane	Horizontal
<i>Tap190Al-G</i>	1192.3	Out of plane	Vertical
<i>Tap190Al-G</i>	2095	Twisting	Torsional
<i>Tap190Al-G</i>	3323.5	Out of plane	Vertical

Table 3.2: First five resonance frequencies and their corresponding oscillation of *Tap300Al-G* and *Tap190Al-G* tips.

is apparent that, there are three types of tip oscillation: out of plane ((a) and (c)) and in-plane ((b) and twisting (d)). The vertical deflections (here in the z -direction), especially the fundamental resonance frequency (f_1), are ideal for

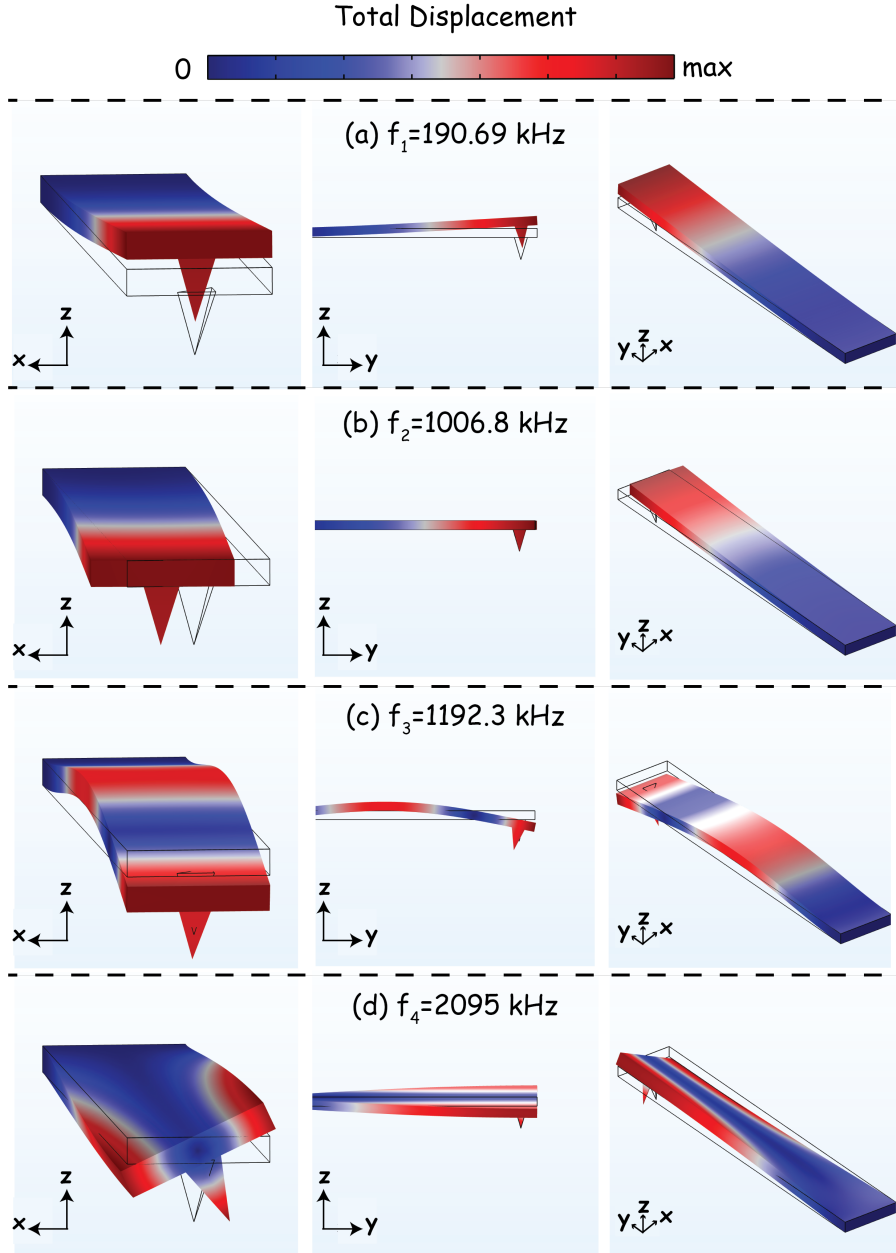


Figure 3.23: The first four eigenfrequencies and corresponding deflection of *Tap190Al-G* from three different view (left, middle and right columns). $f_1 = 190.69$ kHz (a), $f_2 = 1006.8$ kHz (b), $f_3 = 1192.3$ kHz (c) and $f_4 = 2095$ kHz (d). Dark red represents the maximum deflection and dark blue shows no deflection.

the typical tapping mode AFM. However, generally tapping mode is insensitive to lateral force gradients. That is why the twisting oscillation of the tip can be utilized as a torsional mode. This torsional vibration has been recently introduced. In this method a tip is vibrated in the torsional mode at high-frequency [166, 167]. Figure 3.23 (d) reveals the oscillation scheme in torsional mode. Higher harmonic vertical deflection of the tip is also instrumental. It plays a crucial role in recent near-field techniques such as photo-induced force microscopy, which is expansively discussed in the next chapter. Table 3.2 shows summary of the mechanical properties of the *Tap300Al-G* and *Tap190Al-G* tips.

In this section, we presented a model to investigate the mechanical properties of the tips. Based on the task and demand, this simulation enables us to acquire the resonance frequency of the tip in either tapping or torsional modes, which is generally not available from the manufactures.

4. Photo-induced Force Microscopy (PiFM)

4.1. Principles of PiFM

PiFM is an extremely sensitive nanoscale spectroscopic technique from the visible [27–34] to the mid-infrared [168–174], that measures the photo-induced force between the sharp metal tip and the sample with high spatial resolution. The force involves the interaction between induced dipole and thermal expansion [28, 175]. The tip-enhanced thermal expansion force is dominant near the molecular resonance of most dielectric materials, whereas the induced electromagnetic dipole force (optical field gradient force) is dominant in plasmonic and phononic materials [169]. In this thesis we do not consider the thermal expansion effects. As PiFM is an AFM based technique, it is ideally suited to utilize in combination with a TERS setup.

In principle, AFM-based spectroscopic methods can be divided, based on applied detection scheme, into two groups. Those that rely on a mechanical detection and those that obtain signals via photon detection. Both tip-enhanced Raman spectroscopy (TERS) and scattering-type scanning near-field optical microscopy (s-SNOM) are techniques that involve photon detection in the far-field. Then some methods are utilized to separate the near-field scattering signal from background signals generated by far-field scattering and reflection. In contrast, photo-thermal induced resonance (PTIR) [176–180] and photo-induced force microscopy (PiFM) [27, 28, 31, 168, 181] are mechanical detection based techniques, which rely intrinsically on a near-field sensing method and thereby reduce the challenge of dealing with background scattering and reflection [182]. An AFM can be considered as a mechanical resonator operated in feedback loop. Such a system is susceptible to topographic changes because a sharp tip is placed on the resonator (cantilever or quartz tuning forks) and the proximity to the surface increases the tip-sample interactions, which in turn leads to changes the resonator properties, i.e. cantilever deflection and the resonance conditions. As the tip is scanned over the sample, the topography can be mapped by detecting these changes. Generally, the mechanical resonances can be considered as sensors. For example, in tapping mode AFM, the cantilever oscillates at a frequency equal to the cantilever’s first resonant frequency (f_0). The optical detection system that monitors the cantilever motion is fed into the input of a lock-in amplifier referenced by the drive signal that vibrates the cantilever; as the tip approaches the surface, the lock-in am-

plitude decreases due to the increasing force interaction. Maintaining a fixed predetermined amplitude, so called set-point, the Z-scanner compensates for the amplitude drop/gain by moving to separate/bring closer the tip and sample. Any system which can be described to a first approximation as a classical harmonic oscillator, exhibits several additional eigenmodes in addition to the fundamental one that can also be used as independent sensors for additional detection channels. This forms the basis of PiFM. A typical PiFM setup is schematically outlined in (Figure 4.1). Next the basic principles for an experimental realization of a PiFM measurement are presented. In 4.1.2 we will show that, the photo-induced force includes both gradient and scattering forces [27]. In 4.1.2 we will show that the gradient force arises from a field gradient at the tip-sample interface resulting from the dipole-dipole interaction between the induced dipole on the sample and the image dipole on the tip, leading to an attractive force between the two. The scattering force is a direct interaction between the incident light and the tip due to the transfer of photon momentum and does not contain any chemical information about the sample. The incident light can also cause heating of the tip and cantilever, leading to cantilever motion via non-uniform thermal expansion which is more pronounced with infrared illumination [168]. The chemical information of the sample lies in the gradient force, which depends on the wavelength-dependent polarization of a sample. The scattering forces in the near-field region have slight local variation [27] and the targeted chemical information is in the gradient force 4.1.2, which is highly localized, "sideband" detection based on the measurement of the force derivative can be used to suppress the unwanted forces. In this approach, the laser modulation frequency f_m is chosen so that when added to f_0 , it equals to f_1 : $f_m + f_0 = f_1$ [27]. f_m was chosen to set the lock-in reference (f_{ref}) precisely to the cantilever's second mechanical resonant oscillation frequency to take advantage of the high Q factor to improve the signal-to-noise ratio. In the above mentioned example of tapping mode AFM, a laser can be focused on the tip-sample region and modulate at $f_m = f_1$ to "directly" detect the photo-induced force.

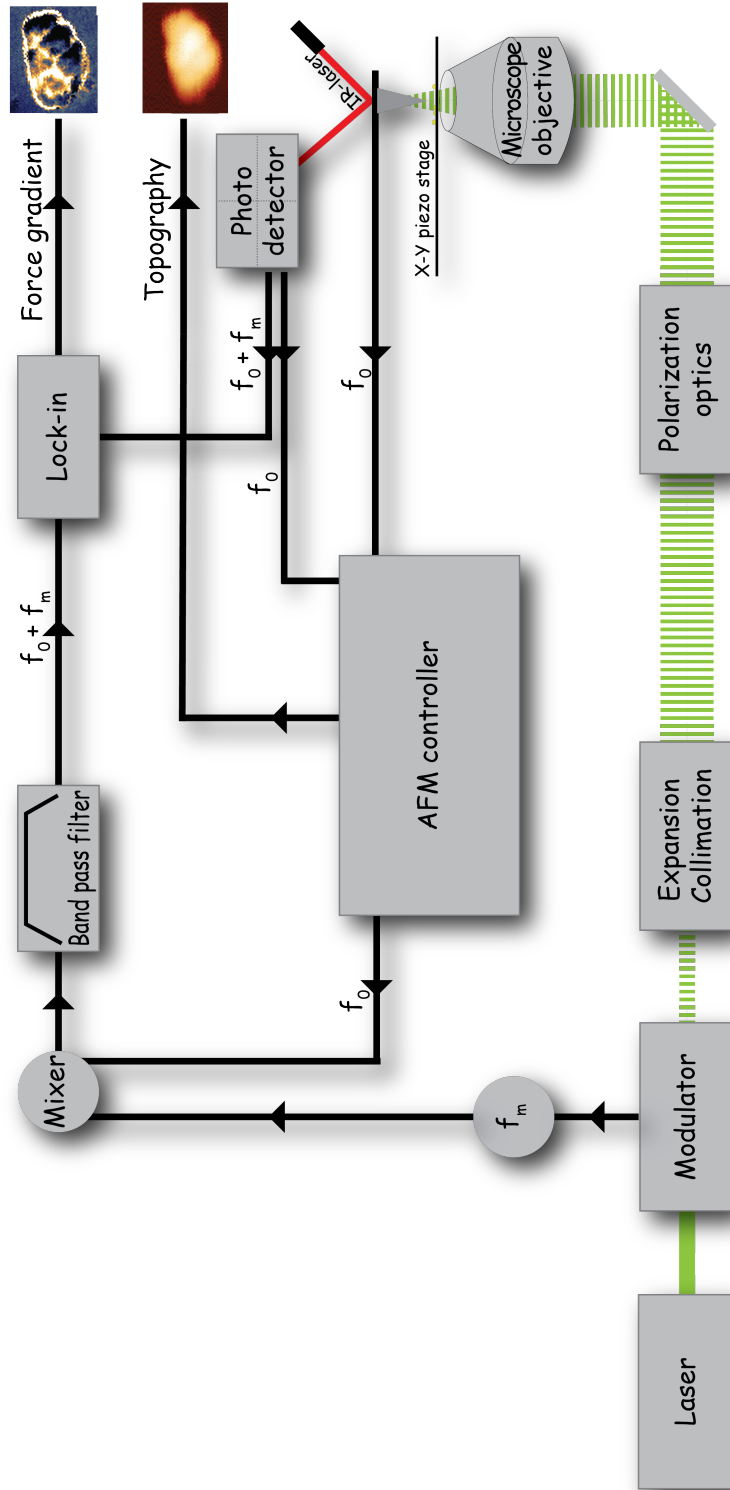


Figure 4.1: Schematic of a photo-induced force microscopy experiment. f_0 is the frequency that cantilever is oscillating at and f_m is laser modulation frequency.

In a nutshell, a PiFM setup is built around a tapping mode AFM, where the cantilever is excited at its first mechanical resonance f_0 shown in Figure 4.1. The laser beam is modulated at frequency f_m which modulates the image force gradient between object features and their mirror images also at f_m . This force gradient modulation in turn modulates the cantilever mechanical resonance frequency generating sidebands at $f_m + f_0$ and $f_m - f_0$. The $f_m + f_0$ sideband which, as mentioned earlier, is arranged to lie on top of the second mechanical resonance of the cantilever. The reference for the lock-in is derived by mixing the f_0 (taken from controller) and f_m (taken from modulator) followed by a bandpass filter centered at $f_m + f_0$. Hence after demodulating the inputs by lock-in amplifier, the extracted gradient force in PiFM (originally called “image force microscopy” [27]) is simultaneously detected with the topography while the object is raster scanned.

4.1.1. Theory of Sideband Coupling

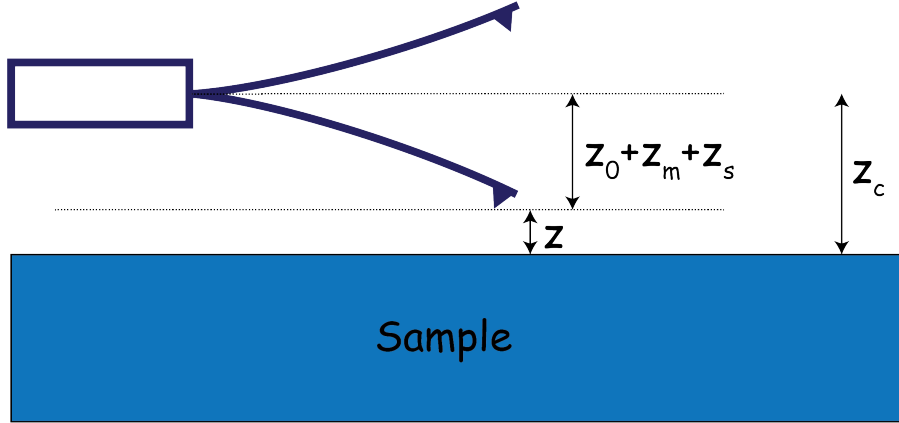


Figure 4.2: Dynamic motion of a cantilever.

After a brief introduction of the PiFM, the next key step is to understand the way the time-averaged photo-induced force is measured. In the context of multifrequency AFM, here a quantitative theory of sideband coupling for probing force gradients detected in PiFM is developed. This description follows largely the outline presented in [183]. It should be mentioned that all the analysis presented in this section is independent of the origin of the photo-induced force and is valid for any form of the photo-induced response in the system.

The dynamics of motion of a continuous beam system (cantilever tip system) is described by the Euler-Bernoulli model. The motion of the tip can be represented by a point-mass model and described by the superposition of its eigenmodes [184, 185]. Since the higher eigenmodes contribute negligibly

to the cantilever motion [186], we can assume, for our discussion here, that only the fundamental ($i = 0$) and the first mechanical resonance ($i = 1$) are important. Consequently, the equation of motion of the tip-sample system in two degrees of freedom are given by:

$$m\ddot{z} + b_0\dot{z} + k_0z = F(z(t), t) \quad (4.1)$$

$$m\ddot{z} + b_1\dot{z} + k_1z = F(z(t), t) \quad (4.2)$$

where m is the mass of the cantilever, $F(z(t), t)$ is the total external force including a tip-sample interaction force, and k_i and b_i are the i th spring constant and damping coefficient of the cantilever, respectively. The sideband motion (with frequency of $f_{s\pm}$) is induced by coupling the modulated force gradient (with frequency of f_m) with the carrier frequency (f_i) (here $f_{s\pm} = f_0 \pm f_m$). The instantaneous tip-sample distance is represented by $z(t) \cong z_c + z_0(t) + z_m(t) + z_s(t) + 0(\varepsilon)$ where z_c is the equilibrium position, z_0 is the coordinate of the carrier motion of the fundamental eigenmode, z_m describes the motion due to the modulated force, and z_s is the relevant coordinate for sideband-coupled motion (see Figure 4.2). Assuming that the motion is sinusoidal, the instantaneous tip-sample distance is given as:

$$z(t) \approx z_c + z_0(t) + z_m(t) + z_s(t) + 0(\varepsilon) \quad (4.3)$$

$$z_0(t) \approx A_0 \sin(\omega_0 t + \theta_0) \quad (4.3a)$$

$$z_m(t) \approx A_{m0} \sin(\omega_m t + \theta_{m0}) + A_{m1} \sin(\omega_m t + \theta_{m1}) \quad (4.3b)$$

$$z_s(t) \approx A_{s0} \sin(\omega_{s\pm} t + \theta_{s0}) + A_{s1} \sin(\omega_{s\pm} t + \theta_{s1}) \quad (4.3c)$$

where $\omega_{s\pm} = \omega_m \pm \omega_0$. A_{mi} and θ_{mi} are the amplitude and phase that are driven by the photo-induced force acting on the fundamental (previously introduced as f_0) and first eigenmodes (previously introduced as f_1); A_{si} and θ_{si} are the amplitude and phase driven by the interaction responsible for coupling the eigenmodes. Substituting equation 4.3 into equations 4.1 and 4.2 by multiplying both sides of the resulting equation by $\sin(\omega_j t + \theta_j)$ and $\cos(\omega_j t + \theta_j)$, followed by an integration over the oscillation period, the following general relations for the amplitude and phase of the motions are obtained:

$$(k_i - m\omega_j^2) \frac{A_j}{2} = \frac{1}{T} \int_0^T F(z(t), t) \sin(\omega_j t + \theta_j) dt \quad (4.4)$$

$$\frac{b_i \omega_j A_j}{2} = \frac{1}{T} \int_0^T F(z(t), t) \cos(\omega_j t + \theta_j) dt \quad (4.5)$$

where $i = 0, 1$, $j = 0, m_i, s_{i\pm}$. Equations 4.4 and 4.5 are the general expressions of the sideband coupling theory in multifrequency atomic force microscopy. If

the form of $F(z(t), t)$ is known, the amplitudes A_0 , A_{mi} , $A_{si\pm}$ and the phase shifts θ_0 , θ_{mi} , $\theta_{si\pm}$ can be calculated through numerical integration. Next, we will consider the small oscillation limit and apply the sideband coupling theory to the case where photo-induced forces are detected.

Under the assumption that the oscillation is sufficiently small, equations 4.4 and 4.5 can be analytically solved considering z_s as perturbation. Note that this small oscillation approximation is equivalent to the first-order approximation of the general motion of the cantilever system [187]. The total external force can be expanded at the equilibrium position z_c as follows:

$$F(z(t), t) \approx F(z_c) + \left(\frac{\partial F}{\partial z} \right)_{z_c} (z - z_c) + \dots \quad (4.6)$$

We assume that the higher order coupling terms (second order and higher) can be ignored in the small oscillation limit. In PiFM with sideband mode detection, we modulate the fundamental eigenmode of the cantilever for tracking the topography and modulate the optical force at the angular frequency ω_m . Therefore, the total external force can be written as:

$$F(z(t), t) = F_0 \cos(\omega_0 t) + F_{int}(z) + F_{pif}^{DC}(z) + F_{pif}^{AC}(z) \cos(\omega_m t + \theta_m) \quad (4.7)$$

where F_0 is the driving force for the fundamental resonance, and F_{int} is a mechanical tip-sample interaction force that can be generally described as the sum of a conservative and a nonconservative force: $F_{int}(z) = F_c(z) - \Gamma(z)\dot{z}$ [188]. Such a form of the force provides a good description of the energy dissipation of the cantilever [189, 190]. In the small oscillation limit, nonvelocity dependent effects, such as the hysteresis effect, can be assumed to be small [191]. The photo-induced force contributes through the third and fourth term on the righthand side of equation 4.7, and is given as $F_{pif}^{DC}(z) + F_{pif}^{AC}(z) \cos(\omega_m t + \theta_m)$. The origin of the sideband signal derives from the product of the carrier motion and the modulated force. Inserting equations 4.3 and 4.7 into equation 4.6, and by considering the higher order terms are sufficiently small, the total force terms are rewritten as:

$$F_c(z) \approx F_c(z_c) + \left(\frac{\partial F_c}{\partial z} \right)_{z_c} (z_0 + z_m + z_s) \quad (4.8)$$

$$\Gamma(z)\dot{z} \approx \left(\Gamma(z_c) + \left(\frac{\partial \Gamma}{\partial z} \right)_{z_c} (z_0 + z_m + z_s) \right) \dot{z} \quad (4.9)$$

$$F_{pif}^{DC}(z) \approx F_{pif}^{DC}(z_c) + \left(\frac{\partial F_{pif}^{DC}}{\partial z} \right)_{z_c} (z_0 + z_m + z_s) \quad (4.10)$$

$$F_{pif}^{AC}(z) \cos(\omega_m t + \theta_m) \approx F_{pif}^{AC}(z_c) \cos(\omega_m t + \theta_m) + \left(\frac{\partial F_{pif}^{AC}}{\partial z} \right)_{z_c} (z_0 + z_m + z_s) \cos(\omega_m t + \theta_m) \quad (4.11)$$

the second term in equation 4.11 gives the coupled response between all the motions through the modulated photo-induced force gradient. The sideband force, however, is the modulated photo-induced force gradient coupled with the carrier motion (z_0), defined in 4.3a, as given below:

$$\begin{aligned} F_{pif}^{AC}(z) \cos(\omega_m t + \theta_m) z_0 &= \left(\frac{\partial F_{pif}^{AC}}{\partial z} \right)_{z_c} \cos(\omega_m t + \theta_m) A_0 \sin(\omega_0 t + \theta_0) \\ &= \left(\frac{\partial F_{pif}^{AC}}{\partial z} \right)_{z_c} \frac{A_0}{2} \sin((\omega_m + \omega_0)t + (\theta_m + \theta_0)) \\ &\quad - \left(\frac{\partial F_{pif}^{AC}}{\partial z} \right)_{z_c} \frac{A_0}{2} \sin((\omega_m - \omega_0)t + (\theta_m - \theta_0)) \end{aligned} \quad (4.12)$$

where $\omega_s = \omega_m \pm \omega_0$ are the sum and difference frequencies at which the sideband coupled signal is detected. In the remainder of this work, we will choose ω_{s+} for our sideband detection. By setting the sideband frequency to coincide with the first resonance frequency, $\omega_s \equiv \omega_{s+} = \omega_1$, the sideband motion is amplified by this eigenmode due to high Q-factor as mentioned in the previous chapter. In general ω_{s+} is well separated from the fundamental mechanical resonance. Therefore, the amplitude of the sideband mode can be approximated by $A_s \approx A_{s1+} \gg A_{s0+}$ and thus $z_s(t) \approx A_s \sin(\omega_s t + \theta_s)$ and $F_{side} = \frac{A_0}{2} \left(\frac{\partial F_{pif}^{AC}}{\partial z} \right)_{z_c} \sin((\omega_m + \omega_0)t + (\theta_m + \theta_0))$. As mentioned earlier, the fundamental mechanical resonance of the cantilever is externally driven with the F_0 force and the frequency of ω_0 , while the higher-order resonance is actively driven by the optical force, F_{side} . The interaction force, F_{int} (which bundles all relevant van der Waals and Casimir forces present in AFM) and F_{pif}^{DC} (which includes all the constant forces applied on the tip due to illumination of laser light) act on the motion of both resonances. Now we are facing the following equations to solve and obtain analytical expression for A_s and A_0 . By considering the above approximation, the integral equations for the carrier and sideband motions in 4.4 and 4.5 are rewritten as:

$$(k_0 - m\omega_0^2) \frac{A_0}{2} = \frac{1}{T} \int_0^T [F_0 \cos(\omega_0 t + \theta_0) + F_c(z) - \Gamma(z) \dot{z} + F_{pif}^{DC}(z)] \sin(\omega_0 t + \theta_0) dt \quad (4.13)$$

$$\frac{b_0\omega_0 A_0}{2} = \frac{1}{T} \int_0^T [F_0 \cos(\omega_0 t + \theta_0) + F_c(z) - \Gamma(z)\dot{z} + F_{pif}^{DC}(z)] \cos(\omega_0 t + \theta_0) dt \quad (4.14)$$

$$(k_1 - m\omega_s^2) \frac{A_s}{2} = \frac{1}{T} \int_0^T [F_c(z) - \Gamma(z)\dot{z} + F_{pif}^{DC}(z) + F_{side}] \sin(\omega_s t + \theta_s) dt \quad (4.15)$$

$$\frac{b_1\omega_s A_s}{2} = \frac{1}{T} \int_0^T [F_c(z) - \Gamma(z)\dot{z} + F_{pif}^{DC}(z) + F_{side}] \cos(\omega_s t + \theta_s) dt \quad (4.16)$$

Now using equations 4.8, 4.9 and 4.10 and substituting them into equations 4.13 and 4.14 carrier motion can be obtained. Sideband motion also could be achieved by solving equations 4.15 and 4.16. This way simplified equations will be achieved as below:

$$(k_0 - \bar{k}_c - m\omega_0^2) A_0 = F_0 \sin \theta_0 \quad (4.17)$$

$$(b_0 - \Gamma)\omega_0 A_0 = F_0 \cos \theta_0 \quad (4.18)$$

$$(k_1 - \bar{k}_c - m\omega_s^2) A_s = -\frac{A_0}{2} \left(\frac{\partial F_{pif}^{AC}}{\partial z} \right)_{z_c} \cos(\theta_s - (\theta_m - \theta_0)) \quad (4.19)$$

$$(b_1 - \Gamma)\omega_s A_s = \frac{1}{2} \left(\frac{\partial F_{pif}^{AC}}{\partial z} \right)_{z_c} \sin(\theta_s - (\theta_m - \theta_0)) \quad (4.20)$$

where $\bar{k}_c = \frac{\partial \bar{F}_c}{\partial z}|_{z_c}$ and $\bar{F}_c = F_c + F_{pif}^{DC}$ is effective conservative force. By squaring and summing equations 4.17 and 4.19 we obtain the amplitude of the carrier motion as:

$$A_0 = \frac{F_0}{\sqrt{m^2(\omega_0'^2 - \omega_0^2) + b_0'^2 \omega_0^2}} \quad (4.21)$$

with $b_0' = b_0 + \gamma(z)$ is an effective damping parameter and $\omega_0' = \sqrt{\frac{(k_0 - \bar{k}_c)}{m}}$ accounts for frequency shift induced by the force gradient. By introducing the transfer function as below:

$$G_i(\omega_j) = \frac{1}{\sqrt{m^2(\omega_i'^2 - \omega_j^2) + (b_i' \omega_j)^2}} \quad (4.22)$$

where $i = 0, 1$ and $j = 0, m, s$. Using the transfer function we can obtain analytical expression for carrier and sideband motion as:

$$A_0(\omega_0) = G_0(\omega_0) F_0 \quad (4.23)$$

$$A_s(\omega_s) = G_1(\omega_s) \frac{A_0}{2} \left(\frac{\partial F_{pif}^{AC}}{\partial z} \right)_{z_c} \quad (4.24)$$

Equation 4.23 is the unperturbed solution of the carrier motion and equation 4.24 is the first order perturbation solution due to the presence of the modulated force. We can see that the amplitude of the sideband motion A_s is proportional to the force gradient of the photo-induced force ($\frac{\partial F_{pif}^{AC}}{\partial z}$) rather than to the photo-induced force itself. By doing same analytical approach for direct detection (when $\omega_m = \omega_1$), amplitude of direct motion ($A_d(\omega_1)$) expressed as below:

$$A_d(\omega_1) = G_1(\omega_1) F_{pif}^{AC}(z_c) \quad (4.25)$$

Because the detected amplitude in the direct mode is directly related to F_{pif}^{AC} , the signal contains both localized (attractive) and nonlocalized (repulsive) force contributions [29]. In contrast, the sideband mode is related to the force gradient of the photo-induced force, $\frac{\partial F_{pif}^{AC}}{\partial z}$. Since the gradient of localized force contributions is much higher than the gradient of the slowly varying nonlocalized forces, the sideband is much more sensitive to localized tip-sample interactions. The reduced spatial scale at which these interactions are prominent gives rise to a high spatial resolution and improved contrast compared to what is seen in the direct detection mode.

4.1.2. Theoretical Investigation of the Optical Force Interaction at Nano Sclae

In the previous section, the theory behind the sideband detection scheme was presented. Now, it is time to investigate the forces measured in that scheme; hence, a brief overview of the theoretical background of optical forces is presented. In principle two approaches for modeling the optical force interaction are pursued, namely the dipole-dipole approximation (see 4.1.2) and Maxwell stress tensor (see 4.1.2).

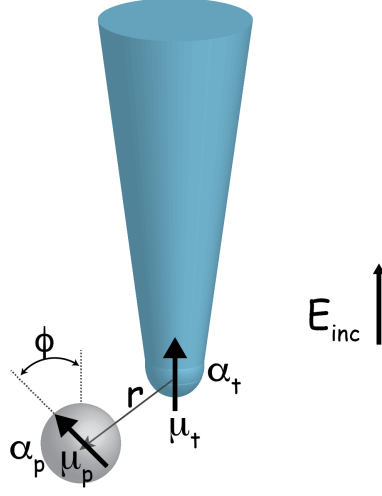


Figure 4.3: Induced dipole moments of an AFM tip and a particle with incident electromagnetic field E_{inc} , where r is the center of mass coordinate, μ_t and α_t (μ_p and α_p) are dipole moment and polarizability of the tip (sample), respectively.

Dipole-Dipole Approximation (DDA)

In DDA the interaction between tip and sample can be considered equivalent to the interaction between dipoles generated by absorption in the sample and the corresponding mirror-image dipoles in the tip. In fact, several mirror images can arise in the tip-sample-substrate system, which leads to an attractive "image force" that corresponds to the wavelength-dependent optical absorption of the sample absorption [27]. Especially for a linearly polarized beam, this approach is advantageous to obtain a simple analytical view of the different forces present in photo-induced interactions.

To begin to develop a theory of the optical force interactions at the AFM tip, first a polarizable particle illuminated with a monochromatic electromagnetic wave, of angular frequency ω is considered. In this case the time harmonic electric and magnetic field components at location \mathbf{r} can be described by:

$$\mathbf{E}(\mathbf{r}, t) = \text{Re}[\mathbf{E}(\mathbf{r})e^{-i\omega t}] \quad (4.26)$$

$$\mathbf{B}(\mathbf{r}, t) = \text{Re}[\mathbf{B}(\mathbf{r})e^{-i\omega t}] \quad (4.27)$$

The particle then acquires an induced dipole moment with the same time dependence as the incident fields, and can be written as:

$$\boldsymbol{\mu}(\mathbf{r}, t) = \text{Re}[\boldsymbol{\mu}(\mathbf{r})e^{-i\omega t}] \quad (4.28)$$

Assuming the particle has no static dipole moment of its own, the induced dipole moment, to the first order, is proportional to the electric field at the

particle position \mathbf{r} given as:

$$\boldsymbol{\mu}(\mathbf{r}) = \alpha(\omega)\mathbf{E}(\mathbf{r}) \quad (4.29)$$

where α denotes the polarizability of a particle that satisfies the Clausius-Mossotti relation (for a sphere shape particles)

$$\alpha = 4\pi\epsilon_0 \frac{\epsilon - 1}{\epsilon + 2} a^3 \quad (4.30)$$

Here a is the particle radius and ϵ denotes the complex dielectric permittivity. For particles such as single molecules the projection of $\boldsymbol{\mu}$ along the direction of the magnetic field is the only relevant component. Hence α can be treated simply as a scalar quantity, instead of a tensor of rank 2. The AFM cantilever cannot respond at optical frequencies, such as ω , so the time-averaged Lorentz force in the dipole approximation is [6]

$$\langle \mathbf{F} \rangle = \frac{\alpha'}{2} \nabla \langle |\mathbf{E}|^2 \rangle + \omega \alpha'' \langle \mathbf{E} \times \mathbf{B} \rangle \quad (4.31)$$

where the particle polarizability is separated by the relation $\alpha(\omega) = \alpha'(\omega) + i\alpha''(\omega)$ into α' , the real part, and α'' , the imaginary part. The first term of equation 4.31 is called the gradient force (also described as the dipole force) and the second term is called the scattering force (or also the absorption force). These two forces will be described separately below.

Gradient Force The gradient force stems from variations in the electromagnetic field and is proportional to the real (dispersive) part, α' , of the complex polarizability. The electric field at the particle dipole is due to both the incident electric field as well as the evanescent field from the induced dipole at the tip, and vice versa. We can model the mutual interaction if we consider the tip and molecule as spheres of volume $\frac{4}{3}\pi r^3$ each with their own effective polarizabilities, as in Figure 4.3, and the induced dipole moments become:

$$\boldsymbol{\mu}_t = \alpha_t(\mathbf{E}_0 + \mathbf{E}_p) \quad (4.32)$$

$$\boldsymbol{\mu}_p = \alpha_p(\mathbf{E}_0 + \mathbf{E}_t) \quad (4.33)$$

where \mathbf{E}_0 is the electric field of the incident laser, and $\boldsymbol{\mu}_t$ and $\boldsymbol{\mu}_p$ are the effective dipole moments of the tip and molecule, respectively. \mathbf{E}_t is the evanescent field of the tip, and \mathbf{E}_p is the induced electric field of the particle. The cantilever response is mostly confined to the z direction (normal force component detection) and therefore, only the z components of the tip and molecule dipoles are relevant, $\boldsymbol{\mu}_t = \mu_t \hat{\mathbf{z}}$ and $\boldsymbol{\mu}_p = \mu_p \hat{\mathbf{z}}$ respectively. The evanescent fields of the induced dipoles are given as:

$$\mathbf{E}_i = \frac{1}{4\pi\epsilon_0} \frac{(3\boldsymbol{\mu}_i \cdot \mathbf{r})\mathbf{r} - \boldsymbol{\mu}_i}{r^3} \quad (4.34)$$

where $\mathbf{E}_i = E_{ix}\hat{\mathbf{x}} + E_{iy}\hat{\mathbf{y}} + E_{iz}\hat{\mathbf{z}}$, $r = \sqrt{x^2 + y^2 + z^2}$, and $i = t, p$ respectively. Using equations 4.31 - 4.33 expressions for the z -component of the molecule's induced dipole moment and the electric field at the molecule can be in terms of the tip and particle polarizabilities and incident field in z as:

$$\mu_p = \frac{2z^3\pi a_p\epsilon_0(a_t + 2z^3\pi\epsilon_0)E_{0z}}{4z^6\pi^2\epsilon_0^2 - a_p a_t} \quad (4.35)$$

$$E_p = \frac{a_p(a_t + 2z^3\pi\epsilon_0)E_{0z}}{4z^6\pi^2\epsilon_0^2 - a_p a_t} \quad (4.36)$$

When the relative sizes of the tip and molecule are assumed to be smaller than the gap distance, $z > a_t$ and $z > a_p$, and as the tip and molecule polarizabilities scale with the cube of the radius (equation 4.30) we can also safely assume that $z \gg a_p^3 a_t^3$. With these assumptions equations 4.34 and 4.35 can be simplified and an expression for the z -component can be described simply as:

$$F_g \equiv \langle \mathbf{F}_g \rangle_z \cong -\frac{a_p' a_t'}{2\pi z^4} E_{0z}^2 \quad (4.37)$$

There are few significant items to note from equation 4.37, which is similar to the formula described in Ref. [192]. Firstly, the gradient force is attractive. Secondly, there is a z^{-4} spatial dependence, and F_g is only relevant for very short tip-molecule separations. Lastly, the strength of the force is proportional to the dispersive part of the molecule's polarizability and therefore, information from the molecule's optical properties can be gained from studying this force. It will be helpful to characterize the magnitude of this force by collapsing the gradient force coefficients into the simple parameter β as:

$$\beta = \frac{a_p' a_t'}{2\pi} E_{0z}^2 \quad (4.38)$$

Scattering Force The other optically induced contribution predicted by equation 4.31 is known as the scattering force. The magnitude of this repulsive force is proportional to the dissipative part of the light-particle interaction i.e. the imaginary part of the complex polarizability. The scattering force is described as

$$F_{sc} \equiv \langle \mathbf{F}_{sc} \rangle_z \cong \omega \alpha_t'' \langle \mathbf{E}_0 \times \mathbf{B}_0 \rangle_z \quad (4.39)$$

$\mathbf{B}_0 = B_{0x}\hat{\mathbf{x}} + B_{0y}\hat{\mathbf{y}} + B_{0z}\hat{\mathbf{z}}$. The transverse components of the electric and magnetic field are the only contributors to the force along the tip axis in the z -direction. The dominant component of the incident field is polarized along x , $\mathbf{E}_0 = E_{0x}\hat{\mathbf{x}}$, then the scattering force can be simplified as:

$$\langle \mathbf{F}_{sc} \rangle_z = \frac{2\pi\alpha_t''}{\lambda} E_{0x}^2 \quad (4.40)$$

where λ is the wavelength of the incident beam. Whereas the gradient force scales z^{-4} with tip-sample distance, the scattering force is independent of distance in the nanoscale region of the tip, since the distance-dependence is implicitly contained in the spatial extent of the excitation field E_{0x} . As the excitation field dimension in the focal plane is in the (sub)- μm range, the scattering force is manifested over a different spatial scale than the local gradient force. Therefore, the short range nanoscopic interactions are expected to be governed by the gradient force, while at longer distances the scattering force is dominant. The scattering force is generally repulsive unlike the attractive gradient force, so there may be a specific tip-sample distance where the two optical forces cancel out in magnitude. It should be noted that the image dipole will be generally in phase with the source dipole, giving rise to a significant component of the total tip-sample force (F_{pif}^{AC}) which is unipolar (with nondispersive peak shape), while additional force components acting between tip polarization driven directly by the incident radiation (F_{pif}^{DC}) and the sample polarization may have a dispersive behavior.

The dipole approximation was presented in an analytical approach to reveal the formalization of the existing gradient and the scattering forces under the illumination of linearly polarized light for the tip-sample system. This scenario gets increasingly complex if more precise modeling and different polarizations have to be considered. Hence in the next section, a more accurate yet rigid method is introduced.

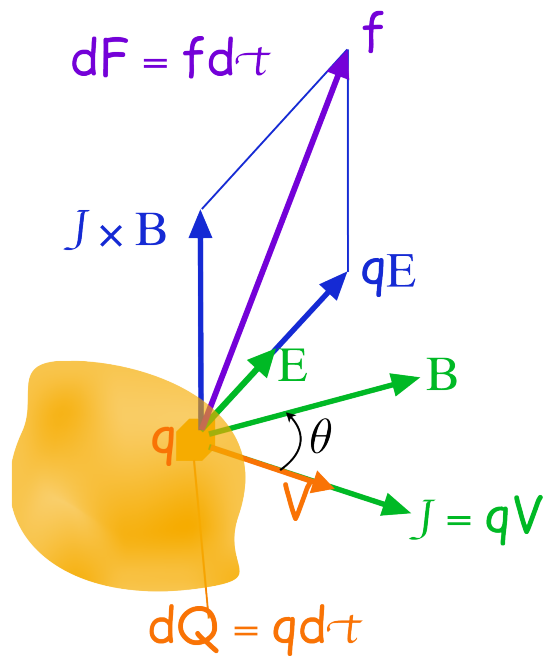


Figure 4.4: Lorentz force (per unit volume) f on a continuous charge distribution (charge density q) in motion. The current density J corresponds to the motion of the charge element dQ in volume element $d\tau$ and varies throughout the continuum. Image is adapted from [193].

Maxwell Stress Tensor

The gradient force in PiFM arises from the wavelength-dependent polarization of the sample. This sample polarization interacts with the cone-shaped, metal-coated tip. In comparison with dipole approximation, here the equation for the optical forces is derived in a different formalism. With Maxwell stress tensor formalism a more precise optical force calculations and modeling can be performed. Let us begin by considering the Lorentz force

$$\mathbf{F}_Q = Q\mathbf{E} + Q\mathbf{v} \times \mathbf{B} \quad (4.41)$$

By extending this equation to the case of an infinitesimal element of a distributed test charge, assuming that a differential volume has an equivalent charge $dQ = qd\tau$, where q is the charge density and $d\tau$ the differential element of volume, and that it moves rigidly along a trajectory such that its instantaneous velocity is \mathbf{v} see Figure 4.4. Thus, we will assume that the force on a differential element of charge is

$$d\mathbf{F} = qd\tau\mathbf{E} + qd\tau\mathbf{v} \times \mathbf{B} \quad (4.42)$$

The force per unit volume of charge is, therefore

$$\mathbf{f} = \frac{d\mathbf{F}}{d\tau} = q\mathbf{E} + q\mathbf{v} \times \mathbf{B} \quad (4.43)$$

Here the “usual” development of the Maxwell stress tensor is presented. Such a development is presented in many textbooks on classical electrodynamics, but we will follow the one by Griffiths [194]. Consider the Lorentz force equation 4.43 and use Maxwell’s equations to write

$$\begin{aligned} \mathbf{f} &= [\epsilon_0 \nabla \cdot \mathbf{E}] \mathbf{E} + \left[\frac{1}{\mu_0} \nabla \times \mathbf{B} - \epsilon_0 \partial_t \mathbf{E} \right] \times \mathbf{B} \\ &= [\epsilon_0 \nabla \cdot \mathbf{E}] \mathbf{E} - \frac{1}{\mu_0} \mathbf{B} \times [\nabla \times \mathbf{B}] - \epsilon_0 \partial_t [\mathbf{E} \times \mathbf{B}] + \epsilon_0 \mathbf{E} \times \partial_t \mathbf{B} \\ &= [\epsilon_0 \nabla \cdot \mathbf{E}] \mathbf{E} - \frac{1}{\mu_0} \mathbf{B} \times [\nabla \times \mathbf{B}] - \epsilon_0 \partial_t [\mathbf{E} \times \mathbf{B}] - \epsilon_0 \mathbf{E} \times [\nabla \times \mathbf{E}] \end{aligned} \quad (4.44)$$

utilizing the well-known vector identity

$$\mathbf{g} \times [\nabla \times \mathbf{g}] = \nabla \left[\frac{g^2}{2} \right] - [\mathbf{g} \cdot \nabla] \mathbf{g} \quad (4.45)$$

and add the zero-valued function $\frac{[\nabla \cdot \mathbf{B}]}{\mu_0}$ to obtain

$$\mathbf{f} = \epsilon_0 [\nabla \cdot \mathbf{E}] \mathbf{E} + \frac{1}{\mu_0} [\nabla \cdot \mathbf{B}] \mathbf{B} - \nabla \left[\frac{\epsilon_0 E^2}{2} + \frac{B^2}{2\mu_0} \right] + \epsilon_0 [\mathbf{E} \cdot \nabla] \mathbf{E} + \frac{1}{\mu_0} [\mathbf{B} \cdot \nabla] \mathbf{B} - \partial_t [\mathbf{E} \times \mathbf{B}] \quad (4.46)$$

Consider the i th component:

$$\begin{aligned} f_i = & \epsilon_0[\partial_j E_j]E_i + \frac{1}{\mu_0}[\partial_j B_j]B_i - \partial_i \left[\frac{\epsilon_0 E^2}{2} + \frac{B^2}{2\mu_0} \right] \\ & + \epsilon_0[E_j \partial_j]E_i + \frac{1}{\mu_0}[B_j \partial_j]B_i - \epsilon_0 \partial_t[\epsilon_{ijk} E_j B_k] \end{aligned} \quad (4.47)$$

which we can rewritten as

$$\begin{aligned} f_i = & \partial_j \left[\epsilon_0 E_i E_j + \frac{1}{\mu_0} B_i B_j - \left(\frac{\epsilon_0 E^2}{2} + \frac{B^2}{2\mu_0} \right) \delta_{ij} \right] - \partial_t[\epsilon_{ijk} E_j B_k] \\ = & \partial_j T_{ij} - \partial_t[\epsilon_{ijk} E_j B_k] \end{aligned} \quad (4.48)$$

T_{ij} are the components of a second order tensor — a 3×3 matrix — called the Maxwell stress tensor:

$$T_{ij} = \epsilon_0 E_i E_j + \frac{1}{\mu_0} B_i B_j - \left[\frac{\epsilon_0 E^2}{2} + \frac{B^2}{2\mu_0} \right] \delta_{ij} \quad (4.49)$$

We see that it is symmetric because $T_{ji} = T_{ij}$ for any choice of the indices i, j . Using dyadic notation, we write this tensor in the form

$$\mathbf{T} = T_{ji} \mathbf{e}_i \mathbf{e}_j \quad (4.50)$$

Therefore, we can rewrite equation 4.47 as

$$\mathbf{f} = \nabla \cdot \mathbf{T} - \partial_t[\mathbf{E} \times \mathbf{B}] \quad (4.51)$$

Equation 4.52 is the force per unit volume on a distributed charge. Focusing on a differential element having volume $d\tau$, we can write the force on it as

$$d\mathbf{f} = \nabla \cdot \mathbf{T} d\tau - \epsilon_0 \partial_t[\mathbf{E} \times \mathbf{B}] d\tau \quad (4.52)$$

Now suppose that we want to find the force on a charge distributed over a region R . We merely integrate the preceding equation over this region, getting

$$\mathbf{F} = \int_R \nabla \cdot \mathbf{T} d\tau - \epsilon_0 \int_R \partial_t[\mathbf{E} \times \mathbf{B}] d\tau \quad (4.53)$$

This expression contains every aspect of electromagnetism and momentum affecting any arbitrary shaped medium. A rigorous numerical calculation of the second-order Maxwell stress tensor with boundary conditions based on the specific geometry of the tip-sample-substrate system gives us a numerical solution of the forces and force gradients arising from optical force interactions. In our case we consider the statistic interactions, hence, we are only dealing with the first part of the equation 4.53.

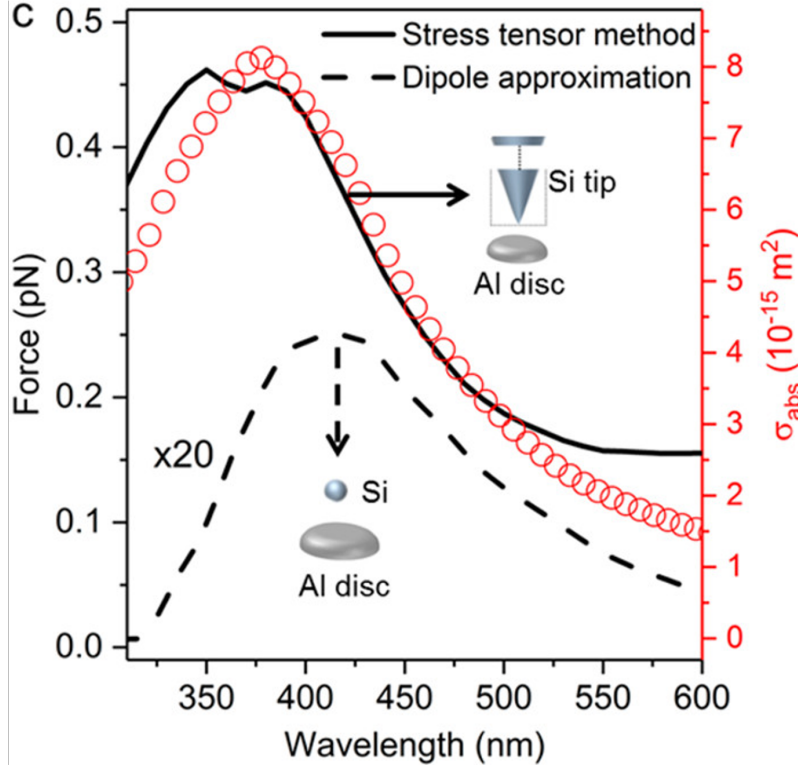


Figure 4.5: The photo-induced force spectrum of a single Al disc calculated using the Maxwell's stress tensor method for a Si tip (solid line), and the same calculated by approximating the tip as a Si sphere (with radius = 20 nm), using the dipole approximation method (dashed line). The absorption cross section (σ_{abs}) calculated for a single Al disc is also plotted for comparison (red markers). For all calculations, the diameter of Al discs (covered by a 3 nm Al_2O_3 layer) = 92 nm. Image is adapted from [34] with permission.

N. J. Halas and coworkers in [34] highlighted the importance of including realistic dimensions of the tip and sample in calculations of photo-induced force interactions (see Figure 4.5). They did this by comparing the optical force spectrum evaluated on a single Al disc using the DDA method with the force spectrum calculated using the stress tensor method. The optical force spectrum evaluated using the stress tensor method tracks the absorption spectrum very well. However, the force spectrum calculated using the dipole approximation method is red-shifted by ~ 50 nm. It is also important to note that the force calculated using the dipole approximation method is highly sensitive to the size of the dipole and can yield arbitrary results depending on the radius of curvature of the dipolar sphere used to evaluate the force [34]. In our case we consider the statistic interactions, hence we are only dealing with the first part of the equation 4.53. In this thesis Comsol Multiphysics was used to calculate optical forces ($\int_{tip} \nabla \cdot \mathbf{T} d\tau$) exerted on the tip in the presence of the sample. The results are displayed and discussed in 4.2.

4.2. Results

One of the benefits of the PiFM is to assist other near-field experiments such as TERS. For a TERS measurement, after adjusting the optical setup, the tip is placed in the laser focus. These positions are fixed to each other then sample is scanned. The critical point of every TERS experiment is to maximize Raman signal amplification. This is directly coupled to a high excitation and collection efficiency. Momentum matching usually compromises the use of an objective with high NA which demands for a setting of the laser focus with nanometer precision in regard to the tip-sample region. However, in this context, the correct lateral tip position with respect to the field distribution in the focal plane and correct focus adjustments along the optical axis is crucial. When focusing linearly polarized light in a transmission configuration onto the sample surface, the correct axial focus position must first be found to focus the laser beam onto the end of the TERS tip. This ensures maximum coupling of the electromagnetic field to the plasmonic structure. In our case, the bottom illumination/collection, the adjustment of the focus of the laser spot is mostly made via a camera image. This assumes that the actual focal plane correlates precisely with the imaging plane on the camera. As a further indication, the response of the Raman signal of the TERS tip itself is used. Since silicon is used as the base substrate of the tips, the first phonon mode of silicon (Si peak at 520 cm^{-1} in the spectrum [195]) can be used to approximately optimize the laser focus on this signal. However, it should be noted here that alignment using the Si signal alone often leads to misalignment since the peak signal increases with overfocusing. For local positioning of the tip within the assumed focus spot, one can either scan the objective over the tip region. For different polarizations, the electric field distribution on the sample surface (Figure 3.8) is well-known. For linear polarization the aim is to position the tip slightly away from the focus spot, into one of the two side lobes polarized in the z -direction. Often only a rough estimate of the optimal tip position for an assumed maximum signal gain can be made. Another challenge compromises the intactness of the tip nanstructure, i.e. optical activity of the tip after initial alignment process.

PiFM offers an optimal solution for the challenges mentioned above. As shown later, PiFM can address the correct axial focus position and the lateral tip position in focus to achieve maximum signal amplification. Moreover, simultaneous checking of the state of the TERS tip is intrinsically given (cf. section 4.2.2). Furthermore, the PiFM technique can be easily integrated into an existing TERS setup. It is non-destructive and guarantees a significant acceleration of the TERS alignment process due to the fast image acquisition. Thus, optimal TERS conditions can be ensured and monitored with PiFM. In the following, after introducing our PiFM setup, some of the applications of

the PiFM technique is discussed.

All the PiFM measurements were conducted with the Vistascope (Molecular Vista, Inc.) which is an AFM-based system. The schematic setup is shown in Figure 4.1. The optical measurements are performed in a transmission configuration. A CW laser (Excelsior, Spectra-Physics) emitting a linearly polarized beam with a wavelength of 532 nm, is expanded, collimated, and then coupled into the AFM system. There it hits the input aperture of a 100x oil immersion objective (Müller Optronic) with a numerical aperture of 1.25 or alternatively a 60x oil immersion objective with numerical aperture of 1.45 (Olympus). The expansion of the laser beam overfills the back aperture of the objective, producing excellent focusing on the sample plane. To control the input polarization, a $\lambda/2$ plate in combination with a polarizer was used. To measure the PiFM signal, the laser beam first hits an acousto-optic modulator (AOM from APE Berlin/Gooch&Housego). An ultrasonic wave is first generated in the AOM, which consists of quartz (operating frequency 110 MHz). This acts as an optical grating on which the input beam is diffracted accordingly. The first diffraction order, and thus the corresponding intensity of the beam are modulated at the frequency f_m . Polarization control includes various optical elements, e.g. a radial polarizer consisting of a liquid crystal (ARCoptix). So linearly polarized light, and particularly azimuthally and radially polarized light can also be generated. After coupling into the AFM and passing the objective, the modulated beam hits the tip. As usual for ordinary AFM imaging, tapping mode was used. The tuning of the cantilever frequencies results in the known first resonance frequency f_0 and higher harmonic oscillations such as the second resonance frequency f_1 . A PiFM signal becomes measurable when the frequency of the modulated laser beam either directly coincides with the second resonance frequency f_1 of the cantilever (direct mode detection $f_m = f_1$) or coincides with one of the sidebands of f_0 (sideband mode detection see section 4.1.1). For sideband modulation f_m can be tuned into the sum and the difference of the two resonance frequencies. In this work, the sum configuration ($f_1 = f_m + f_0$) was used. The photo-induced force is then detected by demodulation using a lock-in amplifier. For imaging the electromagnetic field distributions on the sample surface (see chapter 4.2.1) an objective scan is performed, whereby depending on the polarization state the corresponding field distribution becomes visible as a PiFM signal. If the PiFM signal of the sample need to be examined, an objective scan is first performed to place the tip in the laser focus (= maximum PiFM signal). The tip is then moved over the sample (tip scan) and both the topography and the PiFM signal of the sample are detected simultaneously.

4.2.1. Mapping Electromagnetic Field Distributions at Nanoscale

The incident excitation field plays a vital role for any near-field enhancement measurements. The main goal is to achieve the highest enhancement of the electromagnetic field at the near-field probe by choosing the polarization of the excitation field. Although sometimes the choice of the excitation field is dictated by the different illumination geometries, still it can be engineered by different polarization optics. Bottom illumination/collection setup is used in this work. In this configuration, the highest amplitude of the incident field \mathbf{E}_0 coincides along the tip axis (z -direction, perpendicular to the sample surface), the localized surface plasmon is generated, which acts most strongly along the tip axis. In this case, since the induced dipole moment of the tip, μ_t , also acts in the z -direction, a maximum amplification of the electromagnetic field, or Raman signal, occurs. For example, Figure 4.6 (a) illustrates electromagnetic field distribution on the sample surface and the possible orientation of the induced dipole moment μ_t for an incident beam with linear (left column), radial (middle column), and azimuthal polarization (right column). The left column of Figure 4.6 (a) shows that when linearly polarized light passes through the high NA objective lens, individual polarization components are rotated toward the tip axis [77, 196]. Although a significant fraction of the field components retain their x or y component (x component in our case) due to geometric factors, the relative ratio (x , y versus z components) can be quantitatively determined by choice of NA. Considering the field distribution of this configuration on the sample surface, the z -portion of the field perpendicular to the surface, E_z , does not appear in the center of the intensity distribution. Since the tip axis is aligned parallel to the z -component of the field, to make the best possible use of the optical antenna effect of the tip and proper excitation of the surface plasmons (SPPs) at the its end, ideally tip is placed in one of the two side lobes, as shown in Figure 4.6 (a) left column [154, 197]. One of the photo-induced force microscopy (PiFM) applications is imaging which is essentially non-destructive, fast (acquisition of an image in about 30 s), and yields the possibility to visualize a wide variety of polarization states on the sample surface. For an overview, Figure 4.6(a), (b), and (c) show the respective polarization on the sample surface, normalized transverse, $|E_{x,y} = E_r|^2$, and longitudinal, $|E_z|^2$, field components on the sample surface and the corresponding PiFM image, respectively. The PiFM images were taken in the focal plane with constant tip-to-sample distance, at constant laser power and a wavelength of 532 nm. Commercial gold tips were used because they exhibit a stronger PiFM signal due to their higher polarizability compared to a silicon tip. After approaching the tip to the sample surface (glass substrate), the objective was scanned in a raster pattern over the area of the tip and the re-

spective PiFM image was measured as a function of the incident polarization. The numerical simulation of the electric field distribution of the different polarized beam in the focal plane was performed using the wave optic module of COMSOL Multiphysics which utilizes finite element method (FEM) to solve Maxwell's equations. As described earlier this chapter, PiFM measures the photo-induced force using the polarizability between tip and sample (particle) after excitation with an electromagnetic field. Since the sample in this case is a glass substrate, mirror image of the tip is generated in the substrate, which interacts with the tip. Suppose this tip-substrate system is now illuminated with an external electromagnetic field (see Figure 4.3). In that case, it can be described by two interacting dipoles (section 4.1.2), the dipole of the tip and its mirror image in the substrate with the respective polarizability. Consequently, PiFM measures the force between the induced dipole of the tip, which is proportional to the polarizability of the tip material and its mirror image in the substrate. Thus, this photo-induced dipole-dipole interaction force is correlated with the PiFM signal. This total (photo-induced) force can be caused by both the short-range gradient force and the long-range scattering force, which in turn can be dependent on the influence of the gradient of the incident field [28]. A clear distinction must be made between the (short-range) gradient force and the (total) force gradient.

$$F_g \equiv \langle \mathbf{F}_g \rangle_z \cong -\frac{\beta}{z^4} \quad (4.54)$$

$$\frac{\partial F_{pif}^{AC}}{\partial z} \quad (4.55)$$

The gradient force is part of the electromagnetic interaction, and previously for a linear polarization field is shown as equation 4.54 in which β is achieved as in equation 4.38. This gradient force for other polarizations has different forms. However, the force gradient (or gradient of the force) implies the changes of the force as in equation 4.55 and it can have not only electromagnetic but a thermal origin and it is the basis for sideband coupling measurements as shown in equation 4.24.

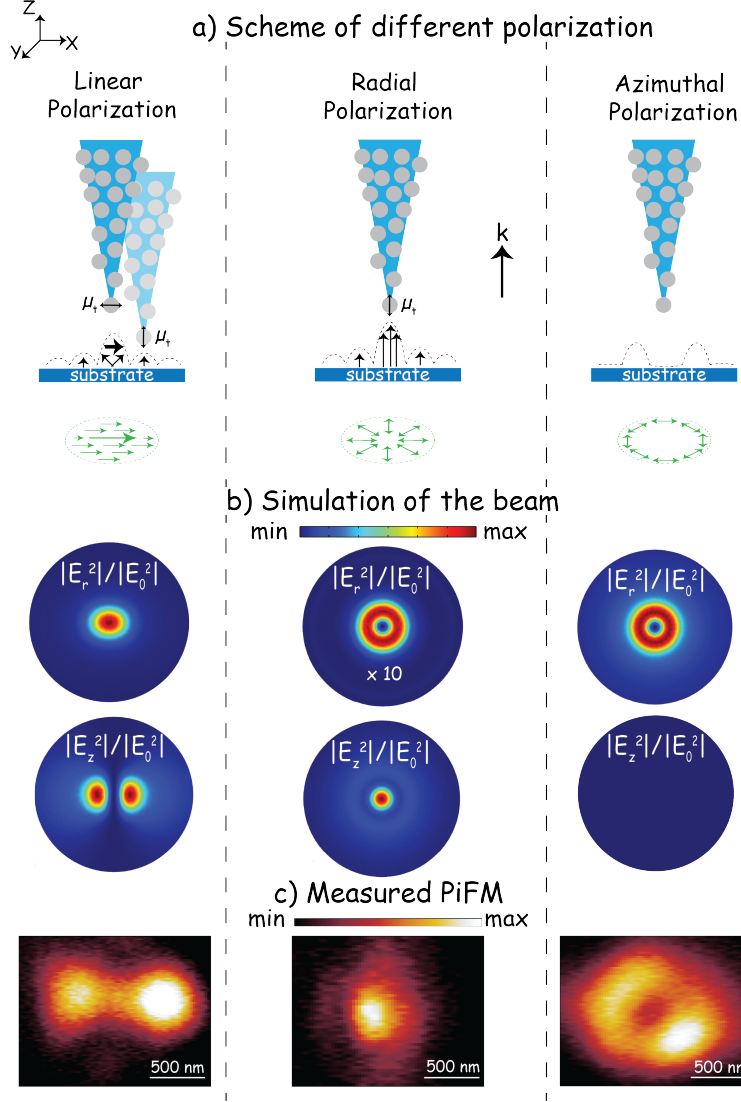


Figure 4.6: PiFM imaging of three different polarization states on the sample surface. a) Field distribution on the sample surface (glass substrate). (Left) Linearly polarized light (x-direction). (Middle) Radially polarized light. (Right) Azimuthally polarized light. b) Numerical simulation of the field distribution of normalized transverse, $|E_{x,y} = E_r|^2$, and longitudinal, $|E_z|^2$, field components on the sample surface. c) PiFM measurement of the three different polarization states and visualization of the field components. PiFM response of an azimuthally polarized beam is specifically discussed in the main text.

Since the measurements in Figure 4.6 are made in the focal plane at constant tip-sample distance, the short-range gradient force contributes to the PiFM signal. In the sideband mode, which is exclusively used in this work, the photo-induced force is separated from all other forces by means of a multi-frequency lock-in amplifier (discussed in section 4.1.1)). Thus, the influence of the long-range scattering force is suppressed in the sideband mode. It should be mentioned that the long-range scattering force can still contribute to a measurable PiFM signal, which will be discussed in more detail in section 4.2.4.

Looking at the PiFM image in Figure 4.6 (c) for linearly polarized light, the two characteristic side lobes due to the axial dipole-dipole alternating effect between tip and sample become visible. Thus, the strong E_z field interaction leads to a measurable force in PiFM. Although, as can be seen in the simulation (Figure 4.6 (b)), the transverse field components have a higher intensity, the PiFM measurement responds to the axial E_z field components. The radial polarization, which is advantageous for TERS, contains exclusively E_z field components (Figure 4.6 (a) and (b) middle column) on the sample surface after focusing. This is confirmed by the dominant axial field components of the PiFM image (Figure 4.6 (c)). Since the establishment and assurance of radial polarization is more demanding in terms of alignment, PiFM provides a reliable method to ensure the correct polarization state on the sample surface. Although in Figure 4.6 (c) left and middle columns only the prominent E_z field components are measured, PiFM can also be used to measure an image contrast for azimuthally polarized light, even though all field components lie in the xy plane and theoretically no z components of the electric field are present on the surface (Figure 4.6 right column (a) and (b)). This phenomena needs to be clarified.

PiFM for an azimuthally polarized beam. Authors in [115] analytically show that for azimuthally polarized radiation, the force exerted on the tip can be written as

$$F_g \equiv \langle \mathbf{F}_g \rangle \propto |\alpha_{tip,t} E_t|^2 \quad (4.56)$$

here E_t denotes the transverse components of the incident field and $\alpha_{tip,t}$ expresses the transverse components of the tip's polarization. So as it can be seen the experimental results in Figure 4.6 right column (c), are fitting with the analytical formula and the optical force is proportional to the transverse components of the incident beam which in our case is $E_t = E_r$.

In this section, it was shown that PiFM can visualize the optical near fields and the distributions of the electric field components within a strongly focused laser beam with linear, radial, and azimuthal polarization by measuring the optical force between the tip and the mirror image of the dipole in the glass substrate. Compared to other near-field optical methods, such as s-SNOM, in PiFM both excitation and detection are performed directly from the optical

near-field. Thus, PiFM provides background-free imaging of the optical near-field and the corresponding field components and distributions on the sample surface, which is limited in sensitivity only by the performance of the AFM.

4.2.2. Characterization of the plasmonic tips

As already described in the previous section, PiFM is particularly well suited for visualizing the polarization state on the sample. In the course of this work, another decisive advantage of the PiFM technique is developed. This addresses the most important and, at the same time most, sensitive part of a TERS measurement; the tip. A typical TERS tip is covered with many nanoparticles, ideally a single nanoparticle sitting at the tip end. However, due to the manufacturing process, the integrity and correct arrangement of the nanoparticle bending at the tip end cannot be guaranteed. One SEM image is typically used to control the manufacturing process for each set of produced tips. However, carbon deposition during the SEM measurement can cause the examined tip to be unusable for TERS measurements. Assuming a proper arrangement of the frontmost nanoparticle at the tip's end, it is still not excluded from getting damaged during the adjustment of the TERS measurement, e.g., approaching the tip too hard to the sample surface. Consequently, the crucial part contributing to the required field enhancement in TERS is lost. Experimentally, a tip that is deficient due to the manufacturing process or damaged due to adjustment is noticeable by a low or missing Raman signal. In addition to the time aspect of replacing the tip again, it is impossible to predict whether an ideal TERS tip is present before any TERS experiment. Thus, PiFM is used to address this issue. For this purpose, a series of freshly prepared TERS tips from different production sets were each characterized before a TERS experiment using PiFM at constant laser power. The used laser wavelength of 532 nm ensures efficient plasmonic excitation of the tip. After installing the tip, it was approached to the sample surface with the smallest possible oscillation amplitude (low set point) to minimize the tip-sample interaction. Since the objective, with the focused laser beam, is scanned over the tip region, the tip remains intact. Figure 4.7 shows four PiFM images of the TERS tips, as well as the corresponding SEM images of the tips after the PiFM measurement.

Looking at the PiFM signal in Figure 4.7 (a), the well-defined characteristic side lobes can be seen, representing the E_z field component. In the SEM image (Figure 4.7 (a)), it is clear that this is an ideal TERS tip, with a single nanoparticle sitting at the tip's end. Comparing PiFM signals in Figure 4.7 (a) and (b), it can be seen that due to a large number of nanoparticles at the tip end (cluster), a very strong PiFM signal is measured. Similar behavior is observed on silicon tips covered with gold nanoparticles [198]. Compared to

the tips used here, sometimes the gold particles form a closed film around the tip. This leads to an uncontrollable anisotropy of the induced dipole at the tip end, revealing itself in distorted PiFM images [198]. In contrast, Figure 4.7 (c) shows a TERS tip with no nanoparticle at the tip end and where only the bare silicon tip functions as the tip end. In this case, the tip-sample interaction is dominated by the silicon tip. It is reflected in a very weak PiFM signal since the detection of the photo-induced force depends on a sufficiently high electromagnetic response of the tip. Finally, Figure 4.7 (d) shows a TERS tip after a standard TERS measurement. The tip was approached and retracted several times to the sample, adjusted several times to its maximum silicon Raman signal, simultaneously measured the AFM topography of the sample under investigation. Afterward, a PiFM measurement is performed. The signs of use are clearly reflected in the PiFM signal, and the damage of the tip can be confirmed from the SEM image.

In summary, this section has shown that the PiFM technique is very well suited for the before/after characterization of the near-field probe such as TERS tips. Besides saving time, a first qualitative impression of the TERS tip can be obtained. Since a qualitative characterization by SEM is intrinsically prohibited, PiFM provides a reliable result on the quality of the tips and the presence of the crucial frontmost nanoparticle at the tip end. However, it should be mentioned that PiFM measurements on other TERS tip systems, consisting of a metallic AFM tip covered with plasmonic nanoparticles, might be different. In the case of no nanoparticle at the tip's end, the metallic tip can contribute to a quantitatively higher PiFM signal simply because of its higher polarizability. In the case of the TERS tips used in our group (silicon AFM tip with silver nanoparticles), however, a valid statement can be made about the suitability of the tip for a near-field experiment.

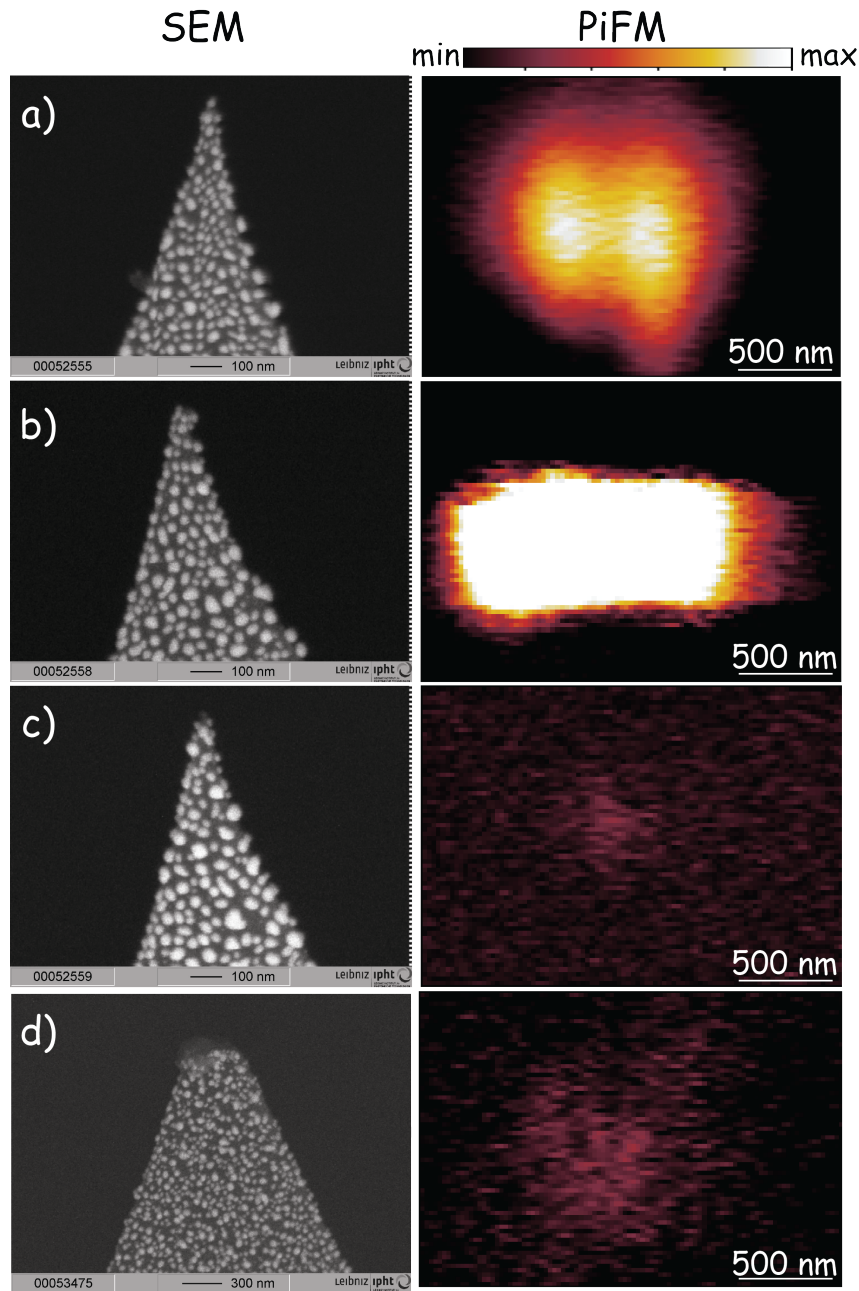


Figure 4.7: SEM images of four different TERS tips (left) with their corresponding PiFM signal (right). In (a,b,c) the SEM images were taken before the PiFM experiment to investigate the influence of the freshly made TERS tips on the PiFM signal. In (a) the PiFM image of an ideal TERS tip is shown. Similarly, (b) shows the response of a nanoparticle cluster at the tip's end. (c) represents the effect of the absence of the front-most nanoparticle at tip and a nearly absent PiFM signal. In d), a TERS tip is seen after a TERS measurement, and its wear is also reflected in the nearly absent PiFM signal.

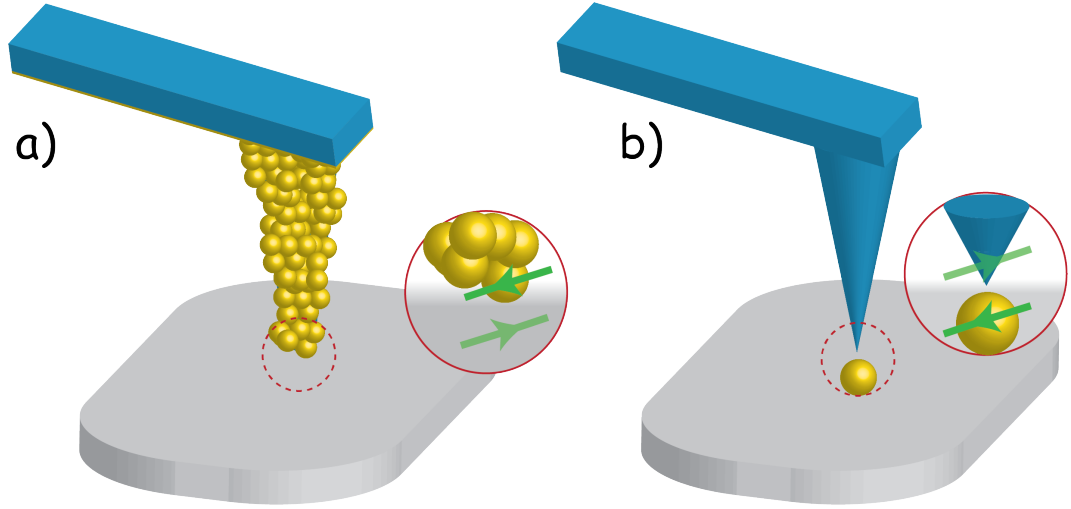


Figure 4.8: Schematic comparison of a) an Au coated Si and b) bare Si tip showing advantages of taking PiFM signal with Si tip due to the sharper end radius and more symmetric shape. The small Au grains at the tip's end increase the tip's radius and also results in different lateral polarizabilities of the induced dipole in different directions [198].

4.2.3. High Resolution PiFM Imaging of Plasmonic Nanostructures

Besides the possibility to visualize different polarization states on the sample surface, the PiFM is suitable to uncover the plasmonic nanostructure's behavior. As it is well known, the slightest deviations in the morphology of these structures significantly influence the local near-field optical interaction. Hence simultaneous topography and near-field imaging of such materials are highly advantageous. Numerous approaches have been investigated to enable the synchronous imaging of topography and the electromagnetic near-field response of nanoscale materials with high resolution. Although many applications of plasmonic structures rely on their near-field interactions, in experimental studies of these systems, far-field spectroscopy is often used together with near-field modeling to characterize their optical response. As shown in section 3.2.4, spectral responses in the far and near fields may differ significantly. Consequently, investigating the near-field spectral nature of plasmonic materials together with high-resolution topography mapping is tedious. PiFM allows indirect visualization of the near-field response of nanoscale materials by probing photo-induced changes in chemical, physical, or spectroscopic signatures through a nanoscale tip besides their topography image [198].

Detecting the photo-induced force in PiFM depends on a particular tip

with an adequate electromagnetic response. As mentioned, the PiFM measures the force between the induced dipole at the tip, proportional to its polarizability, and its mirror image on the substrate. To obtain a detectable photo-induced force signal in a conventional PiFM, Au/Ag-coated tips are used. Due to higher polarizability of the Au/Ag-coated tips than that of a Si tip and produces a stronger dipole at the tip, signal enhances. Nevertheless, in some cases, coating a Si tip with Au/Ag deteriorates the symmetrical shape of the tip due to randomly arranged Au/Ag grains at the end of the tip [115]. Consequently, it might lead to an uncontrollable anisotropy of the induced dipole at the end of the tip, see Figure 4.8 a), which in turn leads to distorted beam profiling and PiFM images [115]. But when an investigation of the plasmonic samples is desired, are plasmonic tips still needed? Can a bare Si tip still detect the PiFM signal of Au/Ag-NPs placed on the substrate? see Figure 4.8 b). From the theoretical point of view, the Au/Ag NPs on the glass can somehow fulfill the Au/Ag grain at the end of the tip in the conventional PiFM technique. The SPPs of these NPs on the glass substrate can create sufficient optical force so that even a bare Si tip can map a PiFM image. Authors in [33] have investigated PiFM response of Au NPs using Au coated tips. Here in this part, we will examine the ability and quality of mapping the near-field response of these NPs using PiFM with pure Si tips. In this condition if PiFM can still perform, it might be very beneficial because the near-field responses mapped is almost purely related to the sample with only a minor distortion from the tip. Here we used the same PiFM scheme as before in section 4.2. But the objective lens has been replaced with a higher numerical aperture (Olympus PlanApo 60x/1.45 Oil TIRFM). The power of the incident beam at the sample is $\sim 900 \mu\text{W}$. The PiFM works in non-contact mode. We used Si cantilevers (Tap300Al-G from Budget Sensors) with first and second cantilever resonances at 295 kHz and 1860 kHz, respectively. The cantilever is driven at its first mechanical resonance, and the PiFM signal is detected at the second. We map the near-field distribution of Au NPs excited with LP light. Au NPs with ~ 100 nm radius were dispersed on a glass slide using piezo-dispensing technique [199]. The PiFM signal (measured in mV) is proportional to the cantilever's oscillation amplitude at its second mechanical resonance, which in turn reflects the photo-induced longitudinal force exerted on the tip.

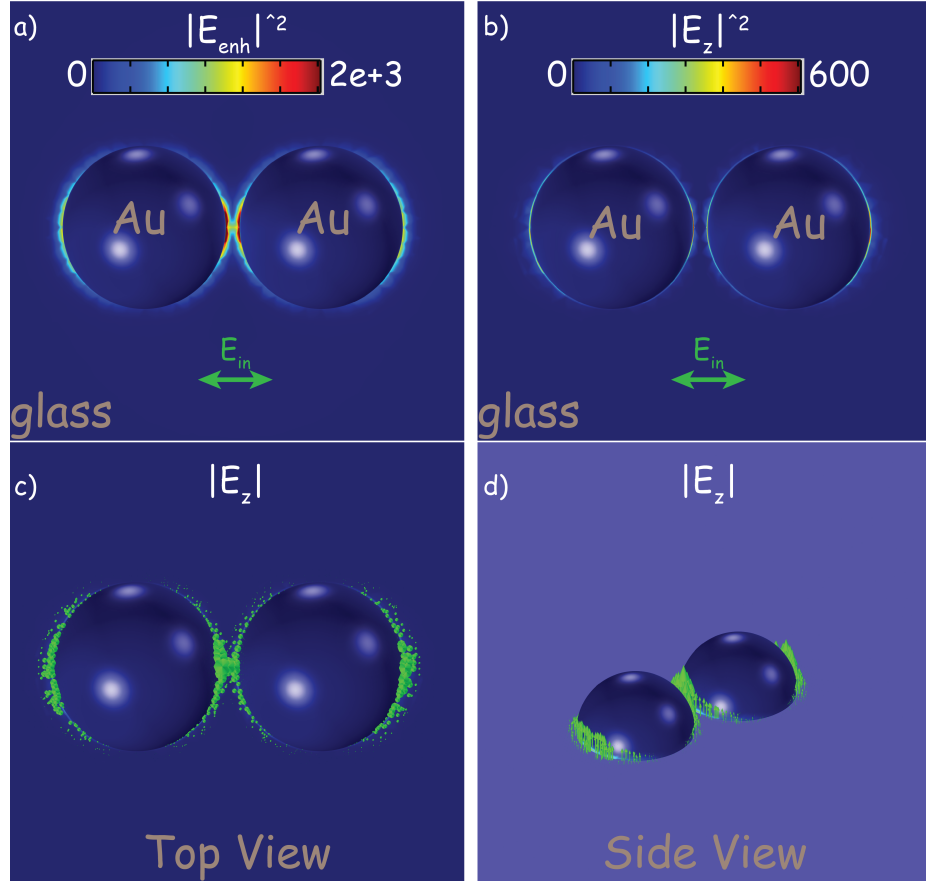


Figure 4.9: FEM simulation of a system of dimer of 90 nm radius of Au NPs with 20 nm gap size. a) $|\mathbf{E}_{enh}|^2$ and b) $|\mathbf{E}_z|^2$ distribution around Au NPs represented from top view. z components of enhanced electric field of dimer can be seen from top view c) and side view d). Polarization of the incident light, \mathbf{E}_{in} , is shown with green arrow in a) and b).

Before performing the PiFM experiment, simulation of simple cases were done. Figure 4.9 shows the electric field distribution around the dimer of 90 nm radius Au NPs with 20 nm gap size lying on a glass substrate in bottom illumination/collection configuration. In Figure 4.9 a) electric field enhancement, $|\mathbf{E}_{enh}|^2$ is shown from top view. It shows that strong field enhancement occurs in the boundary between noble metal and high refractive index material here Au and glass, respectively. As discussed in previous chapters, this is a condition for the emergence of the surface plasmons in noble metal NPs. It can also be seen that in the gap cavity between NPs, the field enhancement is stronger due to coupling between dipole moments of NPs. The strength of this coupling depends on the gap distance and the polarization of the incident light. Even though most of the components of \mathbf{E}_{enh} are parallel to the polarization of incident beam (here x which is parallel to the dimer axis and is shown as \mathbf{E}_{in}) Figure 4.9 b) shows that there are a noticeable z components perpendicular to the surface. Abstract of these electric field vector components is shown as, $|\mathbf{E}_z|$, from top and side view in Figure 4.9 c) and d), respectively. These electric field components also are more pronounced in the edges of the NPs.

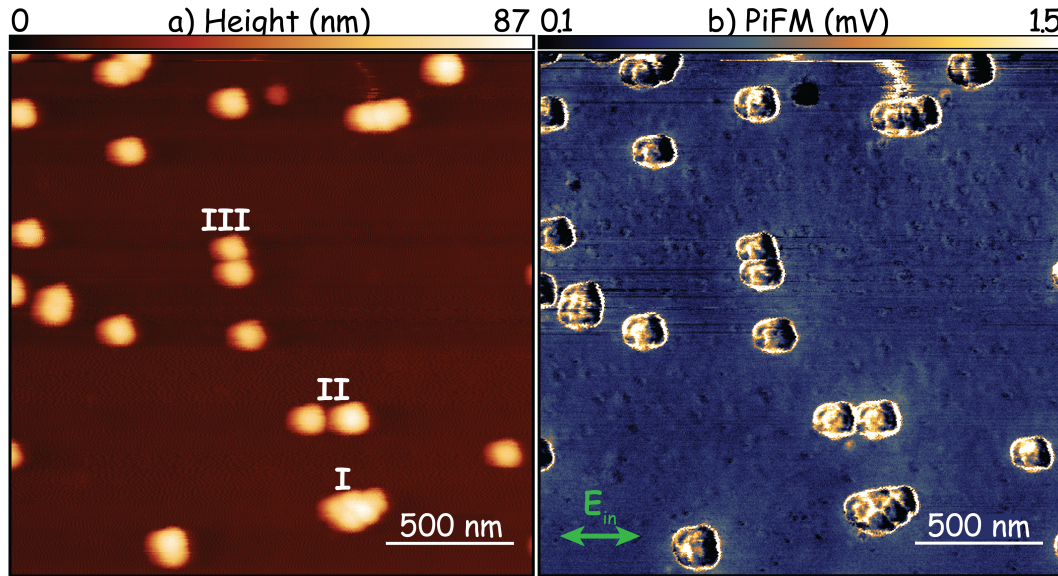


Figure 4.10: Simultaneous a) AFM and b) PiFM imaging of Au NPs. Polarization of the incident light, \mathbf{E}_{in} , is shown with green arrow.

Figure 4.10 shows simultaneous a) AFM and b) PiFM experiments of Au NPs under linearly polarized beam illumination with polarization indicated as \mathbf{E}_{in} . The most apparent observation is that the PiFM image has a much higher resolution than the topography image. The boundaries and edges of the NPs are much better resolved in PiFM image. Specifically, the PiFM image reveals that cluster I consists of 5 NPs, which cannot be revealed in topography

images. Moreover, the PiFM response of dimers II and III are polarization-dependent. In our case, the polarization direction is perfectly aligned with the axis of dimer II, whereas dimer III is perpendicular, resulting in a weaker PiFM signal. Another clear pattern is that, in PiFM image, the edge of NPs with a boundary with the glass substrate, the PiFM signal is much substantial. It is in correlation with the simulation results shown in Figure 4.9. In the 4.1.2 we showed that in PiFM measurement short-range gradient force is dominant and for linearly polarized beam illumination it is proportional to $|E_z|^2$ as shown in equation 4.38. Therefore from the simulations results, since in the edge of NPs $|E_z|$ is stronger, PiFM signal would increase accordingly. In the following part, we will investigate this correlation in further detail. Unquestionably, there are differences between the simulation and the experiment. In the PiFM image, not only the edges but also some parts of the center surface of the NPs are showing PiFM signal. This might come from the asymmetry of the NPs (they are not necessarily perfect smooth half-sphere similar to simulation) with roughness or even atomic-scale protrusions causing a solid localized field enhancement in those spots.

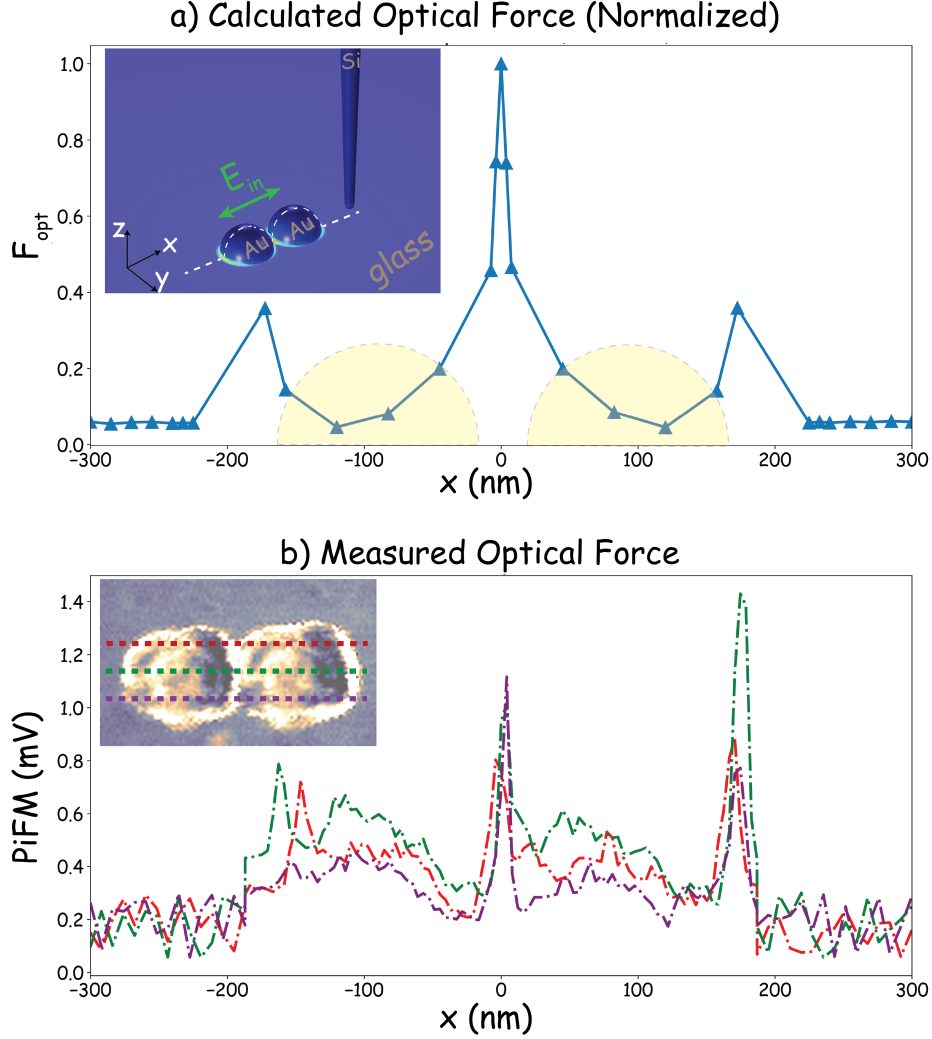


Figure 4.11: a) calculated and b) measured photo-induced force on a Si tip from dimer of Au NPs.

To investigate the photo-induced force of a dimer system, we specifically focus on dimer II and compare our experimental data with FEM simulation results. Although the field distribution around the NPs without the tip (Figure 4.9) presents some insight about the photo-induced force, the field distribution alone is not enough to interpret the PiFM data because of the following reasons. First, the force exerted on the tip is proportional to both the field (here short-range gradient force in equation 4.54) and the field gradient (for sideband detection scheme, we have shown this in 4.1.1 and equation 4.55). Therefore, if at some points the field varies rapidly along the z -axis, the force value might be high even if the absolute value of the field might not be as high [198]. Secondly, the presence of the tip close to the dimer can perturb the field

distribution because of the comparable dimensions of the Si probe and the Au dimer. In this case, the dipole-dipole approximation might not be very accurate, and realistic geometries of the tip should be taken into account. In the FEM simulation, the same dimer system as in Figure 4.9 is used (a tightly focused Gaussian beam with 532 nm wavelength illuminated two Au half-spheres with a radius of 90 nm and a gap of 20 nm on top of a glass substrate). Additionally, this time, the Si tip with a long cone with a radius of curvature of 10 nm is also modeled. To calculate the forces on the tip Maxwell stress tensor method is used. The length of the tip was 1 μm . As mentioned in 4.1.2, it is shown that to obtain more accurate force values, more extended tips around 4.5 μm are needed [33]. However, we considered a shorter tip since it is sufficient enough to calculate the trends of optical force on the tip and compare the force values at the gap and on the edges to those on top of the half-spheres. For the incident polarization parallel along the dimer axis, Figure 4.11 (a) and (b) compare the normalized calculated longitudinal optical force (along the z-axis) with the PiFM signal taken experimentally on a line scan shown inside of each graph, respectively. In FEM simulation, we assumed a 1 nm gap between the tip and the dimer as it scans over the line shown inside of Figure 4.11 (a). A very good agreement in terms of the presence of the peak in the gap as well as peaks at the edges can be seen in both figures.

Finally, the extraordinary resolution of PiFM imaging is pointed out. As shown in Figure 4.10, the PiFM image appears much more detailed than the AFM topography image. While the two NPs appear spherical in the lower AFM image area, the facets and edges of the particles are much more prominent in the PiFM image. Particles are much more detailed in the PiFM image. Due to the finite dimension of the tip, there is a broadening of the lateral particle dimensions in the topography image caused by the convolution of the tip with the sample geometry. Furthermore, the facets to be resolved on the particles are smaller than the tip radius of the used probe (radius = 10 nm), so that they cannot be resolved in the topography image. Thus, the resulting profile of the sample of an AFM measurement depends on the sample dimension and tip geometry. In addition to the PiFM overview, Figure 4.12 shows PiFM line profiles of Au NPs. Based on the profile, the individual facets below 10 nm become visible and can be resolved. In this case, the resolution was determined from the full width at half maximum (FWHM) of the signal peak in the PiFM line profile.

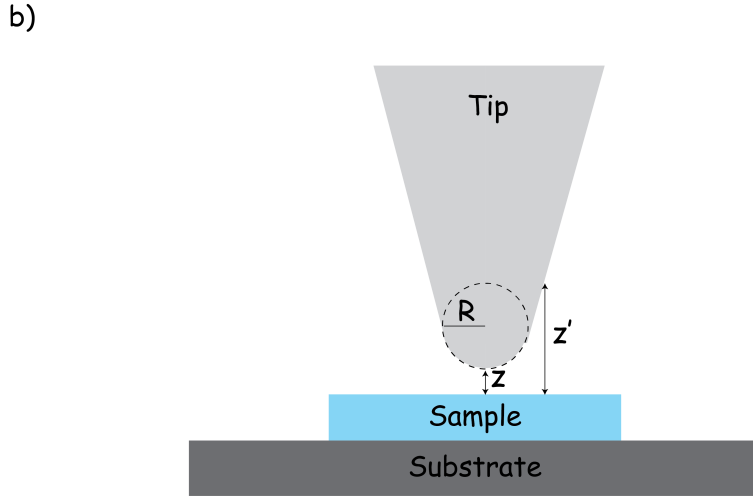
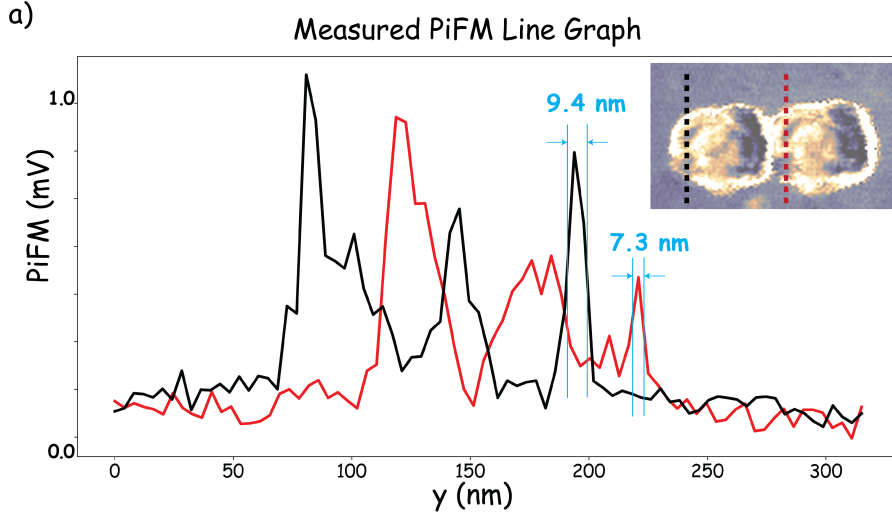


Figure 4.12: Line scan profile across the Au NPs in PiFM. Resolution below 10 nm is well resolved. b) Definition of parameters that determine the spatial resolution of PiFM. z and z' are two different points of the tip affecting on the measurement at the same time.

Generally, the spatial resolution of any scanning probe microscopy technique is determined by three main criteria: effective volumes of the tip and sample that are interacting, the sensitivity of the detection technique, and the background signal that will determine the signal-to-noise ratio. Typically, the effective volumes of the tip and sample that are interacting will depend on tip radius (R), the gap spacing between the tip and the sample (z), and the tip-sample interaction as a function of z (here $F_{int}(z)$ and $F_{opt}(z)$). These parameters, along with the field enhancements (that result from the shape and coating of the tip, and the nature of substrate), will determine the lower limit of the spatial resolution. As mentioned earlier in 4.1.1 there are two types of

forces acting on the tip during the simultaneous measurement of AFM and PiFM (see Figure 4.10). The mechanical tip-sample interaction force F_{int} and the photo-induced optical force F_{opt} . The mechanical tip-sample interaction force can be described by attractive conservative van der Waals forces:

$$F_{int}(z) = -\frac{HR}{6z^2} \quad (4.57)$$

where H is the Hamaker constant, R is the tip radius, and z is the distance between the tip's apex and the sample surface, while the photo-induced optical force for linearly polarized beam reads as:

$$F_{opt}(z) = -\frac{a'_p a'_t}{2\pi z^4} E_{0z}^2 + \frac{2\pi \alpha_t''}{\lambda} E_{0x}^2 \quad (4.58)$$

where E_{0z} is the z component of the incident field, and α_t and α_s denote the complex polarizability of tip and sample, respectively. From the above equations, it can be seen that F_{opt} has a z^{-4} dependence making it a highly localized force that can be exploited for very high lateral resolution. The z^{-4} dependence of PiFM falls-off extremely fast with increasing z . The consequence of the fast fall-off is that, referring to Figure 4.12 (b), $F_{opt}(z')$ will be much smaller than $F_{opt}(z)$ while $F_{int}(z')$ and $F_{int}(z)$ are less different. Thus in PiFM experiments, the interaction volume of tip and sample is much smaller (on the order of the tip radius) than in AFM experiments. If we go one step further, another reason for the enhanced spatial resolution in PiFM arises from the fact that the tip's electric-field enhancement profile is much smaller than the physical tip profile. When the illuminated tip is very close to the sample surface, in the created cavity, an enhanced field appears. FWHM of this localized field is much smaller than the tip's radius. In PiFM, the measured photo-induced signal originates from this localized field enhancement. This scenario is even more pronounced for edges and atomic-scale protrusions associated with NPs of the tip or the sample, which can cause an even narrower yet stronger field enhancement [125].

This example shows the advantages of PiFM to study the heterogeneity in local field distributions for nominally equal nanostructures fabricated by a precision tool such as e^- beam lithography. As such, PiFM will be an acceptable addition to the toolbox of nanoscale characterization methods and will find useful applications for the characterization of precisely manufactured nanostructures, surface-enhanced Raman scattering (SERS) substrates, and photocatalysis.

4.2.4. Focusing effect on PiFM

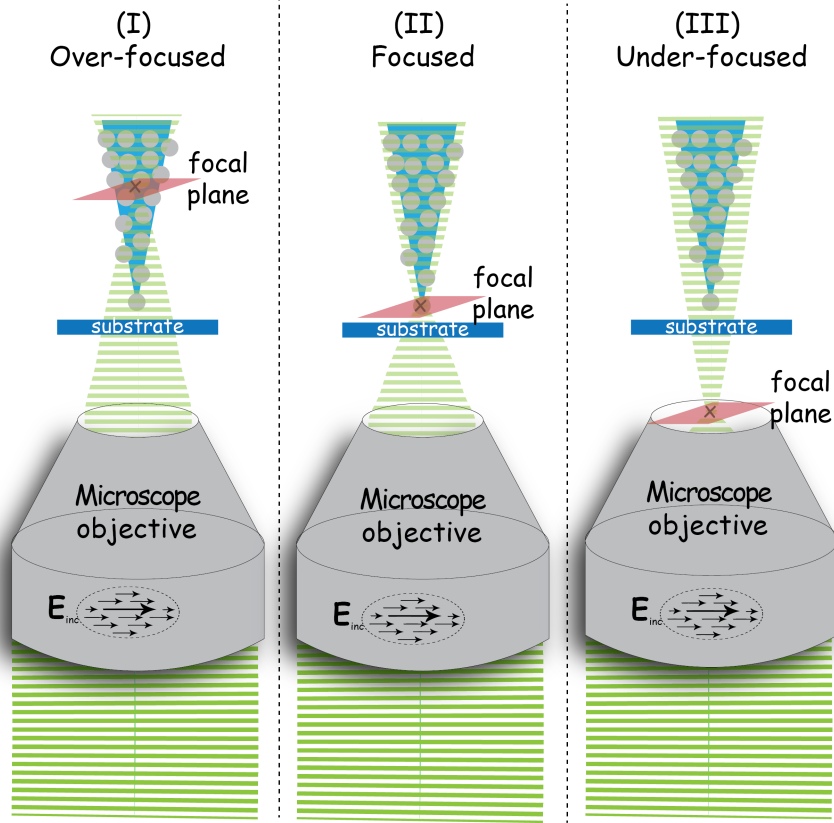


Figure 4.13: Schematic representation of PiFM measurement for overfocused (+700 nm, I), focus (0 nm, II) and underfocused (-700 nm, III) conditions.

So far, for all previous discussions and applications of PiFM, the laser beam was focused on the front-most part of the tip. In this section, we will focus more on the fundamental features of PiFM. Investigations of the impact of different focusing positions on the PiFM image formation and contrast is the primary goal of this section. Explicitly, we are focusing the laser on three separate cases. In the first case, the laser beam is focused +700 nm above the sample stage, so the beam is overfocused and schematically shown in Figure 4.13 (I). The second case complies with the regular PiFM configuration, and the beam is focused on the front-most part of the tip (see Figure 4.13 (II)). The last case considers beam to be focused -700 nm below the sample stage, i.e. laser is underfocused (see Figure 4.13 (III)).

At first, we show the optical force distribution at different focus positions of a tightly focused Gaussian laser beam due to the interaction between a TERS

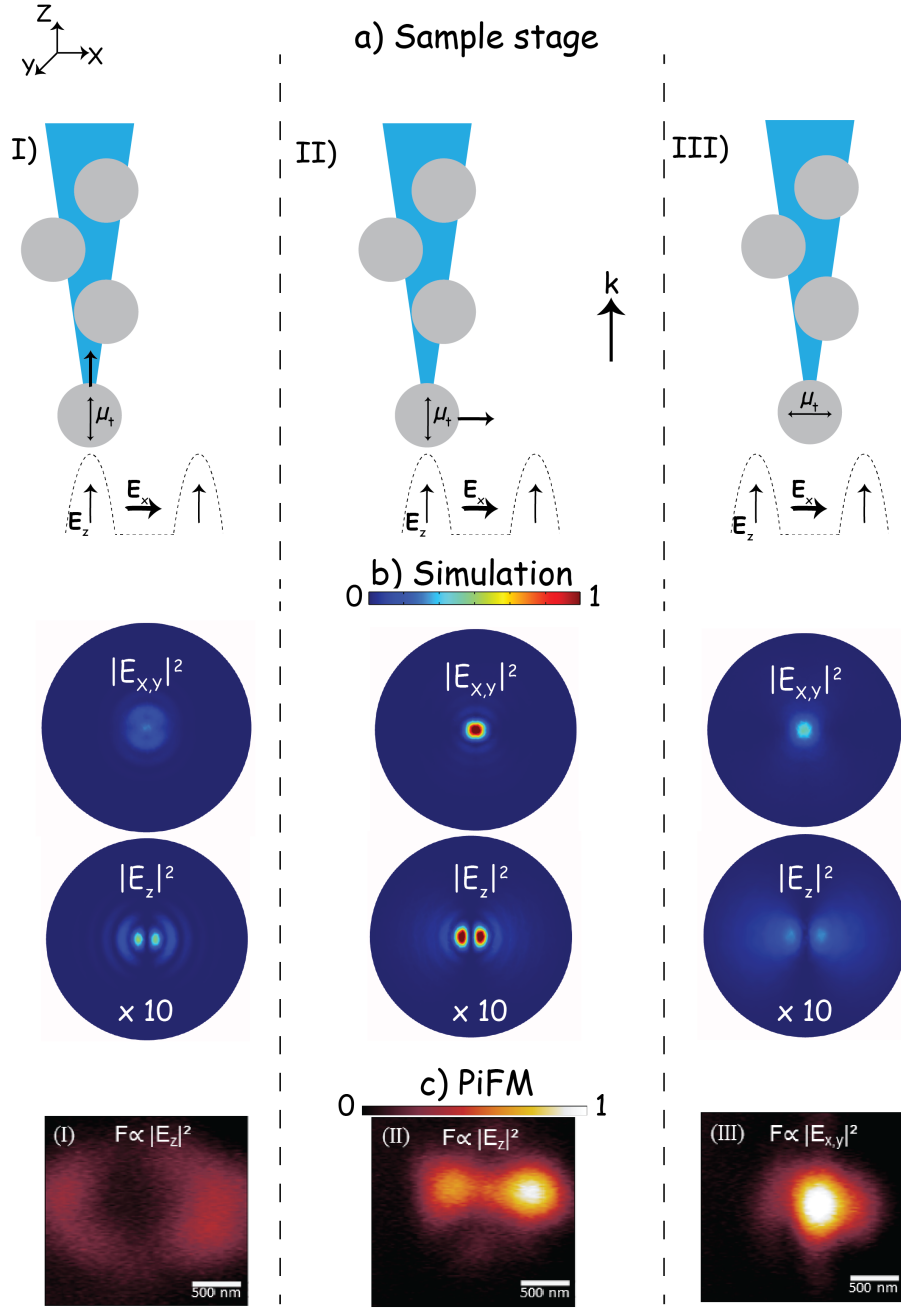


Figure 4.14: PiFM mapping of the electrical field distribution of a laser focus using a TERS tip for overfocused (+700 nm, I), focus (0 nm, II) and underfocused (-700 nm, III) conditions. (a) High NA focused Gaussian beam, generating a spatially dependent field distribution of x-polarization (transversal, E_x) and z-polarization (axial, E_z) at the sample surface. (b) Simulation results considering $E_{x,y}$ - and E_z -field components at the respective focus position (I-III). (c) Respecting experimental PiFM data for overfocused (I), focus (II) and underfocused (III) condition. Image is reproduced from [200] with permission.

tip and its image dipole induced on a cleaned glass coverslip (Figure 4.14). As we know by now, this optical force image directly measures the electromagnetic field distribution at the sample stage, with the TERS tip acting as a perfect dipole antenna. The input laser beam was polarized along the x-axis, and the focal spot was raster scanned to obtain the optical force image. We already mentioned that a PiFM experiment probes the axial (z-direction) dipole-dipole interaction in the tip-sample junction. It would be very useful to consider the theoretical simulations (Figure 4.14 (b)) and comparing them to the detected forces in the experiment. Similar to previous sections, the electromagnetic field distribution of a tightly focused Gaussian laser beam was calculated at three focal positions using Finite-Element-Method (FEM) implemented in Comsol Multiphysics software to solve Maxwell's equation for stationary problems. We assume that the incoming electrical field (E_0) is linearly polarized along the x-axis. The incident light is focused with a high NA (NA = 1.25) objective on a glass substrate without a tip. The subsequent field distributions for the overfocused and underfocused conditions have been represented. Apart from simple geometry factors, the difference is based on the fact that the fields are diverging or converging depending on the (de)focusing. Therefore, depending on the tip-focus distance, different forces are present over a different spatial scale and contribute to the PiFM signal.

$$F_{opt} = F_{gr} + F_{sc} = -\frac{a'_p a'_t}{2\pi z^4} E_{0z}^2 + \frac{2\pi \alpha''_t}{\lambda} E_{0x}^2 \quad (4.59)$$

$$A_s \propto \frac{\partial F_{opt}}{\partial z} \quad (4.60)$$

Here we present all necessary equations playing role in our PiFM measurement. Equation 4.59 shows the total optical forces including gradient force (F_{gr}) and scattering force (F_{sc}) in the dipole-dipole approximation (DDA). In which α_p represents the polarizability of the sample (here is glass substrate) and α_t is showing the polarizability of the probe (here, TERS tip). Equation 4.60 shows the amplitude of the PiFM signal in sideband detection, utilized here. By considering equation 4.60 we can see that in sideband detection, gradients of the forces are measured. Here we are focusing on optical forces only (F_{opt}). DDA and equation 4.59 suggest that long-range scattering forces (F_{sc}) are intrinsically suppressed during sideband detection. The goal of this section is to see if this is always the case. In other words, here we investigate the measured gradients of the overall forces in the different focal positions.

The laser wavelength, here 532 nm, is optically resonant with the used plasmonically active TERS tip, resulting in a spatial variation of the photo-induced force at the focus position and following the shape of the z-component of the focal field, as already reported in previous sections. Clearly, the strongest forces (z-components) are observed at the off-axis locations where the E_z is

maximized, forming double lobes associated with the axial field component being much stronger than the transversal ((II) in Figure 4.14 (c)). The same principle also applies for the overfocused condition ((I) in Figure 4.14 (c)), but with a weaker PiFM signal that is spatially broadened. For the underfocused condition ((III) in Figure 4.14 (c)), the experimental PiFM signal becomes a round spot, which is initially surprising considering the involved z -components of the field. The effect can be understood by considering the theoretical simulations (Figure 4.14 (b)) and comparing them to the detected forces in the experiment [200]. For the focus and overfocused condition (I and II in Figure 4.14 (c)), measured PiFM signal is only sensitive to the axial field distribution. Since E_z leads to an induced dipole moment of the tip (μ_t) in z -direction (Figure 4.14 (a)), the short-range gradient force F_{gr} is the dominating force at this tip-focus distance, giving rise to the image contrast. In the underfocused condition ((III) in Figure 4.14 (c)) with a larger tip-focus distance, the induced dipole moment of the tip changes its orientation according to the polarization (x,y -field components) of the incoming field. Thus, the long-range scattering force F_{sc} is dominating and leads to a measurable gradient of the overall photo-induced force in PiFM, observed as a round spot. In other words, the round spot originates from the strong gradient of the overall photo-induced force (which is measurable in sideband mode) generated from the high $E_{x,y}$ in the underfocused case. Hence, depending on the initial focus position, either the gradient or the scattering force is dominating and leads to a PiFM image contrast. Next, we experimentally investigated TERS on molybdenum disulfide (MoS_2) as an ideally flat surface to confirm these results [200].

The Raman spectrum reveals the two characteristic modes for a MoS_2 monolayer at 382 and 400 cm^{-1} . The more enhanced peak in the TERS spectrum at 400 cm^{-1} refers to the A_{1g} out-of-plane vibration of the sulfur atoms in MoS_2 , whereas the weaker peak at 382 cm^{-1} is assigned to the E_{2g}^1 in-plane vibration of the two sulfur atoms with respect to the molybdenum atom in the sheet [201,202]. It has been shown that in TERS measurement, since the tip is set into one of the two side lobes, z -polarization along the tip axis is obtained. Thus, the out-of-plane mode A_{1g} mode is strongly enhanced [200,203]. The combined PiFM and TERS experiments on a MoS_2 flake transferred on glass is performed to prove the results of pure PiFM experiment and the simulations shown in Figure 4.14.

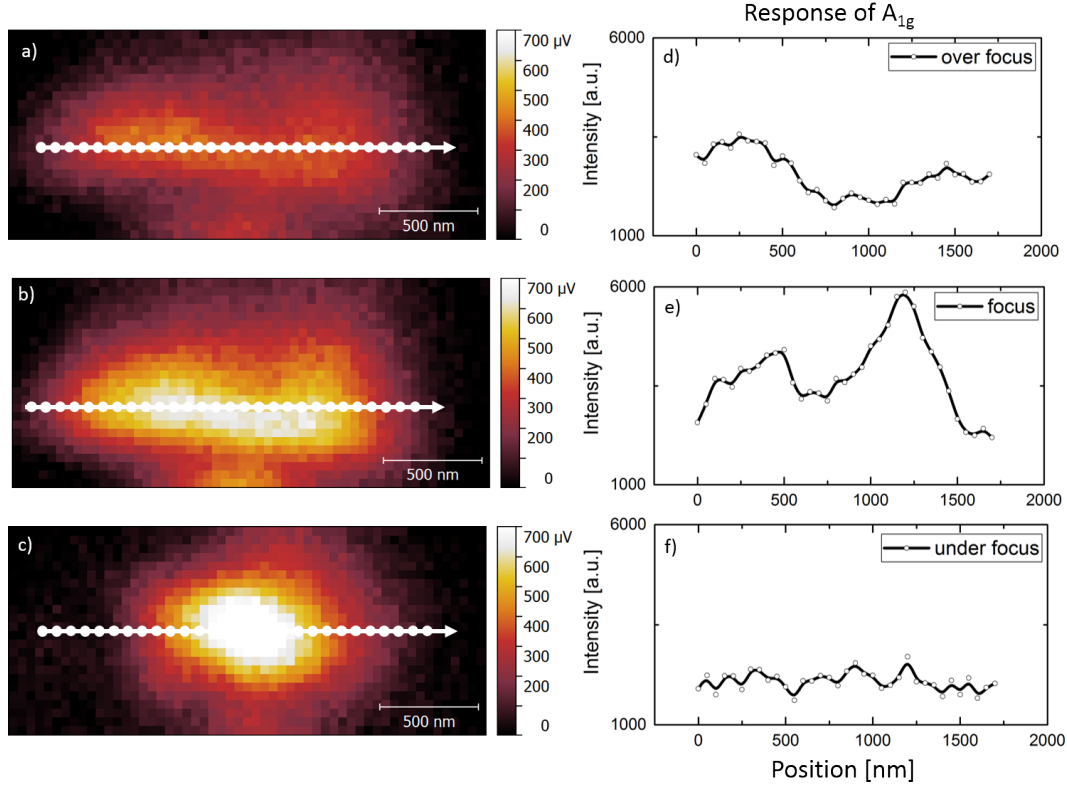


Figure 4.15: An example of combined measurements on MoS₂ monolayer flakes. (a-c) PiFM images of the initial focus positions. Each spot along the line scan represents one TERS spectrum, from which the response of the A_{1g} mode has been extracted and analyzed, shown in (d-f). To rate the objective response of the A_{1g} mode according to the present electromagnetic field, the intrinsically increasing background has been subtracted. Image is taken from [200] with permission.

Considering Figure 4.15 (a), the overfocused condition, the PiFM experiment reveals a vague double lobe structure with a weaker signal compared to the focus condition. The latter is comparable to the situation on bare glass ((I) in Figure 4.14 (c)). Plotting the response of the A_{1g} mode over the lateral position for this overfocused condition shows that the A_{1g} mode follows the E_z -field distribution and the maximum peak intensity can be found as expected in the side lobes, here $\approx 3\text{k}$ counts (Figure 4.15 (d)). In Figure 4.15 (b), PiFM probes the axial field distribution (z-component) of the incoming electromagnetic field in an ideally focused case, hence ideal TERS conditions. A clear double lobe structure is detected in the PiFM experiment. Analyzing the respective response of the A_{1g} vibrational mode along a profile through this double lobe shows, again, that the intensity of the A_{1g} mode is strongly enhanced when matching the E_z -field component synchronously investigated by PiFM. Here, the maximum peak intensity reaches 6k counts, and the over-

all trend perfectly follows the double lobe structure (Figure 4.15 (e)). This is also the experimental proof that at the focus position PiFM probes the short-range gradient force, being responsible for the enhancement of the respective out-of-plane A_{1g} mode. Last not least, Figure 4.15 (c) refers to the underfocused condition. As in (III) Figure 4.14 (c) on bare glass, a round spot is detected by PiFM. As discussed beforehand, in sideband mode PiFM measures in z-direction under such focusing conditions the gradient of the overall forces being present, which refers in this case to the long-range scattering force. Accordingly, the measured force in Figure 4.14 (c) is proportional to the $E_{x,y}$ -field components of the incident light. Therefore, the A_{1g} out-of-plane mode shows no axial response (Figure 4.14 (c)), and an overall stable intensity profile with a comparably low enhancement over all positions is observed. Moreover, operating in underfocused (relatively high transversal field components) condition, the tip will only enhance E_z -field components. Hence, the transversal components cannot be sufficiently enhanced with the present tip geometry. In this context it should be also mentioned that the investigation of the E_{2g}^1 band, especially in the underfocused scenario, raises a point of interest but would require extremely long acquisition times, particularly for the very interesting out-of-focus regions. In summary, the combined PiFM and TERS experiment on a MoS_2 monolayer substantiates the effective enhancement via the corresponding field distribution necessary for successful TERS experiments and emphasizes the importance of the correct axial focal, as well as lateral tip position [200].

This chapter introduced photo-induced force microscopy (PiFM) as a new and powerful near-field technique. We started with an introduction and then the theory behind the optical force interaction at the nanoscale in terms of dipole-dipole approximation (DDA) and Maxwell stress tensor, along with the view of sideband detection. Next, we investigated some applications of PiFM, from beam profile mapping to revealing plasmon response of nanostructure with outstanding spatial resolution. Lastly, we focused some fundamental investigation in PiFM and, for the first time, showed the effect of focal position in PiFM both in theory and experiment and combined with TERS.

5. Summary and Outlook

This work delves into the multidisciplinary field of near-field optics, a branch of microscopy that enables researchers to visualize extremely small objects with high precision. The initial section of the work presents a novel approach to analyze the height distribution of SARS-CoV-2 virus samples by utilizing an atomic force microscope (AFM). The AFM is a specialized microscope that utilizes a sharp probe to scan the surface of a sample and generate a three-dimensional representation of its topography. The study highlights the importance of accurate height measurements in the characterization of the virus's structure, a crucial factor in developing targeted treatments and vaccines. The second section of the work discusses the design and behavior of plasmonic probes, tiny structures used in near-field optical microscopy. The research indicates that the foremost particle of the probe plays a critical role in obtaining a strong near-field enhancement, while the other particles contribute in enhancing far-field scattering. Additionally, the study investigates the mechanical properties of probes, which are critical in newer microscopy techniques such as torsional force microscopy and photo-induced force microscopy. Finally, the study examines the applications of photo-induced force microscopy in various fields, including the evaluation of plasmonic probe quality, the creation of maps of electromagnetic fields, and the study of the optical properties of plasmonic nanoparticles. The work emphasizes the synergy of multiple technologies and their potential for enabling breakthroughs in fields such as medicine and materials science. In summary, this work illustrates how diverse technologies can converge to develop powerful tools for studying nanoscale objects, ultimately advancing research in numerous scientific disciplines.

Looking ahead, the algorithm developed for batch processing of AFM data can be applied to a wide range of samples beyond the inactivated SARS-CoV-2 samples analyzed in this study, enabling faster and more efficient analysis of data obtained from AFM measurements. The insights gained from modeling plasmonic probes and their behavior can inform the design of new and improved near-field optical microscopy techniques. Additionally, the advancements in technologies such as torsional force microscopy and photo-induced force microscopy open up new avenues for studying materials and biological samples at the nanoscale. Overall, the findings of this study have the potential to drive progress in the field of near-field optics and contribute to a better understanding of nanoscale phenomena.

Zusammenfassung

Diese Arbeit befasst sich mit dem multidisziplinären Gebiet der Nahfeldoptik, einem Zweig der Mikroskopie, der es Forschern ermöglicht, extrem kleine Objekte mit hoher Präzision sichtbar zu machen. Im ersten Teil der Arbeit wird ein neuartiger Ansatz zur Analyse der Höhenverteilung von SARS-CoV-2-Virusproben mit Hilfe eines Rasterkraftmikroskops (AFM) vorgestellt. Das AFM ist ein spezielles Mikroskop, das eine scharfe Sonde verwendet, um die Oberfläche einer Probe abzutasten und eine dreidimensionale Darstellung ihrer Topografie zu erzeugen. Die Studie unterstreicht die Bedeutung genauer Höhenmessungen für die Charakterisierung der Virusstruktur, die für die Entwicklung gezielter Behandlungen und Impfstoffe von entscheidender Bedeutung ist. Der zweite Teil der Arbeit befasst sich mit dem Design und dem Verhalten von plasmonischen Sonden, winzigen Strukturen, die in der optischen Nahfeldmikroskopie verwendet werden. Die Forschung zeigt, dass das vorderste Teilchen der Sonde eine entscheidende Rolle bei der Verstärkung des Nahfeldes spielt, während die anderen Teilchen die Streuung im Fernfeld verstärken. Darüber hinaus werden in der Studie die mechanischen Eigenschaften der Sonden untersucht, die für neuere Mikroskopietechniken wie die Torsionskraftmikroskopie und die photoinduzierte Kraftmikroskopie von entscheidender Bedeutung sind. Schließlich untersucht die Studie die Anwendungen der photoinduzierten Kraftmikroskopie in verschiedenen Bereichen, darunter die Bewertung der Qualität plasmonischer Sonden, die Erstellung von Karten elektromagnetischer Felder und die Untersuchung der optischen Eigenschaften plasmonischer Nanopartikel. Die Arbeit unterstreicht die Synergie mehrerer Technologien und ihr Potenzial, Durchbrüche in Bereichen wie der Medizin und der Materialwissenschaft zu ermöglichen. Zusammenfassend lässt sich sagen, dass diese Arbeit zeigt, wie verschiedene Technologien konvergieren können, um leistungsstarke Werkzeuge für die Untersuchung von Objekten im Nanomaßstab zu entwickeln, die letztendlich die Forschung in zahlreichen wissenschaftlichen Disziplinen voranbringen.

Der Algorithmus, der für die Stapelverarbeitung von AFM-Daten entwickelt wurde, kann über die in dieser Studie analysierten inaktivierten SARS-CoV-2-Proben hinaus auf eine breite Palette von Proben angewandt werden und ermöglicht eine schnellere und effizientere Analyse von Daten aus AFM-Messungen. Die aus der Modellierung plasmonischer Sonden und ihres Verhaltens gewonnenen Erkenntnisse können die Entwicklung neuer und verbesserter optischer Nahfeldmikroskopietechniken unterstützen. Darüber hinaus eröffnen die Fortschritte bei Technologien wie der Torsionskraftmikroskopie und der

photoinduzierten Kraftmikroskopie neue Möglichkeiten für die Untersuchung von Materialien und biologischen Proben im Nanomaßstab. Insgesamt haben die Ergebnisse dieser Studie das Potenzial, den Fortschritt auf dem Gebiet der Nahfeldoptik voranzutreiben und zu einem besseren Verständnis von Phänomenen im Nanobereich beizutragen.

6. Bibliography

- [1] L. Rayleigh, “Xv. on the theory of optical images, with special reference to the microscope,” *The London, Edinburgh, and Dublin Philosophical Magazine and Journal of Science*, vol. 42, no. 255, pp. 167–195, 1896.
- [2] E. Abbe, “Beiträge zur Theorie des Mikroskops und der mikroskopischen Wahrnehmung,” *Archiv für mikroskopische Anatomie*, vol. 9, no. 1, pp. 413–468, 1873.
- [3] E. Betzig and J. K. Trautman, “Near-field optics: microscopy, spectroscopy, and surface modification beyond the diffraction limit,” *Science*, vol. 257, no. 5067, pp. 189–195, 1992.
- [4] E. Betzig and R. J. Chichester, “Single molecules observed by near-field scanning optical microscopy,” *Science*, vol. 262, no. 5138, pp. 1422–1425, 1993.
- [5] E. Synge, “Xxxviii. a suggested method for extending microscopic resolution into the ultra-microscopic region,” *The London, Edinburgh, and Dublin Philosophical Magazine and Journal of Science*, vol. 6, no. 35, pp. 356–362, 1928.
- [6] L. Novotny and B. Hecht, *Principles of nano-optics*. Cambridge university press, 2012.
- [7] J. A. O’Keefe, “Resolving power of visible light,” *JOSA*, vol. 46, no. 5, pp. 359–359, 1956.
- [8] E. Ash and G. Nicholls, “Super-resolution aperture scanning microscope,” *Nature*, vol. 237, no. 5357, pp. 510–512, 1972.
- [9] G. Binnig, H. Rohrer, C. Gerber, and E. Weibel, “Tunneling through a controllable vacuum gap,” *Applied Physics Letters*, vol. 40, no. 2, pp. 178–180, 1982.
- [10] G. A. Massey, “Microscopy and pattern generation with scanned evanescent waves,” *Applied Optics*, vol. 23, no. 5, pp. 658–660, 1984.
- [11] D. W. Pohl, W. Denk, and M. Lanz, “Optical stethoscopy: Image recording with resolution $\lambda/20$,” *Applied physics letters*, vol. 44, no. 7, pp. 651–653, 1984.

- [12] A. Lewis, M. Isaacson, A. Harootunian, and A. Muray, "Development of a 500 Å spatial resolution light microscope: I. light is efficiently transmitted through $\lambda/16$ diameter apertures," *Ultramicroscopy*, vol. 13, no. 3, pp. 227–231, 1984.
- [13] E. Betzig, M. Isaacson, and A. Lewis, "Collection mode near-field scanning optical microscopy," *Applied physics letters*, vol. 51, no. 25, pp. 2088–2090, 1987.
- [14] E. Betzig, J. K. Trautman, T. Harris, J. Weiner, and R. Kostelak, "Breaking the diffraction barrier: optical microscopy on a nanometric scale," *Science*, vol. 251, no. 5000, pp. 1468–1470, 1991.
- [15] F. Zenhausern, M. O'boyle, and H. Wickramasinghe, "Apertureless near-field optical microscope," *Applied Physics Letters*, vol. 65, no. 13, pp. 1623–1625, 1994.
- [16] W. Githui, F. Kitui, E. Juma, D. Obwana, J. Mwai, and D. Kwamanga, "A comparative study on the reliability of the fluorescence microscopy and ziehl-neelsen method in the diagnosis of pulmonary tuberculosis.," *East African medical journal*, vol. 70, no. 5, pp. 263–266, 1993.
- [17] S. Nie and S. R. Emory, "Probing single molecules and single nanoparticles by surface-enhanced raman scattering," *science*, vol. 275, no. 5303, pp. 1102–1106, 1997.
- [18] J. Wessel, "Surface-enhanced optical microscopy," *JOSA B*, vol. 2, no. 9, pp. 1538–1541, 1985.
- [19] M. S. Anderson, "Locally enhanced Raman spectroscopy with an atomic force microscope," *Applied Physics Letters*, vol. 76, no. 21, pp. 3130–3132, 2000.
- [20] R. M. Stöckle, Y. D. Suh, V. Deckert, and R. Zenobi, "Nanoscale chemical analysis by tip-enhanced Raman spectroscopy," *Chemical Physics Letters*, vol. 318, no. 1-3, pp. 131–136, 2000.
- [21] D. Pohl, "Scanning near-field optical microscopy (snom)," in *Advances in optical and electron microscopy*, vol. 12, pp. 243–312, Elsevier, 1991.
- [22] U. Dürig, D. W. Pohl, and F. Rohner, "Near-field optical-scanning microscopy," *Journal of applied physics*, vol. 59, no. 10, pp. 3318–3327, 1986.
- [23] R. Zenobi and V. Deckert, "Scanning near-field optical microscopy and spectroscopy as a tool for chemical analysis," *Angewandte Chemie International Edition*, vol. 39, no. 10, pp. 1746–1756, 2000.

- [24] L. Novotny and S. J. Stranick, “Near-field optical microscopy and spectroscopy with pointed probes,” *Annu. Rev. Phys. Chem.*, vol. 57, pp. 303–331, 2006.
- [25] P. Verma, “Tip-enhanced Raman spectroscopy: technique and recent advances,” *Chemical reviews*, vol. 117, no. 9, pp. 6447–6466, 2017.
- [26] T. Deckert-Gaudig, A. Taguchi, S. Kawata, and V. Deckert, “Tip-enhanced Raman spectroscopy—from early developments to recent advances,” *Chemical Society Reviews*, vol. 46, no. 13, pp. 4077–4110, 2017.
- [27] I. Rajapaksa, K. Uenal, and H. K. Wickramasinghe, “Image force microscopy of molecular resonance: A microscope principle,” *Applied physics letters*, vol. 97, no. 7, p. 073121, 2010.
- [28] J. Jahng, J. Brocious, D. A. Fishman, F. Huang, X. Li, V. A. Tamma, H. K. Wickramasinghe, and E. O. Potma, “Gradient and scattering forces in photoinduced force microscopy,” *Physical Review B*, vol. 90, no. 15, p. 155417, 2014.
- [29] J. Jahng, D. A. Fishman, S. Park, D. B. Nowak, W. A. Morrison, H. K. Wickramasinghe, and E. O. Potma, “Linear and nonlinear optical spectroscopy at the nanoscale with photoinduced force microscopy,” *Accounts of chemical research*, vol. 48, no. 10, pp. 2671–2679, 2015.
- [30] A. Ambrosio, R. C. Devlin, F. Capasso, and W. L. Wilson, “Observation of nanoscale refractive index contrast via photoinduced force microscopy,” *ACS Photonics*, vol. 4, no. 4, pp. 846–851, 2017.
- [31] B. Kim, J. Jahng, R. M. Khan, S. Park, and E. O. Potma, “Eigenmodes of a quartz tuning fork and their application to photoinduced force microscopy,” *Physical Review B*, vol. 95, no. 7, p. 075440, 2017.
- [32] F. Huang, V. A. Tamma, Z. Mardy, J. Burdett, and H. K. Wickramasinghe, “Imaging nanoscale electromagnetic near-field distributions using optical forces,” *Scientific reports*, vol. 5, no. 1, pp. 1–12, 2015.
- [33] T. U. Tumkur, X. Yang, B. Cerjan, N. J. Halas, P. Nordlander, and I. Thomann, “Photoinduced force mapping of plasmonic nanostructures,” *Nano letters*, vol. 16, no. 12, pp. 7942–7949, 2016.
- [34] T. Tumkur, X. Yang, C. Zhang, J. Yang, Y. Zhang, G. V. Naik, P. Nordlander, and N. J. Halas, “Wavelength-dependent optical force imaging of bimetallic al–au heterodimers,” *Nano letters*, vol. 18, no. 3, pp. 2040–2046, 2018.

- [35] G. Binnig, C. F. Quate, and C. Gerber, “Atomic force microscope,” *Physical review letters*, vol. 56, no. 9, p. 930, 1986.
- [36] R. Petry, M. Schmitt, and J. Popp, “Raman spectroscopy—a prospective tool in the life sciences,” *ChemPhysChem*, vol. 4, no. 1, pp. 14–30, 2003.
- [37] BudgetSensors, “AFM Probes Catalogue.” <https://www.budgetsensors.com/pdf/budgetsensors-brochure.pdf>, 2019.
- [38] R. M. Stöckle, V. Deckert, C. Fokas, and R. Zenobi, “Controlled formation of isolated silver islands for surface-enhanced Raman scattering,” *Applied Spectroscopy*, vol. 54, no. 11, pp. 1577–1583, 2000.
- [39] N. Hayazawa, Y. Inouye, Z. Sekkat, and S. Kawata, “Metallized tip amplification of near-field Raman scattering,” *Optics Communications*, vol. 183, no. 1-4, pp. 333–336, 2000.
- [40] A. Rasmussen and V. Deckert, “Surface-and tip-enhanced Raman scattering of dna components,” *Journal of Raman Spectroscopy: An International Journal for Original Work in all Aspects of Raman Spectroscopy, Including Higher Order Processes, and also Brillouin and Rayleigh Scattering*, vol. 37, no. 1-3, pp. 311–317, 2006.
- [41] B.-S. Yeo, W. Zhang, C. Vannier, and R. Zenobi, “Enhancement of Raman signals with silver-coated tips,” *Applied spectroscopy*, vol. 60, no. 10, pp. 1142–1147, 2006.
- [42] M. Asghari-Khiavi, B. R. Wood, P. Hojati-Talemi, A. Downes, D. McNaughton, and A. Mechler, “Exploring the origin of tip-enhanced Raman scattering; preparation of efficient ters probes with high yield,” *Journal of Raman Spectroscopy*, vol. 43, no. 2, pp. 173–180, 2012.
- [43] V. Deckert, T. Deckert-Gaudig, M. Diegel, I. Götz, L. Langelüddecke, H. Schneidewind, G. Sharma, P. Singh, P. Singh, S. Trautmann, *et al.*, “Spatial resolution in Raman spectroscopy,” *Faraday Discussions*, vol. 177, pp. 9–20, 2015.
- [44] A. Taguchi, N. Hayazawa, K. Furusawa, H. Ishitobi, and S. Kawata, “Deep-uv tip-enhanced Raman scattering,” *Journal of Raman Spectroscopy: An International Journal for Original Work in all Aspects of Raman Spectroscopy, Including Higher Order Processes, and also Brillouin and Rayleigh Scattering*, vol. 40, no. 9, pp. 1324–1330, 2009.
- [45] D. Mehtani, N. Lee, R. Hartschuh, A. Kisliuk, M. Foster, A. Sokolov, and J. Maguire, “Nano-Raman spectroscopy with side-illumination optics,”

- Journal of Raman Spectroscopy: An International Journal for Original Work in all Aspects of Raman Spectroscopy, Including Higher Order Processes, and also Brillouin and Rayleigh Scattering*, vol. 36, no. 11, pp. 1068–1075, 2005.
- [46] W. Sun and Z. Shen, “Apertureless near-field scanning Raman microscopy using reflection scattering geometry,” *Ultramicroscopy*, vol. 94, no. 3-4, pp. 237–244, 2003.
 - [47] K. A. Chan and S. G. Kazarian, “Tip-enhanced Raman mapping with top-illumination afm,” *Nanotechnology*, vol. 22, no. 17, p. 175701, 2011.
 - [48] L. Zhu, C. Georgi, M. Hecker, J. Rinderknecht, A. Mai, Y. Ritz, and E. Zschech, “Nano-Raman spectroscopy with metallized atomic force microscopy tips on strained silicon structures,” *Journal of Applied Physics*, vol. 101, no. 10, p. 104305, 2007.
 - [49] F. Pampaloni, E. G. Reynaud, and E. H. Stelzer, “The third dimension bridges the gap between cell culture and live tissue,” *Nature reviews Molecular cell biology*, vol. 8, no. 10, pp. 839–845, 2007.
 - [50] N. Hernández-Pedro, E. Rangel-López, B. Pineda, and J. Sotelo, “Atomic force microscopy in detection of viruses,” *Atomic Force Microscopy Investigations into Biology-From Cell to Protein. INTECH. Rijeka, Croatia*, pp. 235–252, 2012.
 - [51] P. E. Florian, Y. Rouillé, S. Ruta, N. Nichita, and A. Roseanu, “Recent advances in human viruses imaging studies,” *Journal of Basic Microbiology*, vol. 56, no. 6, pp. 591–607, 2016.
 - [52] M. G. Rossmann, R. Bernal, and S. V. Pletnev, “Combining electron microscopic with x-ray crystallographic structures,” *Journal of structural biology*, vol. 136, no. 3, pp. 190–200, 2001.
 - [53] J. Ayache, L. Beaunier, J. Boumendil, G. Ehret, and D. Laub, *Sample preparation handbook for transmission electron microscopy: techniques*, vol. 2. Springer Science & Business Media, 2010.
 - [54] M. Adrian, J. Dubochet, J. Lepault, and A. W. McDowell, “Cryo-electron microscopy of viruses,” *Nature*, vol. 308, no. 5954, pp. 32–36, 1984.
 - [55] Z. Shao, J. Yang, and A. P. Somlyo, “Biological atomic force microscopy: from microns to nanometers and beyond,” *Annual review of cell and developmental biology*, vol. 11, no. 1, pp. 241–265, 1995.

- [56] M. Radmacher, R. Tillmann, M. Fritz, and H. Gaub, “From molecules to cells: imaging soft samples with the atomic force microscope,” *Science*, vol. 257, no. 5078, pp. 1900–1905, 1992.
- [57] Y. G. Kuznetsov, J. J. Dowell, J. A. Gavira, J. D. Ng, and A. McPherson, “Biophysical and atomic force microscopy characterization of the rna from satellite tobacco mosaic virus,” *Nucleic acids research*, vol. 38, no. 22, pp. 8284–8294, 2010.
- [58] Y. G. Kuznetsov, J. R. Gurnon, J. L. Van Etten, and A. McPherson, “Atomic force microscopy investigation of a chlorella virus, pbcv-1,” *Journal of structural biology*, vol. 149, no. 3, pp. 256–263, 2005.
- [59] Y. G. Kuznetsov, C. Xiao, S. Sun, D. Raoult, M. Rossmann, and A. McPherson, “Atomic force microscopy investigation of the giant mimivirus,” *Virology*, vol. 404, no. 1, pp. 127–137, 2010.
- [60] S. Lyonnais, M. Hénaut, A. Neyret, P. Merida, C. Cazevielle, N. Gros, C. Chable-Bessia, and D. Muriaux, “Direct visualization of native infectious sars-cov-2 and its inactivation forms using high resolution atomic force microscopy,” *bioRxiv*, 2020.
- [61] M. E. Darnell, K. Subbarao, S. M. Feinstone, and D. R. Taylor, “Inactivation of the coronavirus that induces severe acute respiratory syndrome, sars-cov,” *Journal of virological methods*, vol. 121, no. 1, pp. 85–91, 2004.
- [62] E. I. Patterson, T. Prince, E. R. Anderson, A. Casas-Sanchez, S. L. Smith, C. Cansado-Utrilla, T. Solomon, M. J. Griffiths, Á. Acosta-Serrano, L. Turtle, *et al.*, “Methods of inactivation of sars-cov-2 for downstream biological assays,” *The Journal of infectious diseases*, vol. 222, no. 9, pp. 1462–1467, 2020.
- [63] H. Rabenau, L. Biesert, T. Schmidt, G. Bauer, J. Cinatl, and H. Doerr, “Sars-coronavirus (sars-cov) and the safety of a solvent/detergent (s/d) treated immunoglobulin preparation,” *Biologicals*, vol. 33, no. 2, pp. 95–99, 2005.
- [64] H. Rabenau, J. Cinatl, B. Morgenstern, G. Bauer, W. Preiser, and H. Doerr, “Stability and inactivation of sars coronavirus,” *Medical microbiology and immunology*, vol. 194, no. 1, pp. 1–6, 2005.
- [65] C. S. Heilingloh, U. W. Aufderhorst, L. Schipper, U. Dittmer, O. Witzke, D. Yang, X. Zheng, K. Sutter, M. Trilling, M. Alt, *et al.*, “Susceptibility of sars-cov-2 to uv irradiation,” *American journal of infection control*, vol. 48, no. 10, pp. 1273–1275, 2020.

- [66] <http://gwyddion.net>.
- [67] D. Nečas and P. Klapetek, “Gwyddion: an open-source software for SPM data analysis,” *Central European Journal of Physics*, vol. 10, pp. 181–188, 2012.
- [68] <https://jpk-data-processing.updatestar.com/en>.
- [69] <https://github.com/kouroshezraei/JPK-data-analysis-topography>.
- [70] S. Lyonnais, M. Hénaut, A. Neyret, P. Merida, C. Cazevieuille, N. Gros, C. Chable-Bessia, and D. Muriaux, “Atomic force microscopy analysis of native infectious and inactivated sars-cov-2 virions,” *Scientific reports*, vol. 11, no. 1, pp. 1–7, 2021.
- [71] J. C. Maxwell, *A dynamical theory of the electromagnetic field*. Wipf and Stock Publishers, 1996.
- [72] C. Castelnovo, R. Moessner, and S. L. Sondhi, “Magnetic monopoles in spin ice,” *Nature*, vol. 451, no. 7174, pp. 42–45, 2008.
- [73] A. Volyar and T. Fadeeva, “Laguerre-gaussian beams with complex and real arguments in a uniaxial crystal,” *Optics and spectroscopy*, vol. 101, no. 3, pp. 450–457, 2006.
- [74] C. Maurer, A. Jesacher, S. Fürhapter, S. Bernet, and M. Ritsch-Marte, “Tailoring of arbitrary optical vector beams,” *New Journal of Physics*, vol. 9, no. 3, p. 78, 2007.
- [75] H. Kang, B. Jia, and M. Gu, “Polarization characterization in the focal volume of high numerical aperture objectives,” *Optics express*, vol. 18, no. 10, pp. 10813–10821, 2010.
- [76] S. Vyas, Y. Kozawa, and Y. Miyamoto, “Creation of polarization gradients from superposition of counter propagating vector lg beams,” *Optics express*, vol. 23, no. 26, pp. 33970–33979, 2015.
- [77] U. Levy and Y. Silberberg, “Weakly diverging to tightly focused gaussian beams: a single set of analytic expressions,” *JOSA A*, vol. 33, no. 10, pp. 1999–2009, 2016.
- [78] B. E. Saleh and M. C. Teich, *Fundamentals of photonics*. John Wiley & sons, 2019.
- [79] G. Goubau and F. Schwing, “On the guided propagation of electromagnetic wave beams,” *IRE Transactions on Antennas and Propagation*, vol. 9, no. 3, pp. 248–256, 1961.

- [80] L. Allen, M. W. Beijersbergen, R. Spreeuw, and J. Woerdman, “Orbital angular momentum of light and the transformation of laguerre-gaussian laser modes,” *Physical review A*, vol. 45, no. 11, p. 8185, 1992.
- [81] B. Schrader, *Infrared and Raman spectroscopy: methods and applications*. John Wiley & Sons, 2008.
- [82] T. E. Madey and J. T. Yates Jr, *Vibrational spectroscopy of molecules on surfaces*, vol. 1. Springer Science & Business Media, 2013.
- [83] J. Popp and W. Kiefer, “Encyclopedia of analytical chemistry: Applications, theory and instrumentation,” 2000.
- [84] S. A. Maier, *Plasmonics: fundamentals and applications*. Springer Science & Business Media, 2007.
- [85] A. Otto, “Excitation of nonradiative surface plasma waves in silver by the method of frustrated total reflection,” *Zeitschrift für Physik A Hadrons and nuclei*, vol. 216, no. 4, pp. 398–410, 1968.
- [86] E. Kretschmann, “Die bestimmung optischer konstanten von metallen durch anregung von oberflächenplasmaschwingungen,” *Zeitschrift für Physik A Hadrons and nuclei*, vol. 241, no. 4, pp. 313–324, 1971.
- [87] W. L. Barnes, A. Dereux, and T. W. Ebbesen, “Surface plasmon sub-wavelength optics,” *nature*, vol. 424, no. 6950, pp. 824–830, 2003.
- [88] M. J. Banholzer, J. E. Millstone, L. Qin, and C. A. Mirkin, “Rationally designed nanostructures for surface-enhanced Raman spectroscopy,” *Chemical Society Reviews*, vol. 37, no. 5, pp. 885–897, 2008.
- [89] K. A. Willets and R. P. Van Duyne, “Localized surface plasmon resonance spectroscopy and sensing,” *Annu. Rev. Phys. Chem.*, vol. 58, pp. 267–297, 2007.
- [90] K. M. Mayer and J. H. Hafner, “Localized surface plasmon resonance sensors,” *Chemical reviews*, vol. 111, no. 6, pp. 3828–3857, 2011.
- [91] L. Novotny, R. X. Bian, and X. S. Xie, “Theory of nanometric optical tweezers,” *Physical Review Letters*, vol. 79, no. 4, p. 645, 1997.
- [92] A. V. Zayats, I. I. Smolyaninov, and A. A. Maradudin, “Nano-optics of surface plasmon polaritons,” *Physics reports*, vol. 408, no. 3-4, pp. 131–314, 2005.

- [93] P. Verma, T. Ichimura, T.-a. Yano, Y. Saito, and S. Kawata, “Nano-imaging through tip-enhanced Raman spectroscopy: Stepping beyond the classical limits,” *Laser & Photonics Reviews*, vol. 4, no. 4, pp. 548–561, 2010.
- [94] D. K. Gramotnev and S. I. Bozhevolnyi, “Nanofocusing of electromagnetic radiation,” *Nature Photonics*, vol. 8, no. 1, pp. 13–22, 2014.
- [95] G. Mie, “Beiträge zur optik trüber medien, speziell kolloidaler metallösungen,” *Annalen der physik*, vol. 330, no. 3, pp. 377–445, 1908.
- [96] C. F. Bohren and D. R. Huffman, *Absorption and scattering of light by small particles*. John Wiley & Sons, 2008.
- [97] A. M. Winslow, “Numerical solution of the quasilinear poisson equation in a nonuniform triangle mesh,” *Journal of computational physics*, vol. 1, no. 2, pp. 149–172, 1966.
- [98] K. Yee, “Numerical solution of initial boundary value problems involving maxwell’s equations in isotropic media,” *IEEE Transactions on antennas and propagation*, vol. 14, no. 3, pp. 302–307, 1966.
- [99] R. Harrington, “Field computation by moment methods, macmillan,” *New York*, pp. 1–21, 1968.
- [100] C. Trowbridge and J. Sykulski, “Some key developments in computational electromagnetics and their attribution,” *IEEE transactions on magnetics*, vol. 42, no. 4, pp. 503–508, 2006.
- [101] <https://www.comsol.com>.
- [102] <https://www.cst.com>.
- [103] <https://www.lumerical.com>.
- [104] M. Kupresak, X. Zheng, G. A. Vandenbosch, and V. Moshchalkov, “Benchmarking of software tools for the characterization of nanoparticles,” *Optics Express*, vol. 25, no. 22, pp. 26760–26780, 2017.
- [105] S. Trautmann, “Experimentelle und theoretische untersuchung der ortsauflösung von plasmonischen nahfeldsonden,” *PhD Thesis*, 2020.
- [106] A. Taguchi, N. Hayazawa, Y. Saito, H. Ishitobi, A. Tarun, and S. Kawata, “Controlling the plasmon resonance wavelength in metal-coated probe using refractive index modification,” *Optics express*, vol. 17, no. 8, pp. 6509–6518, 2009.

- [107] M. Nicklaus, *Tip-enhanced Raman spectroscopy for nanoelectronics*. BoD–Books on Demand, 2014.
- [108] N. Hayazawa, Y. Inouye, Z. Sekkat, and S. Kawata, “Near-field Raman imaging of organic molecules by an apertureless metallic probe scanning optical microscope,” *The Journal of chemical physics*, vol. 117, no. 3, pp. 1296–1301, 2002.
- [109] L. Novotny, E. J. Sánchez, and X. S. Xie, “Near-field optical imaging using metal tips illuminated by higher-order hermite–gaussian beams,” *Ultramicroscopy*, vol. 71, no. 1-4, pp. 21–29, 1998.
- [110] A. Downes, D. Salter, and A. Elfick, “Finite element simulations of tip-enhanced Raman and fluorescence spectroscopy,” *The Journal of Physical Chemistry B*, vol. 110, no. 13, pp. 6692–6698, 2006.
- [111] J. Stadler, B. Oswald, T. Schmid, and R. Zenobi, “Characterizing unusual metal substrates for gap-mode tip-enhanced Raman spectroscopy,” *Journal of Raman Spectroscopy*, vol. 44, no. 2, pp. 227–233, 2013.
- [112] T. Deckert-Gaudig and V. Deckert, “Ultraflat transparent gold nanoplates—ideal substrates for tip-enhanced Raman scattering experiments,” *Small*, vol. 5, no. 4, pp. 432–436, 2009.
- [113] R. Dorn, S. Quabis, and G. Leuchs, “Sharper focus for a radially polarized light beam,” *Physical review letters*, vol. 91, no. 23, p. 233901, 2003.
- [114] S. Quabis, R. Dorn, M. Eberler, O. Glöckl, and G. Leuchs, “Focusing light to a tighter spot,” *Optics communications*, vol. 179, no. 1-6, pp. 1–7, 2000.
- [115] J. Zeng, F. Huang, C. Guclu, M. Veysi, M. Albooyeh, H. K. Wickramasinghe, and F. Capolino, “Sharply focused azimuthally polarized beams with magnetic dominance: near-field characterization at nanoscale by photoinduced force microscopy,” *ACS Photonics*, vol. 5, no. 2, pp. 390–397, 2018.
- [116] Y. Saito and P. Verma, “Polarization-controlled Raman microscopy and nanoscopy,” *The journal of physical chemistry letters*, vol. 3, no. 10, pp. 1295–1300, 2012.
- [117] G. Sharma, T. Deckert-Gaudig, and V. Deckert, “Tip-enhanced Raman scattering—targeting structure-specific surface characterization for biomedical samples,” *Advanced drug delivery reviews*, vol. 89, pp. 42–56, 2015.

- [118] A. Taguchi, J. Yu, P. Verma, and S. Kawata, “Optical antennas with multiple plasmonic nanoparticles for tip-enhanced Raman microscopy,” *Nanoscale*, vol. 7, no. 41, pp. 17424–17433, 2015.
- [119] P. Anger, P. Bharadwaj, and L. Novotny, “Enhancement and quenching of single-molecule fluorescence,” *Physical review letters*, vol. 96, no. 11, p. 113002, 2006.
- [120] M. Fleischer, A. Weber-Bargioni, M. V. P. Altoe, A. M. Schwartzberg, P. J. Schuck, S. Cabrini, and D. P. Kern, “Gold nanocone near-field scanning optical microscopy probes,” *ACS nano*, vol. 5, no. 4, pp. 2570–2579, 2011.
- [121] M. Yang, M. S. Mattei, C. R. Cherqui, X. Chen, R. P. Van Duyne, and G. C. Schatz, “Tip-enhanced Raman excitation spectroscopy (teres): direct spectral characterization of the gap-mode plasmon,” *Nano letters*, vol. 19, no. 10, pp. 7309–7316, 2019.
- [122] W. Zhang, X. Cui, B.-S. Yeo, T. Schmid, C. Hafner, and R. Zenobi, “Nanoscale roughness on metal surfaces can increase tip-enhanced Raman scattering by an order of magnitude,” *Nano letters*, vol. 7, no. 5, pp. 1401–1405, 2007.
- [123] X. Cui, D. Erni, W. Zhang, and R. Zenobi, “Highly efficient nano-tips with metal–dielectric coatings for tip-enhanced spectroscopy applications,” *Chemical Physics Letters*, vol. 453, no. 4-6, pp. 262–265, 2008.
- [124] S. Trautmann, M. Richard-Lacroix, A. Dathe, H. Schneidewind, J. Dellith, W. Fritzsche, and V. Deckert, “Plasmon response evaluation based on image-derived arbitrary nanostructures,” *Nanoscale*, vol. 10, no. 21, pp. 9830–9839, 2018.
- [125] S. Trautmann, J. Aizpurua, I. Götz, A. Undisz, J. Dellith, H. Schneidewind, M. Rettenmayr, and V. Deckert, “A classical description of subnanometer resolution by atomic features in metallic structures,” *Nanoscale*, vol. 9, no. 1, pp. 391–401, 2017.
- [126] D. Nečas and P. Klapetek, “Gwyddion: an open-source software for spm data analysis,” *Open Physics*, vol. 10, no. 1, pp. 181–188, 2012.
- [127] T. Attanayake, M. Premaratne, and G. P. Agrawal, “Characterizing the optical response of symmetric hemispherical nano-dimers,” *Plasmonics*, vol. 10, no. 6, pp. 1453–1466, 2015.

- [128] E. Hao and G. C. Schatz, “Electromagnetic fields around silver nanoparticles and dimers,” *The Journal of chemical physics*, vol. 120, no. 1, pp. 357–366, 2004.
- [129] R. Esteban, A. Zugarramurdi, P. Zhang, P. Nordlander, F. J. García-Vidal, A. G. Borisov, and J. Aizpurua, “A classical treatment of optical tunneling in plasmonic gaps: extending the quantum corrected model to practical situations,” *Faraday discussions*, vol. 178, pp. 151–183, 2015.
- [130] T. V. Teperik, P. Nordlander, J. Aizpurua, and A. G. Borisov, “Quantum effects and nonlocality in strongly coupled plasmonic nanowire dimers,” *Optics express*, vol. 21, no. 22, pp. 27306–27325, 2013.
- [131] Y. Wang, Z. Li, K. Zhao, A. Sobhani, X. Zhu, Z. Fang, and N. J. Halas, “Substrate-mediated charge transfer plasmons in simple and complex nanoparticle clusters,” *Nanoscale*, vol. 5, no. 20, pp. 9897–9901, 2013.
- [132] P. Nordlander, C. Oubre, E. Prodan, K. Li, and M. Stockman, “Plasmon hybridization in nanoparticle dimers,” *Nano letters*, vol. 4, no. 5, pp. 899–903, 2004.
- [133] K. L. Kelly, E. Coronado, L. L. Zhao, and G. C. Schatz, “The optical properties of metal nanoparticles: the influence of size, shape, and dielectric environment,” 2003.
- [134] J. E. Millstone, S. Park, K. L. Shuford, L. Qin, G. C. Schatz, and C. A. Mirkin, “Observation of a quadrupole plasmon mode for a colloidal solution of gold nanoprisms,” *Journal of the American Chemical Society*, vol. 127, no. 15, pp. 5312–5313, 2005.
- [135] J. Reguera, J. Langer, D. J. de Aberasturi, and L. M. Liz-Marzán, “Anisotropic metal nanoparticles for surface-enhanced Raman scattering,” *Colloidal Synthesis of Plasmonic Nanometals*, pp. 713–754, 2020.
- [136] T. Temple, G. Mahanama, H. Reehal, and D. Bagnall, “Influence of localized surface plasmon excitation in silver nanoparticles on the performance of silicon solar cells,” *Solar Energy Materials and Solar Cells*, vol. 93, no. 11, pp. 1978–1985, 2009.
- [137] M. Schmid, R. Klenk, M. C. Lux-Steiner, M. Topič, and J. Krč, “Modeling plasmonic scattering combined with thin-film optics,” *Nanotechnology*, vol. 22, no. 2, p. 025204, 2010.
- [138] A. Lereu, A. Passian, and P. Dumas, “Near field optical microscopy: a brief review,” *International journal of nanotechnology*, vol. 9, no. 3-7, pp. 488–501, 2012.

- [139] E. Wolf and M. Nieto-Vesperinas, “Analyticity of the angular spectrum amplitude of scattered fields and some of its consequences,” *JOSA A*, vol. 2, no. 6, pp. 886–890, 1985.
- [140] L. Novotny, “From near-field optics to optical antennas,” *Phys. Today*, vol. 64, no. 7, pp. 47–52, 2011.
- [141] L. Novotny and N. Van Hulst, “Antennas for light,” *Nature photonics*, vol. 5, no. 2, pp. 83–90, 2011.
- [142] M. Richard-Lacroix, Y. Zhang, Z. Dong, and V. Deckert, “Mastering high resolution tip-enhanced Raman spectroscopy: towards a shift of perception,” *Chemical Society Reviews*, vol. 46, no. 13, pp. 3922–3944, 2017.
- [143] B. Pettinger, K. F. Domke, D. Zhang, G. Picardi, and R. Schuster, “Tip-enhanced Raman scattering: influence of the tip-surface geometry on optical resonance and enhancement,” *Surface Science*, vol. 603, no. 10–12, pp. 1335–1341, 2009.
- [144] N. Kazemi Zanjani, “Tip-enhances Raman spectroscopy, enabling spectroscopy at the nanoscale,” 2014.
- [145] M. Rahaman, A. G. Milekhin, A. Mukherjee, E. E. Rodyakina, A. V. Latyshev, V. M. Dzhagan, and D. R. Zahn, “The role of a plasmonic substrate on the enhancement and spatial resolution of tip-enhanced Raman scattering,” *Faraday Discussions*, vol. 214, pp. 309–323, 2019.
- [146] M. Stiglitz, “Field and wave electromagnetics,” *Microwave Journal*, vol. 34, no. 9, pp. 206–207, 1991.
- [147] J. Jin, “The finite element method in electromagnetics. 2nd (ed.) wiley,” *New York*, 2002.
- [148] A. Kovetz, “Principles of electromagnetic theory,” 1990.
- [149] R. K. Wangsness, *Electromagnetic fields*, vol. 2. Wiley New York, 1979.
- [150] L. O. Herrmann, V. K. Valev, C. Tserkezis, J. S. Barnard, S. Kasera, O. A. Scherman, J. Aizpurua, and J. J. Baumberg, “Threading plasmonic nanoparticle strings with light,” *Nature communications*, vol. 5, no. 1, pp. 1–6, 2014.
- [151] W. Ma, L. Xu, A. F. de Moura, X. Wu, H. Kuang, C. Xu, and N. A. Kotov, “Chiral inorganic nanostructures,” *Chemical Reviews*, vol. 117, no. 12, pp. 8041–8093, 2017.

- [152] M. Hentschel, D. Dregely, R. Vogelgesang, H. Giessen, and N. Liu, “Plasmonic oligomers: the role of individual particles in collective behavior,” *Acs Nano*, vol. 5, no. 3, pp. 2042–2050, 2011.
- [153] Y. Zhan, D. Y. Lei, X. Li, and S. A. Maier, “Plasmonic fano resonances in nanohole quadrumers for ultra-sensitive refractive index sensing,” *Nanoscale*, vol. 6, no. 9, pp. 4705–4715, 2014.
- [154] N. Hayazawa, Y. Saito, and S. Kawata, “Detection and characterization of longitudinal field for tip-enhanced Raman spectroscopy,” *Applied Physics Letters*, vol. 85, no. 25, pp. 6239–6241, 2004.
- [155] M. Barbry, P. Koval, F. Marchesin, R. Esteban, A. G. Borisov, J. Aizpurua, and D. Sánchez-Portal, “Atomistic near-field nanoplasmonics: reaching atomic-scale resolution in nanooptics,” *Nano letters*, vol. 15, no. 5, pp. 3410–3419, 2015.
- [156] T. Deckert-Gaudig, E. Bailo, and V. Deckert, “Perspectives for spatially resolved molecular spectroscopy–Raman on the nanometer scale,” *Journal of biophotonics*, vol. 1, no. 5, pp. 377–389, 2008.
- [157] J. Renger, S. Grafström, L. M. Eng, and V. Deckert, “Evanescent wave scattering and local electric field enhancement at ellipsoidal silver particles in the vicinity of a glass surface,” *JOSA A*, vol. 21, no. 7, pp. 1362–1367, 2004.
- [158] B. Sharma, M. F. Cardinal, S. L. Kleinman, N. G. Greeneltch, R. R. Frontiera, M. G. Blaber, G. C. Schatz, and R. P. Van Duyne, “High-performance sers substrates: Advances and challenges,” *MRS bulletin*, vol. 38, no. 8, pp. 615–624, 2013.
- [159] K. Liu, D. Li, R. Li, Q. Wang, S. Pan, W. Peng, and M. Chen, “Silver-decorated zno hexagonal nanoplate arrays as sers-active substrates: An experimental and simulation study,” *Journal of Materials Research*, vol. 28, no. 24, pp. 3374–3383, 2013.
- [160] C.-H. Zhang, J. Zhu, J.-J. Li, and J.-W. Zhao, “Small and sharp triangular silver nanoplates synthesized utilizing tiny triangular nuclei and their excellent sers activity for selective detection of thiram residue in soil,” *ACS applied materials & interfaces*, vol. 9, no. 20, pp. 17387–17398, 2017.
- [161] M. Richard-Lacroix and V. Deckert, “Direct molecular-level near-field plasmon and temperature assessment in a single plasmonic hotspot,” *Light: Science & Applications*, vol. 9, no. 1, pp. 1–13, 2020.

- [162] J. Langer, D. Jimenez de Aberasturi, J. Aizpurua, R. A. Alvarez-Puebla, B. Augu  , J. J. Baumberg, G. C. Bazan, S. E. Bell, A. Boisen, A. G. Brolo, *et al.*, “Present and future of surface-enhanced Raman scattering,” *ACS nano*, vol. 14, no. 1, pp. 28–117, 2019.
- [163] F. Latorre, S. Kupfer, T. Bocklitz, D. Kinzel, S. Trautmann, S. Gr  fe, and V. Deckert, “Spatial resolution of tip-enhanced Raman spectroscopy–dft assessment of the chemical effect,” *Nanoscale*, vol. 8, no. 19, pp. 10229–10239, 2016.
- [164] S. Duan, G. Tian, Y. Ji, J. Shao, Z. Dong, and Y. Luo, “Theoretical modeling of plasmon-enhanced Raman images of a single molecule with subnanometer resolution,” *Journal of the American Chemical Society*, vol. 137, no. 30, pp. 9515–9518, 2015.
- [165] N. Chiang, X. Chen, G. Goubert, D. V. Chulhai, X. Chen, E. A. Pozzi, N. Jiang, M. C. Hersam, T. Seideman, L. Jensen, *et al.*, “Conformational contrast of surface-mediated molecular switches yields  ngstrom-scale spatial resolution in ultrahigh vacuum tip-enhanced Raman spectroscopy,” *Nano letters*, vol. 16, no. 12, pp. 7774–7778, 2016.
- [166] C. Su, K. L. Babcock, and L. Huang, “Torsional resonance mode probe-based instrument and method,” Sept. 20 2005. US Patent 6,945,099.
- [167] T. Kasai, B. Bhushan, L. Huang, and C. Su, “Topography and phase imaging using the torsional resonance mode,” *Nanotechnology*, vol. 15, no. 7, p. 731, 2004.
- [168] D. Nowak, W. Morrison, H. K. Wickramasinghe, J. Jahng, E. Potma, L. Wan, R. Ruiz, T. R. Albrecht, K. Schmidt, J. Frommer, *et al.*, “Nanoscale chemical imaging by photoinduced force microscopy,” *Science advances*, vol. 2, no. 3, p. e1501571, 2016.
- [169] J. Jahng, E. O. Potma, and E. S. Lee, “Nanoscale spectroscopic origins of photoinduced tip–sample force in the midinfrared,” *Proceedings of the National Academy of Sciences*, vol. 116, no. 52, pp. 26359–26366, 2019.
- [170] J. Jahng, H. Yang, and E. S. Lee, “Substructure imaging of heterogeneous nanomaterials with enhanced refractive index contrast by using a functionalized tip in photoinduced force microscopy,” *Light: Science & Applications*, vol. 7, no. 1, pp. 1–9, 2018.
- [171] A. Ambrosio, M. Tamagnone, K. Chaudhary, L. A. Jauregui, P. Kim, W. L. Wilson, and F. Capasso, “Selective excitation and imaging of ultraslow phonon polaritons in thin hexagonal boron nitride crystals,” *Light: Science & Applications*, vol. 7, no. 1, pp. 1–9, 2018.

- [172] Y. Huang, D. Legrand, R. Vincent, E. A. Dogbe Foli, D. Nowak, G. Lerondel, R. Bachelot, T. Taliercio, F. Barho, L. Cerutti, *et al.*, “Spectroscopic nanoimaging of all-semiconductor plasmonic gratings using photoinduced force and scattering type nanoscopy,” *ACS photonics*, vol. 5, no. 11, pp. 4352–4359, 2018.
- [173] X. Liu, C. Zhang, C. Duan, M. Li, Z. Hu, J. Wang, F. Liu, N. Li, C. J. Brabec, R. A. Janssen, *et al.*, “Morphology optimization via side chain engineering enables all-polymer solar cells with excellent fill factor and stability,” *Journal of the American Chemical Society*, vol. 140, no. 28, pp. 8934–8943, 2018.
- [174] B. Qiu, Z. Chen, S. Qin, J. Yao, W. Huang, L. Meng, H. Zhu, Y. Yang, Z.-G. Zhang, and Y. Li, “Highly efficient all-small-molecule organic solar cells with appropriate active layer morphology by side chain engineering of donor molecules and thermal annealing,” *Advanced Materials*, vol. 32, no. 21, p. 1908373, 2020.
- [175] J. Jahng, E. O. Potma, and E. S. Lee, “Tip-enhanced thermal expansion force for nanoscale chemical imaging and spectroscopy in photoinduced force microscopy,” *Analytical chemistry*, vol. 90, no. 18, pp. 11054–11061, 2018.
- [176] A. Dazzi, R. Prazeres, F. Glotin, and J. Ortega, “Local infrared microspectroscopy with subwavelength spatial resolution with an atomic force microscope tip used as a photothermal sensor,” *Optics letters*, vol. 30, no. 18, pp. 2388–2390, 2005.
- [177] A. Dazzi, F. Glotin, and R. Carminati, “Theory of infrared nanospectroscopy by photothermal induced resonance,” *Journal of Applied Physics*, vol. 107, no. 12, p. 124519, 2010.
- [178] A. Dazzi, C. B. Prater, Q. Hu, D. B. Chase, J. F. Rabolt, and C. Marcott, “Afm-ir: combining atomic force microscopy and infrared spectroscopy for nanoscale chemical characterization,” *Applied spectroscopy*, vol. 66, no. 12, pp. 1365–1384, 2012.
- [179] F. Lu, M. Jin, and M. A. Belkin, “Tip-enhanced infrared nanospectroscopy via molecular expansion force detection,” *Nature photonics*, vol. 8, no. 4, pp. 307–312, 2014.
- [180] K. Kjoller, J. Felts, D. Cook, C. Prater, and W. P. King, “High-sensitivity nanometer-scale infrared spectroscopy using a contact mode microcantilever with an internal resonator paddle,” *Nanotechnology*, vol. 21, no. 18, p. 185705, 2010.

- [181] J. Jahng, J. Brocious, D. A. Fishman, S. Yampolsky, D. Nowak, F. Huang, V. A. Apkarian, H. K. Wickramasinghe, and E. O. Potma, “Ultrafast pump-probe force microscopy with nanoscale resolution,” *Applied Physics Letters*, vol. 106, no. 8, p. 083113, 2015.
- [182] R. A. Murdick, W. Morrison, D. Nowak, T. R. Albrecht, J. Jahng, and S. Park, “Photoinduced force microscopy: A technique for hyperspectral nanochemical mapping,” *Japanese Journal of Applied Physics*, vol. 56, no. 8S1, p. 08LA04, 2017.
- [183] J. Jahng, B. Kim, E. S. Lee, and E. O. Potma, “Quantitative analysis of sideband coupling in photoinduced force microscopy,” *Physical Review B*, vol. 94, no. 19, p. 195407, 2016.
- [184] S. B. Clough, X. F. Sun, S. Subramanyam, N. Beladakere, A. Blumstein, and S. K. Tripathy, “Molecular-dynamics simulation of substituted conjugated ionic polyacetylenes,” *Macromolecules*, vol. 26, no. 4, pp. 597–600, 1993.
- [185] M. C. Da Silva and C. Zaretzky, “Non-linear modal coupling in planar and non-planar responses of inextensional beams,” *International Journal of Non-Linear Mechanics*, vol. 25, no. 2-3, pp. 227–239, 1990.
- [186] C. Dietz, M. Schulze, A. Voss, C. Riesch, and R. W. Stark, “Bimodal frequency-modulated atomic force microscopy with small cantilevers,” *Nanoscale*, vol. 7, no. 5, pp. 1849–1856, 2015.
- [187] M. Lee and W. Jhe, “General theory of amplitude-modulation atomic force microscopy,” *Physical Review Letters*, vol. 97, no. 3, p. 036104, 2006.
- [188] J. R. Lozano and R. Garcia, “Theory of phase spectroscopy in bimodal atomic force microscopy,” *Physical Review B*, vol. 79, no. 1, p. 014110, 2009.
- [189] R. Garcia, C. Gomez, N. Martinez, S. Patil, C. Dietz, and R. Magerle, “Identification of nanoscale dissipation processes by dynamic atomic force microscopy,” *Physical review letters*, vol. 97, no. 1, p. 016103, 2006.
- [190] C. J. Gomez and R. Garcia, “Determination and simulation of nanoscale energy dissipation processes in amplitude modulation afm,” *Ultramicroscopy*, vol. 110, no. 6, pp. 626–633, 2010.
- [191] P. M. Hoffmann, S. Jeffery, J. B. Pethica, H. Ö. Özer, and A. Oral, “Energy dissipation in atomic force microscopy and atomic loss processes,” *Physical review letters*, vol. 87, no. 26, p. 265502, 2001.

- [192] I. Rajapaksa and H. Kumar Wickramasinghe, “Raman spectroscopy and microscopy based on mechanical force detection,” *Applied physics letters*, vol. 99, no. 16, p. 161103, 2011.
- [193] https://en.wikipedia.org/wiki/Lorentz_force.
- [194] D. J. Griffiths, “Introduction to electrodynamics,” 2005.
- [195] G. Socrates, *Infrared and Raman characteristic group frequencies: tables and charts*. John Wiley & Sons, 2004.
- [196] K. Bahlmann and S. Hell, “Electric field depolarization in high aperture focusing with emphasis on annular apertures,” *Journal of microscopy*, vol. 200, no. 1, pp. 59–67, 2000.
- [197] N. Kazemi-Zanjani, S. Vedraïne, and F. Lagugné-Labarthet, “Localized enhancement of electric field in tip-enhanced Raman spectroscopy using radially and linearly polarized light,” *Optics Express*, vol. 21, no. 21, pp. 25271–25276, 2013.
- [198] M. Rajaei, M. A. Almajhadi, J. Zeng, and H. K. Wickramasinghe, “Near-field nanoprobng using si tip-au nanoparticle photoinduced force microscopy with 120: 1 signal-to-noise ratio, sub-6-nm resolution,” *Optics express*, vol. 26, no. 20, pp. 26365–26376, 2018.
- [199] A. Pittner, S. Wendt, D. Zopf, A. Dathe, N. Grosse, A. Csáki, W. Fritzsche, and O. Stranik, “Fabrication of micro-patterned substrates for plasmonic sensing by piezo-dispensing of colloidal nanoparticles,” *Analytical and bioanalytical chemistry*, vol. 411, no. 8, pp. 1537–1547, 2019.
- [200] R. Meyer, S. Trautmann, K. Rezaei, A. George, A. Turchanin, and V. Deckert, “Synergy of photoinduced force microscopy and tip-enhanced Raman spectroscopy—a correlative study on mos₂,” *ACS Photonics*, vol. 6, no. 5, pp. 1191–1198, 2019.
- [201] C. Lee, H. Yan, L. E. Brus, T. F. Heinz, J. Hone, and S. Ryu, “Anomalous lattice vibrations of single-and few-layer mos₂,” *ACS nano*, vol. 4, no. 5, pp. 2695–2700, 2010.
- [202] X. Zhang, X.-F. Qiao, W. Shi, J.-B. Wu, D.-S. Jiang, and P.-H. Tan, “Phonon and Raman scattering of two-dimensional transition metal dichalcogenides from monolayer, multilayer to bulk material,” *Chemical Society Reviews*, vol. 44, no. 9, pp. 2757–2785, 2015.
- [203] C. C. Neacsu, S. Berweger, and M. B. Raschke, “Tip-enhanced Raman imaging and nanospectroscopy: sensitivity, symmetry, and selection rules,” *NanoBiotechnology*, vol. 3, no. 3-4, pp. 172–196, 2007.

Selbständigkeitserklärung

Ich erkläre, dass ich die vorliegende Arbeit selbständig und unter Verwendung der angegebenen Hilfsmittel, persönlichen Mitteilungen und Quellen angefertigt habe.

Ort, Datum

Unterschrift der Verfasserin/des Verfassers

Copyright Permissions



ACS Publications <acs@service-now.com>

Wed 3/8, 3:44 PM

Kourosh Rezaei ▾

↻ Reply all | ▾

Dear Dr. Rezaei,

Thank you for contacting ACS Publications Support.

Your permission request is granted and there is no fee for this reuse.

In your planned reuse, you must cite the ACS article as the source, add this direct link: <https://pubs.acs.org/doi/10.1021/acsphotonics.8b01716>, and include a notice to readers that further permissions related to the material excerpted should be directed to the ACS.

Please do not hesitate to contact us if you need any further assistance.

Sincerely,

Vojin Vucic
ACS Publications Support
Customer Services & Information
Website: <https://acs.service-now.com/acs>
Email: support@services.acs.org
Phone: 800-227-9919 | 202-872-(HELP) 4357

Case Info:

Case Number : CSCSI0123051

Created On: 03-08-2023 06:34:52 AM EST

Short Description: Permission request for reusing the figures

Wavelength-Dependent Optical Force Imaging of Bimetallic Al-Au Heterodimers

Author: Thejaswi Tumkur, Xiao Yang, Chao Zhang, et al

Publication: Nano Letters

Publisher: American Chemical Society

Date: Mar 1, 2018



Copyright © 2018, American Chemical Society

PERMISSION/LICENSE IS GRANTED FOR YOUR ORDER AT NO CHARGE

This type of permission/license, instead of the standard Terms and Conditions, is sent to you because no fee is being charged for your order. Please note the following:

- Permission is granted for your request in both print and electronic formats, and translations.
- If figures and/or tables were requested, they may be adapted or used in part.
- Please print this page for your records and send a copy of it to your publisher/graduate school.
- Appropriate credit for the requested material should be given as follows: "Reprinted (adapted) with permission from (COMPLETE REFERENCE CITATION). Copyright (YEAR) American Chemical Society." Insert appropriate information in place of the capitalized words.
- One-time permission is granted only for the use specified in your Rightslink request. No additional uses are granted (such as derivative works or other editions). For any uses, please submit a new request.

If credit is given to another source for the material you requested from Rightslink, permission must be obtained from that source.

[BACK](#)

[CLOSE WINDOW](#)